UNIVERSITAT DE BARCELONA

Dynamics of subduction systems with opposite polarity in adjacent segments: application to the Westernmost Mediterranean

Mireia Peral Millán

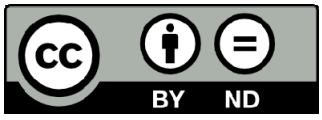

Departament de Dinàmica de la Terra i de l'Oceà
Facultat de Ciències de la Terra
Universitat de Barcelona

Dynamics of subduction systems with opposite polarity in adjacent segments: application to the Westernmost Mediterranean

Tesis doctoral presentada por Mireia Peral Millán al Departament de Dinàmica de la Terra i de l'Oceà de la Universitat de Barcelona para optar al grado de Doctora en Ciencias de la Tierra

Group of Dynamic of the Lithosphere (GDL)
Institut de Ciències de la Terra Jaume Almera (ICTJA)
Consejo Superior de Investigaciones Científicas (CSIC)

Directores:

Prof. Dr. Manel Fernàndez Ortiga

Dr. Sergio Zlotnik

Tutor:

Prof. Dr. Juan José Ledo Fernández

Barcelona 2020

CSIC Consejo Superior de Investigaciones Científicas
ICTJA Institut de Ciències de la Terra Jaume Almera
Universitat de Barcelona

A mis padres

Gota a gota, se ensambló el mar

-Juan José Peral-

Agradecimientos

Y por fin llegó…

Ese día, que nunca imaginé tan próximo y tan cercano, ya está al alcance de mis manos. Desde mi infancia, aprendí que para lograr alcanzar la cima de una montaña, por muy alta y desafiante que sea su silueta, hay que hacerlo paso a paso, con decisión y seguridad, ser firme en cada etapa, pensar con celeridad y paciencia a la vez, sin precipitaciones, para elegir o tratar de elegir los mejores senderos, por angostos que puedan parecer, descansar y darse un respiro para tomar aire cuando sea necesario; quizás simplemente deteniéndose a contemplar el marco del entorno del momento y, ante cualquier adversidad, consultar en el baúl de las lecciones aprendidas. Después, una última mirada hacia adelante para volver a retomar la andadura con mayor ahínco, si cabe. Así he logrado, por fin, alcanzar la cima, después de escribir, una a una, las páginas de esta tesis; como si hubiera estado, a lo largo de estos años de investigación, recorriendo los más insólitos senderos, con una gran dosis de ilusión, esfuerzo y dedicación.

En primer lugar, y por toda la confianza que han depositado en mí para escribirla, a mis directores de tesis: Manel Fernàndez y Sergio Zlotnik. Gracias por vuestra paciencia, tiempo, dedicación y por ayudarme a superar todas las dificultades que han ido surgiendo en el camino, que no han sido pocas. Gracias por enseñarme lo mejor del mundo científico. Sin duda, sin vosotros este proyecto no hubiera sido posible, nunca hubiera visto la luz.

Agradecer también a Juanjo Ledo por aceptar la tutoría de esta tesis y a la comisión de doctorado de la UB (*Universitat de Barcelona*) por el seguimiento realizado durante estos años. Quisiera agradecer también a mi antigua profesora de la UB Pilar Queralt por haberme introducido en el campo científico de la Geofísica.

Gracias a Jaume Vergés, investigador principal de los proyectos entre los que está incluida esta tesis, por brindarme esta gran oportunidad y por todos los conocimientos geológicos que me ha aportado y que, humildemente, he intentado plasmar en ella.

Agradecer también la ayuda de mi compañero y amigo Jonas Ruh, con quien he tenido el honor, no sólo de trabajar, sino también de poder adquirir conocimientos sobre modelización numérica. Gracias por permitirme el acceso al software *I3Elvis* y al supercomputador *BRUTUS* (*Swiss Federal Institute of Technology, Switzerland*).

Agradezco, igualmente, a Ivone Jimenez-Munt y Sergio Zlotnik, la gestión y la supervisión de las solicitudes de acceso a los supercomputadores de la RES (Red Española de Supercomputación), hecho imprescindible para la realización de este trabajo. Gracias al BSC (*Barcelona Supercomputer Center*) y a la UPC (*Universitat Politècnica de Catalunya*) por permitirme hacer uso de sus instalaciones computacionales, así como a mi amigo y compañero Jeremías Likerman, quien me ayudó en los inicios, especialmente en el área técnica, como usuario conocedor de los supercomputadores. A Francesca Funiciello y a Claudio Faccenna por brindarme la oportunidad de trabajar en el LET (*Laboratory of Experimental Tectonics*) de Roma durante mi estancia en Italia. Gracias por vuestra confianza y enriquecedoras enseñanzas. Y gracias también a mi compañera de laboratorio Agi, de quien aprendí las bases más importantes de la modelización análoga.

A todo el equipo de GDL (*Group of Dynamics of the Lithosphere*) y compañeros del ICTJA (*Institut de Ciències de la Terra Jaume Almera*). A Chiara por proporcionarme datos imprescindibles. A Ignacio, por el tiempo dedicado en la configuración de mi ordenador, especialmente en los inicios de esta aventura. A Marc, por proporcionarme todas las herramientas informáticas necesarias. A Alba y Mar por su amistad y sabios consejos. A David y Ajay por su gran compañerismo. A Max, por soportarme durante su estancia en el Instituto. A Jordi, por su ayuda en la edición de las imágenes y su continuo apoyo. A Xavi, nuestro conserje, por alegrarnos el día cada mañana. En definitiva, y aunque no estén aquí nombrados, gracias a todos los que me habéis ayudado a recorrer y disfrutar de este camino que hemos andado juntos.

Una mención especial merece mi "compitrueno" Ángel, con quien he compartido la mayor parte del tiempo dedicado a este trabajo. Gracias por aguantar mis risas y mi mal humor, por no enfadarte nunca, por ayudarme siempre con todo lo que he necesitado y sobre todo por apoyarme en los momentos más delicados. Echaré de menos nuestras discusiones científicas, nuestras confidencias y nuestros bailes (bueno, ¡eso espero que no decaiga nunca!). Sin duda has sido el mejor compañero de "combate" que he podido tener a mi lado.

Y ante todo, gracias a mis padres, a quienes tanto les debo y a los que hoy dedico orgullosa esta tesis. Porque la ilusión y el esfuerzo que hay detrás de este trabajo también es vuestro. A mi hermano, por todo el apoyo que siempre me has dado. A Saara y a Eva, mi pequeña estrella, por los entrañables momentos que me habéis regalado entre página y página. A Rubén, por estar a mi lado durante la recta final de esta tesis. Y a Neita, mi pequeña amiga de cuatro patas, por sus ronquidos que tanto me han inspirado.

Funding

This thesis is part of the projects WE-ME (PIE-CSIC-201330E111), ALPIMED (PIE-CSIC-201530E082) and SUBTETIS (PIE-CSIC-201830E039) financed by the CSIC and EQUINOR. I also thank to the projects AECT-2015-3-0002, AECT-2016-1-0002, AECT-2016-3-0012, AECT-2017-1-0018, AECT-2017-2-0013, AECT-2017-3-0008, AECT-2018-1-0007, AECT-2018-3-0007, AECT-2019-1-0013 and AECT-2019-2-0005 for allowing me to use the facilities of the Barcelona Supercomputing Center (BSC-CNS). This work was carried out within the Grups de Recerca Reconeguts i Finançiats per la Generalitat de Catalunya 2017SGR847.

TABLE OF CONTENTS

Summary

Summary

The objective of this thesis is to study the first-order dynamics of subduction systems characterized by opposite dip polarity in adjacent plate segments. The absence of previous studies analyzing the geodynamic evolution of these systems has defined the research strategy of the present work. Consequently, the thesis consists of three different parts combining analog experiments and numerical models of very simple double subduction systems and its application to the Westernmost Mediterranean where a subduction system with opposite polarity in adjacent plate segments (double polarity subduction) has been proposed to explain the formation and evolution of this region.

Part 1. Analog experiments of subduction systems with opposite polarity in adjacent segments

Firstly, I have studied the first-order plate dynamics of subduction systems with opposite polarity in adjacent plate segments by means of analog experiments. Laboratory experiments have been carried out in the Laboratory of Experimental Tectonics in Roma Tre University during a two month stay in Rome (Italy) under the advice of Prof. Dr. Francesca Funiciello and Prof. Dr. Claudio Faccenna.

A total of eighteen experiments have been designed, including four with a single plate subduction as reference models. The laboratory experiments are composed of one or two separates plates made of silicon putty representing the lithosphere and glucose syrup representing the mantle. The plates are fixed at their back edge to enforce a slab rollback behavior and subduction is started by deflecting manually the leading edge of the plate (i.e., initial slab pull). Different setups have been designed to test the influence of the width of plates and the initial separation between them on the evolution of the system.

Results show that the mantle flow induced by both plates is asymmetric relative to the axis of each plate causing a progressive merging of the toroidal cells that prevents a steady state phase of the subduction process and generates a net outward drag perpendicular to the plates. Trench retreat velocities depend on the relative position of the trenches, increasing when trenches approach to each other and decreasing when they separate after their intersection.

Part 2. Reproducing analog experiments of subduction systems with numerical modeling

Secondly, some of the previous laboratory experiments have been performed by means of numerical modeling to compare and complement previous results and quantify the relevant physical parameters characterizing a double polarity subduction system. Around thirty-five numerical models, in addition to preliminary tests, have been performed although only fifteen are presented in this thesis showing the most outstanding and satisfactory results. The set of the numerical models have been run in the supercomputer *MARENOSTRUM 4* (Barcelona Supercomputing Center, Spain) and *BRUTUS* (Swiss Federal Institute of Technology, Switzerland), with an average computation time of 3 weeks per model.

The 3D numerical setup is chosen with similar material parameters, geometry and dimensions as for previous subuction analog models consisting on one or two viscous plates descending into the upper mantle in opposite directions. Plates are fixed at their trailing edge to enforce roll-back behavior during density-driven subduction. A small perturbation is initially imposed to initiate subduction. Firstly, computational domain size, boundary conditions, rheology and thickness of plates are tested to find the numerical model that best represents analog experiments. Secondly, relevant parameters controlling the double polarity subduction process are studied by means of numerical techniques.

Results show that the most suitable numerical boundary conditions to reasonably reproduce the analog results are free-slip at the lateral boundaries and no-slip at the bottom of the model. Lateral boundary conditions affect the evolution of the system at short distances allowing for a reduction of the size of the model domain relative to the analog model and to increase the resolution and saving computation time. Complementing previous experiments of double polarity subduction, numerical results show that the induced mantle flow generates a stress coupling between the adjacent plates slowing down the overall subduction process and producing lateral movement of plates and asymmetrical deformation of the slabs and trenches.

Part 3. The Alboran and Algerian basins (Westernmost Mediterranean). A case study of double subduction with opposite polarity in adjacent segments.

Finally, a 3D numerical model of double subduction with opposite polarity in adjacent plate segments has been performed simulating the tectonic setting of the Westernmost Mediterranean. The evolution of the Alboran-Tethys slab (*Betic-Rif slab*) is reproduced in this tectonic scenario studying the influence of the adjacent plate segment. Around forty numerical models have been performed varying physical and geometrical parameters, including preliminary numerical tests. In this thesis only the final double polarity subduction model and a single plate subduction model are presented. The numerical models have been run in the supercomputer *MARENOSTRUM 4* (Barcelona Supercomputing Center, Spain) with an average computation time of 4 weeks per model.

The model setup consists of two oceanic plate segments with a visco-plastic rheology subducting in opposite directions into the viscous upper mantle and starting at 35 Ma. In the present-day Alboran Basin region, the plate segment corresponding to the Alboran-Tethys slab (*Betic-Rif slab*) dips to the southeast with the trailing edge fixed to the Iberian margin. A continental African plate segment is included at the west side of this plate. In the present Algerian Basin region the plate segment (*Tell-Kabylies slab*) dips to the northwest and the trailing edge is fixed to the African margin. A small slab perturbation to account for the Africa-Iberia convergence prior to 35 Ma is initially imposed and the subsequent subduction process is driven by Rayleigh-Taylor instability. In addition, a reference model including only the Alboran-Tethys slab has been performed in order to study the influence of an adjacent plate segment subducting in opposite direction.

Results show that the progressive curvature of the Alboran-Tethys slab is due to the lack of a transform zone in its connection with the Atlantic oceanic to the west and the strong segmentation of the African margin. This produces larger retreat velocities in the eastern side of the slab, where a transform zone separates the Alboran segment from the Algerian segment, than in the western side. Trench retreat velocities of both plate segments are measured concluding that the opening of the Alboran Basin occurs around 22 Ma. The influence of the adjacent Algerian segment generates an asymmetrical flow pattern around both trenches slowing down the overall subduction process of the Alboran plate segment.

CHAPTER 1

Introduction

Chapter 1

Introduction

This thesis presents a study on subduction systems with opposite polarity in adjacent plate segments (here in after I will use double polarity subduction to denote these systems). The dynamics of such a process is analyzed using a combination of analog and numerical modeling techniques. Moreover, the geological consequences of its evolution are described.

The study is motivated by the model evolution of the Westernmost Mediterranean proposed by *Vergés and Fernàndez* [2012] where these authors advocate a lateral change in subduction polarity of the Ligurian-Tethys oceanic domain to explain the formation and evolution of the Betic-Rif orogenic system and the Alboran back-arc basin (Figure 1.1).

The evolution of this region is still highly debated by geologists and geophysicists and there is no consensus on the initial geometry (paleogeography) and processes involved other than the slab rollback as the main driving mechanism. The double polarity subduction model differs largely from those proposed up to date to explain the evolution of the region.

Besides the model proposed in the Westernmost Mediterranean, double subduction systems with opposite polarity in adjacent plate segments have been also observed to occur in several regions of the Earth (Figure 1.2), getting more attention during last years. Indeed, a complex slab interaction occurs beneath Taiwan due to the presence of two opposite subduction zones that intersect at a right angle [e.g., *Lallemand et al*., 2001; *Lin and Kuo*, 2016]. Farther south, the Manila slab is dipping east, whereas in the south the Philippine slab dips west [e.g., *Hall and Spakman*, 2015]. In New Zealand, the Australian

plate is being subducted beneath the Pacific plate with opposite polarity to the subduction along the Hikurangi Margin [e.g., *Lamb*, 2011]. The updated hypocenter distribution in the Pamir-Hindu Kush region displays a sharp lateral change in the dip of the Wadati-Benioff zone from the Hindu Kush, dipping to the north, to the Pamir arc, dipping to the southeast [*Kufner et al.*, 2016; *Liao et al.*, 2017]. Tectonic reconstructions of the Alps-Carpathians-Dinarides system also show an opposed subduction polarity between the Alpine-Carpathian Front (S-dipping) and the Dinaric-Hellenic Front (NE-dipping) since ca. 35 Ma [e.g., *Handy et al.*, 2014]. Finally, in Italy, some authors [e.g., *Vignaroli et al.*, 2008] describe the Voltri Massif as an extensional domain formed as a consequence of a reversal subduction polarity at the junction between the Western Alps and the North Apennines.

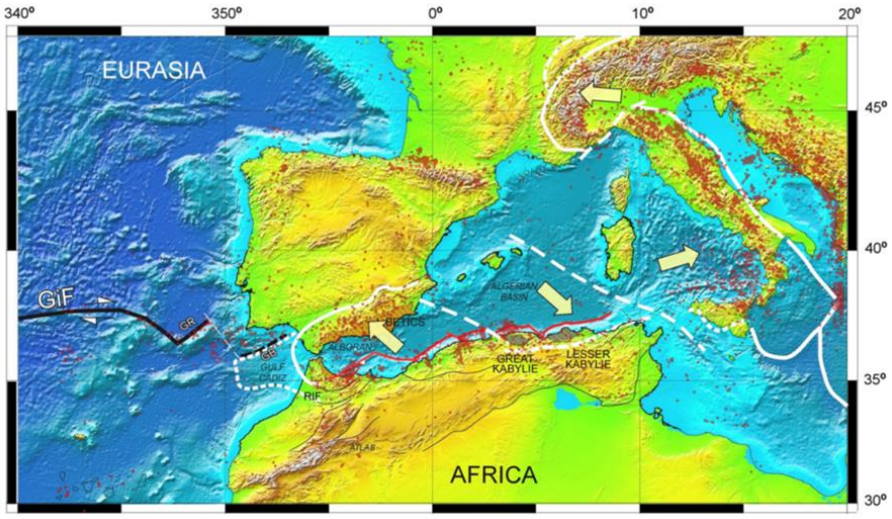

Figure 1.1 Map of the Western Mediterranean showing the kinematic model proposed by *Vergés and Fernàndez* [2012] based on the interaction of plates with opposite subduction polarity separated by transform faults (dashed white lines). Thick yellow arrows indicate the direction of retreating slabs. Continuous white lines show the geometry of arcuate orogenic systems. Figure from *Vergés and Fernàndez* [2012].

Despite the occurrence of double polarity subduction in nature, few geodynamic studies of this process have been published [*Király et al.*, 2016; *Peral et al.*, 2018]. *Kiràly et al.* [2016] presents a 3D numerical model focusing on the interactions between the mantle flow cells induced by the retreating trenches. It concluded that the slabs interact with each other when they are at distances ≤ 600 km. Although they obtain new results on this process, their study do not analyze on the interactions between mantle flow and plate deformations. In fact, in their model setup the authors assume perfect symmetry along the axis of the plates and periodic boundary conditions along the walls parallel with the

trenches. Although these conditions are adequate to study the stress propagation through the mantle, they impose some restrictions in analyzing the deformation of plates, the separate roles of the plate width and the initial separation between plates, and the geometry of the trench curvature. On the other hand, *Peral et al.* [2018] presents for the first time a series of analog models simulating the evolution of a double polarity subduction system and conclude that the interaction between the return flows correlates with variations of rollback velocities and generates a net outward drag perpendicular to the plates. This work is part of this thesis and is presented in Chapter 4.

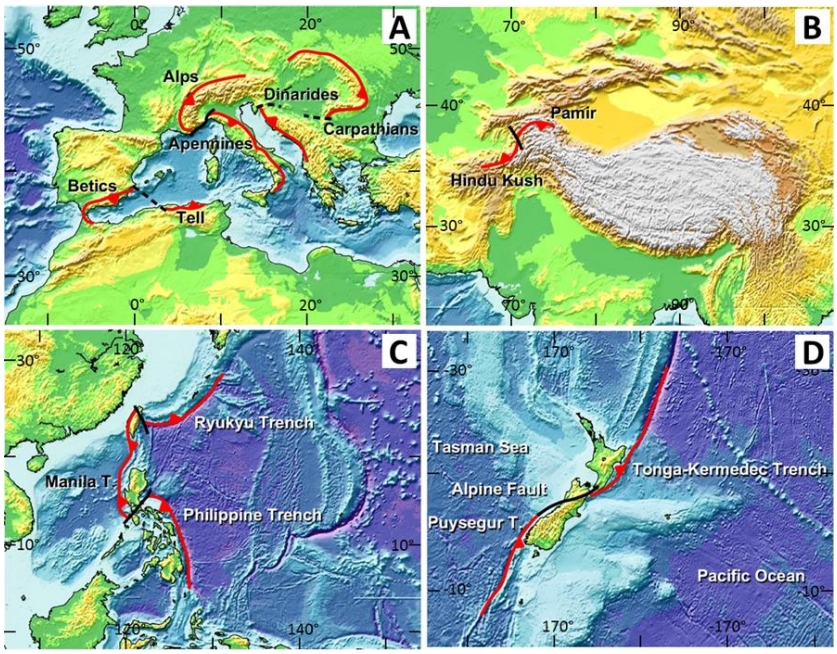

Figure 1.2 Location of double subduction systems with opposite polarity in adjacent segments (double polarity subduction). (A) Mediterranean region: Betic-Rif-Tell system [*Vergés and Fernàndez*, 2012]; Alps-Apennines system [*Vignaroli et al.*, 2008]; Carpathians-Dinarides system [*Handy et al.*, 2014]. (B) West Tibet region: Pamir-Hindu Kush system [*Kufner et al.*, 2016]. (C) West Pacific region: Ryukyu-Manila system [*Lallemand et al.*, 2001; *Lin and Kuo*, 2016]; Manila-Philipine system [*Hall and Spakman*, 2015]. (D) New Zealand region: Kermadec-Puysegur system [*Lamb*, 2011]. The red lines and triangles denote trenches and subduction polarity; the continuous black lines denote active transform zones; the discontinuous black lines denote inactive transform zones. Figure from *Peral et al.* [2018].

1.1 Objectives and methods

This thesis aims to understand the dynamics of a double subduction system with opposite polarity in adjacent plate segments (Figure 1.3) and estimate its geological consequences. The generic objectives of this thesis are:

1) To understand the first-order dynamics of the complex mantle flow generated in such subduction systems by analyzing the interaction between the subducting plates in terms of their deformation and trench velocities, and the intervening parameters characterizing the behavior of the system such as the geometry of plates, viscosity ratios, and boundary conditions.

2) Combining analog and numerical methods to better understand their strength and limitations in modeling complex 3D subduction systems and using the complementarity of these approaches to gain insight on its dynamic evolution.

3) Reproducing the time of formation of the present Alboran and Algerian basins with a self-consistent dynamic model, and the arcuate geometry and actual position of the lithospheric slab beneath the Betic-Rif orogeny that is consistent with the tectonic scenario inferred from plate reconstruction models in the region.

To this end, two complementary modeling techniques are used: laboratory analog models and numerical methods. Numerical methods enable to test parameters and create setups that are too complex for laboratory experiments. On the other hand, the complexities of geological processes sometimes do not even allow formulate the mathematical problem to be solved numerically. And, despite of modern computer capabilities, the computer power able to deal with the resolution required to simulate scales of geological processes is hardly available. Moreover, the amount of methodological parameters required to setup a modern day numerical model and the technical knowledge required to tune them, makes numerical models a time consuming process. The combination of the analog and the numerical approaches, and their reconciliation, increases the truthfulness of the results.

This thesis consists on three parts. Firstly, analog models of double polarity subduction have been performed in order to better understand the first-order plate dynamics of these systems. Secondly, some of the previous laboratory experiments have been numerically reproduced to compare and complement analog and numerical results. Finally, a 3D numerical model of double polarity subduction with a setup applicable to the Westernmost Mediterranean region is designed with the aim of reproducing the timing of the formation of both basins and the arcuate geometry of the slab beneath the Betic-Rif orogeny.

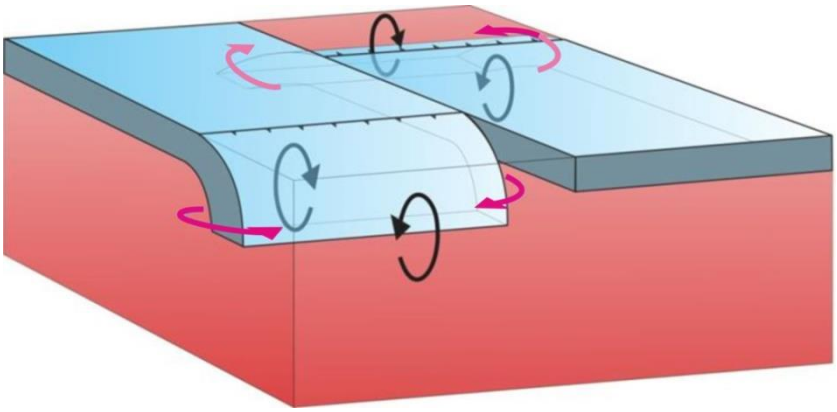

Figure 1.3 Double subduction system with opposite polarity in adjacent segments. The model consists of two oceanic plates (in blue) subducting into the upper mantle (in red) in opposite directions. Black arrows denote the direction of the induced poloidal flow. Fuchsia arrows denote the direction of the induced toroidal flow.

1.2 Outline of the Thesis

This thesis is divided into eight chapters that have been organized as follows (Figure 1.4):

Chapter 2 reviews the dynamics of subduction systems. Firstly, the general characteristics of the most typical subduction zones are described. Secondly, the general behavior of single plate subduction is described by analyzing the forces acting on the system, the basic trench kinematics and the different modes of subduction. Finally, I review the findings of recent studies based on different configurations of double subduction systems.

Chapter 3 describes the fundamentals of analog experiments and numerical modeling of subduction systems. Common materials used for the laboratory experiments and the scaling parameters are defined. Laboratory experiments presented here have been carried out in the Laboratory of Experimental Tectonics in Roma Tre University (Rome, Italy). On the other hand, the basics of the numerical methods and numerical codes used are also described in this chapter. Numerical models have been run in the supercomputer *MARENOSTRUM 4* (Barcelona Supercomputing Center, Spain) and *BRUTUS* (Swiss Federal Institute of Technology, Switzerland).

Chapter 4 presents the results of analog experiments of double subduction systems with opposite polarity in adjacent segments. The laboratory model is composed of two

separate plates made of silicone putty representing the lithosphere, on top of a tank filled with glucose syrup representing the mantle. The set of experiments is designed to test the influence of the width of the plates and the initial separation between them on the resulting trench velocities, deformation of plates, and mantle flow. Additional single plate subduction models have been performed as reference models.

The results presented in Chapter 4 have been published in the scientific journal *Tectonics* (American Geophysical Union):

Peral, M., Király, Á., Zlotnik, S., Funiciello, F., Fernàndez ,M., Faccenna, C., & Vergés, J. (2018). *Opposite subduction polarity in adjacent plate segments*. Tectonics, 37. https://doi.org/10.1029/ 2017TC004896.

Chapter 5 presents the results of a 3D numerical model of double subduction system with opposite polarity in adjacent segments using similar material parameters, geometry and dimensions as for previously carried out laboratory experiments. Numerical models varying the computational domain size and boundary conditions are conducted and compared to analog experiments to make an analog-numerical preliminary comparison providing new insights on subduction modeling. Plate deformation, trench retreat velocities, mantle velocities, stresses and forces within the mantle are quantified for the double polarity subduction system complementing previous analog results. Additional single plate subduction models have been performed as reference models and to study the influence of the plate thickness and rheology on trench curvature.

The results presented in Chapter 5 are submitted and under review to the scientific journal *Geochemistry, Geophysics, Geosystems* (American Geophysical Union).

Chapter 6 presents the results of a 3D numerical model of double subduction system with opposite polarity in adjacent segments simulating the tectonic setting of the Westernmost Mediterranean. Several factors characterizing the evolution of the system as the curvature evolution of the Alboran-Tethys slab and the influence of the adjacent Algerian-Tethys segment have been studied. Moreover, mantle flow and plate deformation produced by this subduction process are analyzed identifying the linking mechanisms coupling the behavior of the retreating plates. Finally, the evolution of the trench retreat velocity of both plates is correlated with geological observations.

A manuscript with the material presented in Chapter 6 is in preparation.

Chapter 7 is focused on discussing the main geological consequences of the dynamics of double polarity subduction systems. The most relevant results of this work are analyzed providing a better knowledge in the field of double subduction dynamics and in the geodynamic evolution of the Westernmost Mediterranean.

Finally, Chapter 8 presents the final conclusions of this thesis and proposes possible future actions to go deeper in the study of complex subduction systems.

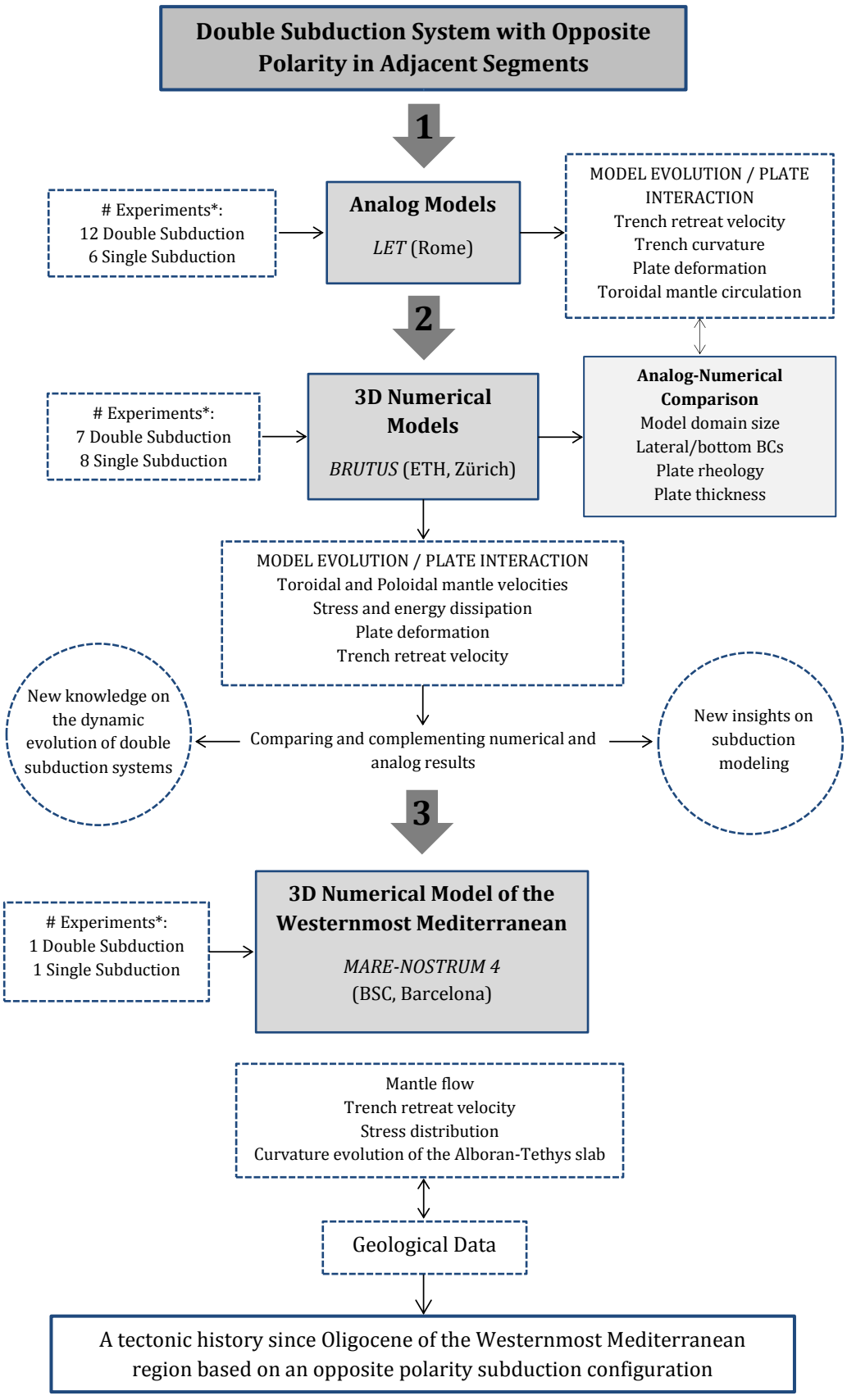

Figure 1.4 Flow chart showing the steps followed to achieve the objective of this thesis. BCs: Boundary conditions. *Number of experiments presented in this thesis; the preliminary experiments performed are not indicated.

CHAPTER 2

Subduction systems

Chapter 2

Subduction systems

The theory of plate tectonics was well established around 1960. This theory describes the outer shell of the Earth as a number of thin rigid plates, the lithosphere, that are continuously in relative motion above the Earth's mantle that behaves like a fluid. The relative plate velocities are of the order of a few cm/year and a large part of important geological phenomena as earthquakes, volcanic eruptions and mountain building occurs at plate boundaries.

The lithosphere is continually created and consumed at plate boundaries. Three plate boundaries can be distinguished depending on the relative motion between the plates, namely transform, divergent and convergent. Thereby, in transform or conservative plate boundaries no lithosphere is created or destroyed as plates slide past each other in opposite directions. In divergent plate boundaries, plates separate from each other and new lithosphere is created in the mid-oceanic ridges by melting and further solidification of the ascending mantle. The complementary process occurs at convergent boundaries where one plate bends and sinks under another into the Earth's mantle forming either a subduction zone or a continental collision. Subduction occurs in many zones on Earth when the old ocean lithosphere becomes gravitationally unstable with respect to the hot mantle rocks [*Davies and Richards*, 1992; *Cloos*, 1993; *Stern*, 2002]. This mechanism is so effective that it makes subduction the largest recycling system of our planet and it is considered as the main driving mechanism of plate tectonics [e.g., *Davies and Richards*, 1992]. Figure 2.1 shows the major subduction zones on Earth. Typical subduction zones show unique subduction polarity and long and linear trenches that may reach up to 7400 km long.

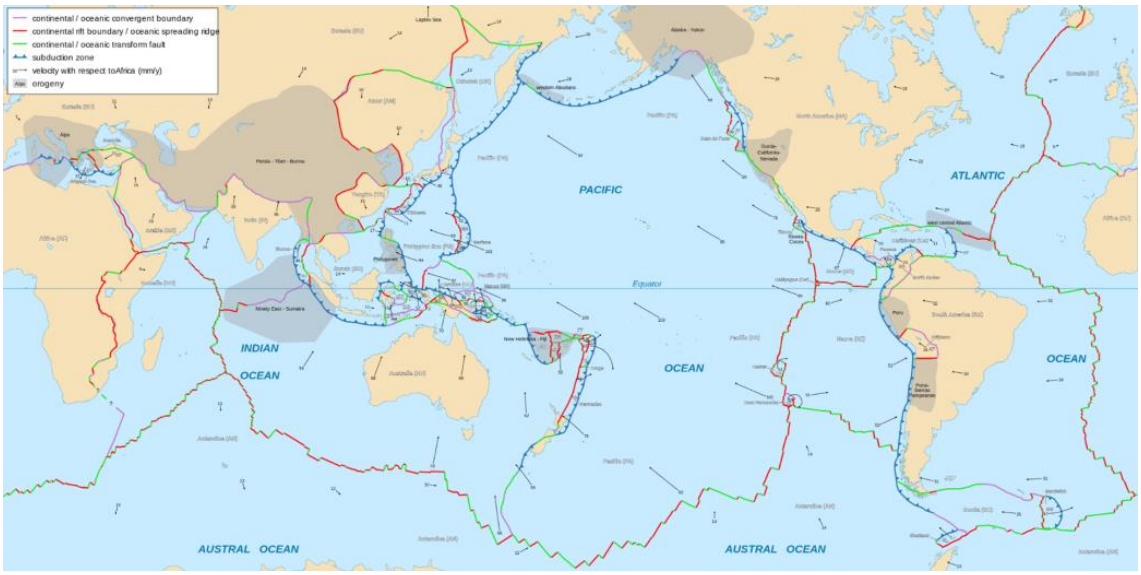

Figure 2.1 Plate boundaries including major subduction zones on Earth [by *Eric Gaba*; *Wikimedia-Commons CC-BY-SA-2.5* (http://creativecommons.org/licenses/by-sa/)]

Subduction occurs between the convergence of two oceanic plates or between an oceanic and a continental plate. Figure 2.2 is a schematic section illustrating the main components of a typical subduction zone and their interactions. The subducting lithosphere is the oceanic plate and descends beneath the overriding plate (oceanic or continental) while it is denser than the surrounding mantle rocks at any depth, although phase changes and compositional variations complicate this process. At 660 km depth the slab, the lithosphere that has already subducted, may accommodate or penetrate in the lower mantle discontinuity associated with the solid-solid phase change from spinel to perovskite and magnesiowüstite, as revealed from mantle tomography studies [*Turcotte*, 1982]. The direct penetration of the slab into the lower mantle may occur if the timescale of the process is long enough (more than a few tens of million years) and the viscosity increase in the lower mantle is less than one order of magnitude [*Davies*, 1995; *Guillou-Frottier et al*., 1995; *Christensen*, 1996; *Funiciello et al*., 2003].

At subduction zones, sediments, oceanic crust containing a large fraction of water, and mantle lithosphere returns to the Earth's mantle. The initiation of this process begins with the down-bending of the oceanic lithosphere requiring a significant amount of energy. A typical dip angle of the descending lithosphere is around 45°, but dip angle may vary between ~5°-90° [e.g., *Turcotte*, 1982; *Wright*, 1993; *Bevis et al*., 1995; *Martínez et al*., 2000]. It is widely accepted that there is a correlation between slab age and dip. While old, dense lithosphere easily sinks with a steep angle, a younger lithosphere may resist subduction showing shallower dip angles [*Stern*, 2002]. However, this correlation is not

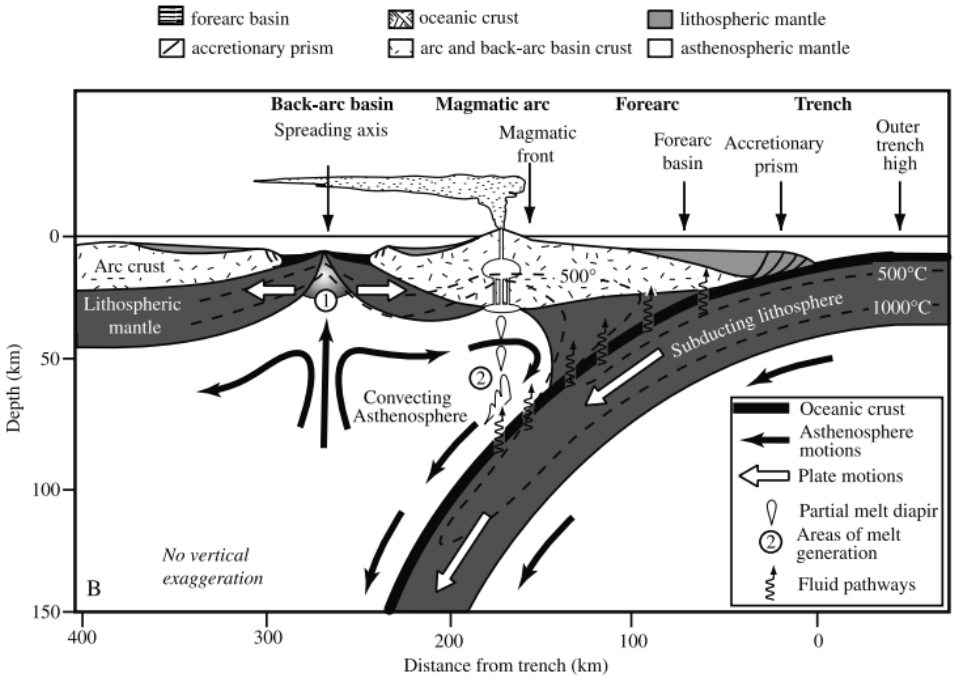

Figure 2.2 Schematic section of a typical subduction zone showing the main components and their interactions. Figure from *Stern* [2002].

unique and additional factors as plate thickness and shape, plate velocities, lateral density variations in the upper mantle and/or effects of accretion/erosion may influence significantly the slab dip angle [*Cruciani et al.*, 2005].

In the overlying lithosphere of a mature and stable subduction zone, important magmatic and tectonic phenomena may occur. This area of a subduction zone is recognized as arc-trench complex and typically presents three components: forearc, magmatic arc and back arc (Figure 2.2). In the forearc, the incoming sediments and rocks of the subducting plate may be accumulated on the upper plate forming an accretionary prism. Sediments, rocks and fluids not emplaced in the accretionary prism are carried out to great depths of the subduction zone. High sedimentation rates also provoke the formation of thick forearc basins between the accretionary prism and the magmatic arc (Figure 2.2). Their formation is also a consequence of permanent deformation of the overriding plate in response to subduction and accretion. Magmatic arcs may be formed as a result of the release of hydrous fluids from the subducted materials drastically reducing the melting temperature of the overlying asthenosphere mantle (Figure 2.2). Moreover, an interesting feature of some subduction zones is the formation of a back-arc basin behind the magmatic arc (Figure 2.2). Although subduction zones are zones of plate convergence, a regressive motion of the trench may occur resulting in extension in the overriding plate [*Elsasser*, 1971; *Lonergan and White*, 1997; *Schellart*, 2004b]. Extensional

forces, rifting and seafloor spreading characterize these regions. Examples of active back-arc basins are the Mariana Trough behind the Mariana arc, the Lau-Havre Trough behind the Tonga-Kermadec arc, the North Fiji Basin behind the Vanuatu (New Hebrides) arc, the Manus Basin NE of New Guinea, and the East Scotia Sea behind the South Sandwich arc [*Stern*, 2002].

It should be emphasized that important geological phenomena occur in subduction zones generating a great impact in society. Indeed, many earthquakes are associated with these zones where seismicity may arrive to 660 km depth. The Wadati-Benioff zone delineates the locations of these intermediate-depth earthquakes that occur within the subducting plate as it descends into the mantle. The descent of young, buoyant oceanic lithosphere produces a strong coupling between the subducted and the overriding plates generating higher magnitude earthquakes than old oceanic lithospheres. Examples of earthquakes in subduction zones are those occurred in Chile in 1960 and in the Indean ocean in 2004, which are the two largest earthquakes in history.

Some volcanism is also associated with subduction. Island arcs or volcanic arcs may be formed on the overriding plate parallel to the trench (magmatic arc; Figure 2.2). The melting of the materials is produced in the mantle wedge (area of melt generation; Figure 2.2). Different processes associated with interactions between the subducting plate and the overlying mantle contributes to the generation of this volcanism. Indeed, frictional dissipation on the fault zone and water released from the heating of hydrated minerals can contribute to melting in the mantle wedge. The Aleutian Islands in the North Pacific are an example of an island arc. In the Western United State a volcanic line extends from Mt. Baker to Mt. Shasta as an example of a volcanic arc. Another example is the Luzon volcanic chain in Philippines where the Mt. Pinatubo provoked one of the most violent volcanic eruption of the 20th century in 1991.

Besides major subduction zones, small-scale subduction systems may show other specific characteristics as shorter and curved trenches, a more diffuse seismicity and non-unique subduction polarity. These characteristics are found in regions characterized by margin segmentation and microplates moving and deforming independently of the major plate. Examples of these complex subduction zones are found in the Pacific ocean (Indonesia and Philippines) [*Hall and Spakman*, 2015] and in the Mediterranean region [Figure 2.3; *Faccenna et al.*, 2010].

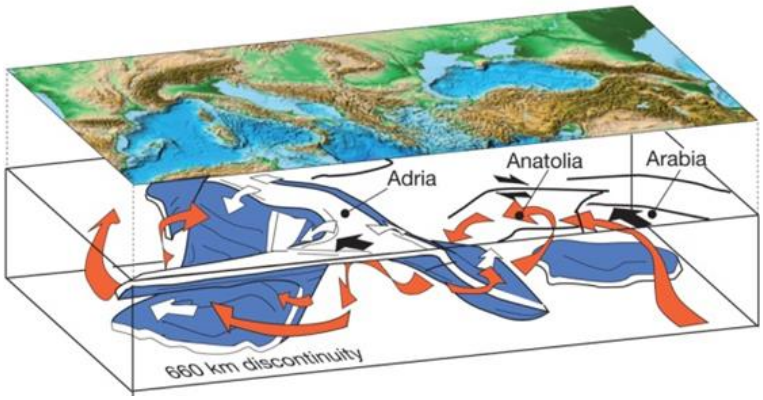

Figure 2.3 Cartoon showing the complex subduction zones and the mantle flow pattern in the Mediterranean region. Figure from *Faccenna and Becker* [2010].

2.1 Subduction dynamics

The dynamics of subduction, involving a single subducting plate, have been extensively studied in the literature [e.g., *Bellahsen et al*., 2005; *Heuret and Lallemand*, 2005; *Lallemand et al*., 2008; *Ribe*, 2010; *Stegman et al*., 2010; *Garel et al*., 2014]. The evolution of the subducting plates depends on the balance between driving and resisting forces, which are not constant in time and depth, and the geometry of the tectonic environment. In nature, there are many forces acting on subduction due to the complexity of the process and their relative importance may vary depending on the age of the subducting lithosphere, the dip angle and mechanical properties, the sinking rate and the duration of the subduction process [e.g., *Billen*, 2008; *Lallemand et al*., 2008; *Kirdyashkin and Kirdyashkin*, 2014]. Here the most relevant forces acting on a single plate subduction system and the basic kinematics are described (Figure 2.4).

The slab pull force, S_p, is the main driving force of subduction and appears as a result of the gravitational instability of the old ocean lithosphere with respect to the mantle acting while the slab sinks pulling the rest of the plate behind it [*Forsyth and Uyedaf*, 1975; *Chapple and Tullis*, 1977; *Carlson et al*., 1983]. The gravitational instability is mainly related to the density difference between the colder subducting slab and the surrounding mantle. Phase changes from olivine to spinel at 410 km depth can enhance the slab pull force, whereas the phase change from spinel to perovskite at 660 km depth has the opposite effect.

Resisting forces include plate bending, $R_{b,}$ frictional plate-coupling, the viscous shear, $V_{d,}$ and the positive buoyancy forces owing to the 660 km phase transition. The plate bending is the main resisting force within the lithosphere and acts continuously as it

descends at the ocean trench and at the 660 km discontinuity if the slab is accommodated over the lower mantle [*Bellahsen et al.*, 2005; *Lallemand et al.*, 2008]. The energy required to bend the plate depends on its viscosity and thickness [*Conrad and Hager*, 1999]. The frictional plate-coupling acts at shallow depths accounting for the coupling of the overriding plate. In the upper mantle, the viscous shear is caused by friction between the descending lithosphere and the mantle. At 660 km depth a positive buoyancy force acts due to the phase transition. In addition to local forces, large scale mantle flow and flow induced by pressure variations may also affect the dynamics of the subduction system [*Billen*, 2008].

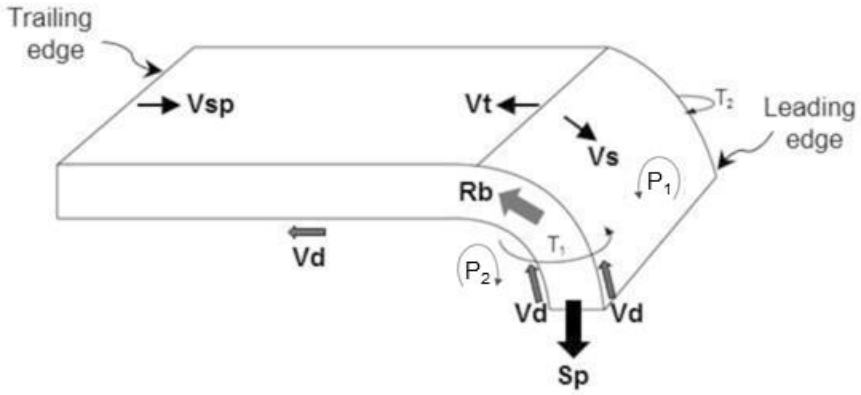

Figure 2.4 Scheme showing the most relevant forces acting on single subduction systems in nature. Slab pull Sp is the driving force while the plate bending Rb and the viscous shear Vd resist subduction. Note that the frictional plate-coupling force is not shown as the overriding plate is not modeled. Kinematically the subduction velocity vs is defined as $v_s=v_{sp}+v_t$, where vsp is the plate velocity and vt the trench velocity. P_1, P_2 denote the poloidal components of the induced mantle flow while T_1, T_2 denote the toroidal components.

Kinematically, the subduction velocity v_s depends on these forces and is described by two main factors: i) the plate advance velocity v_{sp} and ii) the trench velocity v_t, such that $v_s = v_{sp} + v_t$ [e.g., *Lallemand et al.*, 2008] (Figure 2.4). Thereby, subduction zones can be classified depending on the relative velocity of the trench with respect to the plate. When trench velocity is positive, that is the trench moves towards the overriding plate, the process is usually called trench advance, whereas when it is negative, i.e., the trench moves backward with respect to the plate motion, the process is called rollback [e.g., *Elsasser*, 1971; *Garfunkel et al.*, 1986]. The rollback process is characterized by high dipping angle of the slab and slow plate velocities in comparison with the advancing trench mode. In nature we observe both advancing and retreating trenches but the

frequency of one or another process and trench velocities depend on the considered absolute reference frame [*Funiciello et al.*, 2008].

Concerning to retreating trenches (subduction rollback) where $v_s = v_t$, the basic kinematics of a single plate shows a characteristic evolution of the subducting lithosphere during its descent into the upper mantle and its interaction with the 660 km discontinuity [e.g., *Funiciello et al.*, 2003; *Schellart*, 2004a]. This evolution can be divided in three phases characterized by different trench kinematics. During the first phase, before the slab reaches the bottom of the upper mantle, the trench retreats with a fast rate that increases progressively in time with the amount of subducted material. Then there is a short period of low trench retreat velocity during which the leading edge of the slab bends and accommodates on the upper/lower mantle discontinuity. Finally, the trench/slab retreat follows a steady state velocity regime until subduction is completed.

2.2 Mantle flow induced by subduction

The mantle flow induced by a single subducting plate has been studied by many authors [e.g., *Faccenna et al.*, 2010; *Strak and Schellart*, 2014]. During subduction, the movement of the subducting plate drags by friction the surrounding mantle which acts as a fluid and generates a characteristic mantle flow. In the case of a rollback process, the induced mantle flow can be described into two principal components: poloidal and toroidal (Figures 1.3 and 2.4). The poloidal component, associated with the vertical mass transport, is generated on the mantle wedge and behind the slab forming two flow cells on a vertical plane. The toroidal component is composed by two flow cells around the lateral edges of the slab, transporting material from behind the slab to the mantle wedge. It has been observed that both components exist during all the subduction process although they exhibit different circulation regimes depending on the evolutionary stages.

Toroidal flow becomes especially important during the steady state regime of the subduction rollback process, when the trench retreat rate and the slab dip angle become nearly constant [*Funiciello et al.*, 2006]. The mantle material located beneath the slab flows laterally from both sides of the slab producing vortex-like structures (Figures 1.3 and 2.4). The importance of this component has been studied by several authors [e.g., *Funiciello et al*., 2003; *Funiciello et al*., 2004; *Funiciello et al*., 2006; *Stegman et al*., 2006] stressing the need of the three dimensional modeling, as it turns out to have significant influences in the subduction process. Actually, the curved geometry observed in many

trenches is related to the toroidal flow pattern in front of the trench, which results to be more vigorous in the center than at the edges [*Jacoby*, 1973; *Schellart*, 2004a; *Morra et al.*, 2006; *Stegman et al.*, 2006; *Schellart et al.*, 2007; *Loiselet et al.*, 2009; *Schellart* 2010a]. This curvature effect depends on the plate and mantle rheologies and turns out to be more important in narrow plates (≤ 1500 km) where nearly the 70% of the negative buoyancy force of the slab is used to drive the toroidal flow [*Schellart*, 2004b; *Stegman et al.*, 2006]. Furthermore, toroidal flow is proposed to explain the existence of intraplate volcanism near slab edges [e.g., *Strak and Schellart*, 2014] as it is the case of Mount Etna, located at the southern edge of the Calabrian slab [*Faccenna et al.*, 2010; *Schellart*, 2010b] and control the mantle mixing [e.g., *Guillaume et al.*, 2010].

On the other hand, the poloidal component is dominant during the first stage of the slab sinking and drives the deformation of the overriding plate [e.g., *Funiciello et al.*, 2003; *Schellart and Moresi*, 2013; *Sternai et al.*, 2014]. It reaches the maximum vigor just before the slab encounters the 660 km discontinuity and involves an upwelling component in the mantle wedge that may also be a source of intraplate volcanism in the back-arc region over a width extent equivalent to the plate width [*Faccenna et al.*, 2010; *Strak and Schellart*, 2014].

Evidence for poloidal and toroidal mantle flow is supplied by different geological, geophysical and geochemical methods. Seismological and geodetic observations provide direct constraints and evidences of short-term mantle circulation through present-day kinematic vectors and shear-wave splitting analysis [e.g., *Long and Silver*, 2008*; Díaz and Gallart*, 2014; *Long*, 2016; *Palano et al.*, 2017]. Magmatism and basalt geochemistry in terms of major and trace elements, as well as isotopic compositions, is also used to obtain information about poloidal/toroidal mantle flow linked to subduction [e.g., *Faccenna et al.*, 2010; *Mullen and Weis*, 2015].

2.3 Double subduction systems

Besides single plate subduction, different configurations of double subduction systems have been observed to occur in nature (Figures 1.2 and 2.5). The dynamics of such systems is still poorly understood but some recent studies indicate the complexity of these processes. The presence of nearby slabs may affect the evolution of the system to a greater or lesser extent depending on its configuration.

A double-sided subduction system consisting of a single plate subducting from both sides (Figure 2.5A), has been recognized to occur in the Molucca Sea in Eastern Indonesia [*Di Leo et al.*, 2012], and in the Mediterranean at the two sides of the Adria plate [*Faccenna et al.*, 2014b]. 3D numerical models by *Di Leo et al.* [2014] show that trench-parallel sub-slab seismic anisotropy is stronger than in a simple subduction configuration due to the different pattern of the induced mantle flow. Moreover, analog models performed by *Király et al.* [2018b] show that when trenches are closer than 480 km there is an interaction between the induced mantle flow of each slab resulting in an increment of the dynamic pressure in the sub-slab area and in a slow-down of the subduction process.

A double subduction system with parallel trenches in which two plates are subducting simultaneously in the same direction (Figure 2.5B), is thought to be involved in the formation of the Himalaya [e.g. *Burg et al.*, 2006] and the active Izu-Bonin-Marianas and Ryukyu arcs in SE Asia [e.g. *Lallemand et al.*, 2001]. *Mishin et al.* [2008] investigated the influence of converge rate, intermediate plate length, activation volume of the mantle dislocation creep and age of the lithosphere in the evolution of such a system by 2D numerical modeling. Their results show that subduction rates of both plates differ and vary in time even when the total convergence rate remains constant. Relative rates of the converging plates, slab ages and length of the middle plate influences the strength of each subduction zone. They also observe that this type of double subduction involve specific geodynamic processes that are not present in simple subduction systems such as eduction, subduction re-initiation, subduction flip and turn-over of detached slabs. Moreover, *Čížková and Bina* [2015] demonstrate that trench advance can occur in such unusual geometry providing a new geodynamic study of the process.

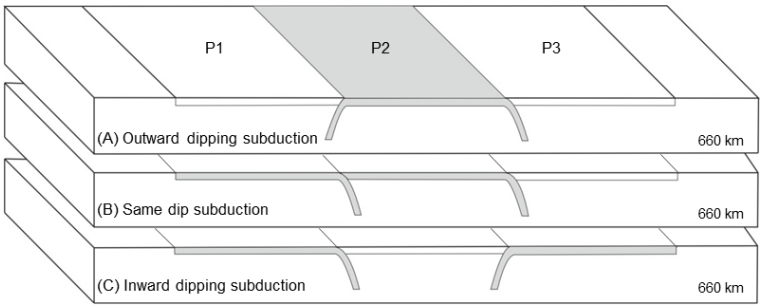

Figure 2.5 Cartoon showing different configurations of double subduction systems with parallel trenches. (A) Outward dipping subduction (double-sided subduction): P2 subducting from both sides, (B) Same dip subduction: P1 and P2 subducting simultaneously in the same direction and (C) Inward dipping subduction: P1 and P3 dipping simultaneously in opposite directions. Modified from *Holt et al.* [2017].

More recently, *Holt et al.* [2017] performed 3D numerical models of double subduction systems with parallel trenches including a new configuration with inward dipping slabs. Their results show that differences between single and double subduction systems involve trench geometry and dip direction affecting to the plate coupling force and mid-plate stresses.

The process studied in this thesis is the double polarity subduction, i.e. double subduction with opposite polarity in adjacent plate segments (Figure 1.3). As mentioned in the Introduction, double polarity subduction has been proposed to occur in the Westernmost Mediterranean region among other places (Figures 1.1 and 1.2) but the complexity of this process remains unknown. The interaction between the induced mantle flows of both plates is expected to modify the evolution of the system, in terms of velocities, stresses and plate deformation. Moreover, the evolution of this process may depend on the relative position of the trenches. While trenches are far away, little or no interaction is expected but as the trenches get closer, the toroidal cells in the inter-plate region will interact modifying the stability of the system. The interaction is expected to be maximum when trenches cross to each other and to vanish as trenches diverge.

Previous numerical models of double polarity subduction performed by *Király et al.* [2016] show that the subduction trench migration is delayed respect to a single plate subduction and stresses in the inter-plate region increases when plate edges are at distances of $d < 600$ km. The interaction is stronger for near plate configurations ($d = 62.5$ km) showing different stress distribution and mantle flow pattern depending on the relative position of the trenches. Indeed, during the first phase (phase 1), while the two slabs sink into the mantle before they reach the 660 km discontinuity, the stress increases around the slabs due to the sinking of the plates. During the second phase (phase 2), coinciding with the acceleration of slab rollback after the slabs interact with the upper-lower mantle boundary, the toroidal flow cells merge and stress increases in the inter-plate region. During the third phase (phase 3), after the trenches become aligned with each other (intersection) until the end of the subduction process, the mantle flow slows down and the stress in the mantle increases at shallows depths.

However, these results cannot be generalized since they are subjected to the modeled geometry of the system, with plates having a width greater than 3000 km and spaced laterally 600-62.5 km, and the assumed boundary conditions as mentioned in the Introduction. In this thesis the study of subduction systems with opposite polarity in

adjacent plate segments is extended using a different geometry and boundary conditions and applying both analog and numerical modeling methods.

CHAPTER 3

Fundamentals

Chapter 3

Fundamentals

Tectonic processes occur in a spatial and temporal scale that makes direct observations very difficult. Same as other geophysical processes, subduction occurs mostly at depth and therefore its dynamics must be inferred from indirect observations, In this context, modeling is a valuable tool that allows to "observe" the process and to validate its physical soundness. Moreover, models are excellent to generate new ideas and hypothesis. Models used here are of two kind, numerical and analog. These two approaches provide with different and complementary views of the processes, although, both are trying to reproduce the same reality and, therefore, the physical model behind them is the same: the basic laws of physics. In this case, the fluid behavior is described by the conservation of mass and momentum, in some simplified form. Conservation equations are closed with an appropriate constitutive law. These equations are described in Sections 3.1 and 3.2. The modeling approaches are presented in Sections 3.3 and 3.4.

3.1 Rheology of the Earth

Rheology deals with the study of deformation and the flow of materials. A variety of rheological behaviors exist in nature depending on the material considered and the external parameters such as pressure, temperature and time. That is, Earth's rocks may deform elasto-visco-plastically depending on the timescale of applied stresses and relaxation times.

Rheologicaly, a material is considered a fluid when it flows under constant stress, independently on its atomic structure. Nowadays, it is generally accepted that over long

time scales (>10^4 years) the hot solid mantle rocks behave as a pure viscous fluid [*Turcotte*, 1982]. This fluid-like behavior of the Earth's mantle was first established by gravity studies at the end of the nineteenth century and the order of its viscosity quantified (10^{20} Pa·s) by Haskell in 1935 [*Haskell*, 1935].

The rheological behavior of the lithosphere is more complex as it includes a range of temperatures from cold to a substantial fraction of the melting point. Concerning to subduction processes, some authors suggest that elasticity play an important role in initiating the subduction, forming instabilities or leading to enhance slab rollback [*Lallemand and Funiciello*, 2009]. However, when subduction initiation is not considered, the slab behavior over long time scales several authors consider it as visco-plastic. For example, *Schmeling et al.* [2008] propose that subduction dynamics is not significantly affected by elasticity. The viscous or visco-plastic approach for the slabs is supported by several geophysical evidences [*Lallemand and Funiciello*, 2009], and largely used in the literature for modeling subduction processes [e.g., *Bellahsen et al*., 2005; *Funiciello et al*., 2006; *Zlotnik et al.*, 2007; *Funiciello et al*., 2008; *; Schmeling et al*., 2008; *Faccenna et al*., 2010; *Capitanio*, 2014; *Strak and Schellart*, 2014; *Király et al.*, 2015; *Király et al*., 2016; *Holt et al*., 2017].

3.2 Mechanical flow problem

On long time scales rocks behave like slowly creeping fluids, therefore geodynamic processes, as subduction, are fairly described by the equations of fluid dynamics. Changes in temperature play an important role in geodynamics and might be coupled to material deformation although, for simplicity, models presented in this thesis do not include the thermal energy balance explicitly and its effect is only considered by assigning the proper physical properties (e.g. density and viscosity) to the different bodies. Cold lithosphere has larger viscosities and densities than the hotter mantle material.

3.2.1 Incompressible mass conservation

The conservation of mass in a continuous medium is described by the continuity equation, which in the Lagrangian description (i.e. for a moving point of reference) is expressed as,

$$\frac{D\rho}{Dt} + \rho\nabla \cdot \vec{v} = 0, \tag{3.1}$$

where ρ is the density and $\vec{v}$ the velocity vector.

In numerical geodynamic modeling, an incompressibility condition (i.e. density of materials is considered constant) is broadly used [e.g., *Tackley*, 2008; *Gerya*, 2009]. The mass conservation under incompressible assumption reads,

$$\frac{\partial v_i}{\partial x_i} = 0, \tag{3.2}$$

where i is the coordinate index, x_i is the *i-th* component of the spatial coordinate (x,y,z) and v_i the *i-th* component of the velocity vector (v_x,v_y,v_z).

3.2.2 Stress and strain

Stress is defined as a force per unit area and reflects the internal distribution and the intensity of the force acting at any point within a continuum in response to internal and external loads applied. The stress is characterized by a tensor, σ_{ij}, which in a 3-dimensional problem has 9 components. A stress component that is orthogonal to a surface of the unit element acting is called a normal stress component (located in the main diagonal of the matrix), and the components which are parallel to the surface, shear stress components (located off diagonal of the matrix).

In geosciences, it is often convenient to define the deviatoric stresses (σ_{ij}') which are deviations of stresses from the hydrostatic stress state (all shear stresses are zero and all normal stresses are equal to each other),

$$\sigma'_{ij} = \sigma_{ij} + P\delta_{ij,} \tag{3.3}$$

where i and j are the coordinate indices, P is the pressure and δ_{ij} is the Kronecker's delta function.

Moreover, the second invariant of the deviatoric stress tensor (σ_{II}) is a scalar value, commonly used as it does not depend on the coordinate system and characterizes the local deviation of stresses in the medium from the hydrostatic state,

$$\sigma_{II} = \sqrt{1/2\sigma_{ij}'^2}, \tag{3.4}$$

Here, Einstein convention is used and the repeated indices (repeated by the square) imply summation along i and j.

The amount of deformation is characterized by the strain tensor (ε_{ij}) defining the total amount of deformation compared to the initial state,

$$\varepsilon_{ij} = \frac{1}{2}\left(\frac{\partial u_i}{\partial x_j} + \frac{\partial u_j}{\partial x_i}\right), \tag{3.5}$$

where u_i and u_j are components of material displacement vector $\vec{u} = (u_x, u_y, u_z)$, and x_i and x_j are the components of the spatial coordinate (*x,y,z*).

While the strain tensor characterizes the deformation in solid materials, fluids are described by the strain rate tensor $\dot{\varepsilon}_{ij}$,

$$\dot{\varepsilon}_{ij} = \frac{1}{2}\left(\frac{\partial v_i}{\partial x_j} + \frac{\partial v_j}{\partial x_i}\right), \tag{3.6}$$

where v_i and v_j are the components of the velocity vector $\vec{v} = (v_x, v_y, v_z)$.

By analogy to the stress tensor, the deviatoric components of the strain rate tensor ($\dot{\varepsilon}'_{ij}$) and the second invariant of the deviatoric strain rate ($\dot{\varepsilon}_{II}$) are also defined as,

$$\dot{\varepsilon}'_{ij} = \dot{\varepsilon}_{ij} - \delta_{ij}\frac{1}{3}\dot{\varepsilon}_{kk}, \tag{3.7}$$

$$\dot{\varepsilon}_{II} = \sqrt{1/2\dot{\varepsilon}'^2_{ij}}, \tag{3.8}$$

where *i,j* and *k* are coordinate indices and $\dot{\varepsilon}_{kk} = \dot{\varepsilon}_{xx} + \dot{\varepsilon}_{yy} + \dot{\varepsilon}_{zz}$.

Finally, the Newtonian law of viscous friction is widely used in geodynamic modeling and relates the shear stress and the shear strain rate. Under the incompressible fluid approximation (equation 3.1), it can be simplified to,

$$\sigma'_{ij} = 2\eta\dot{\varepsilon}_{ij,} \tag{3.9}$$

where η is the viscosity of the material which characterizes the degree of resistance to shear deformation and strongly depends on pressure and temperature [*Ranalli and Murphy*, 1987].

3.2.3 The momentum equation

The conservation of momentum for a continuous medium in the gravity field is derived from the Newton's second law of motion ($\vec{F} = m\vec{a}$) and is expressed as follows,

$$\frac{\partial \sigma'_{ij}}{\partial x_i} + \rho g_i = \rho\frac{Dv_i}{Dt}, \tag{3.10}$$

where g_i is the *i-th* component of the gravity vector $\vec{g} = (g_x, g_y, g_z)$, ρ is the density and $\frac{Dv_i}{Dt}$ is the substantive time derivative of *i-th* component of the velocity vector.

The so-called Navier-Stokes equation of motion is obtained from equations 3.3 and 3.10, and describes the conservation of momentum for a fluid in the gravity field,

$$\frac{\partial \sigma'_{ij}}{\partial x_j} - \frac{\partial P}{\partial x_i} + \rho g_i = \rho \frac{Dv_i}{Dt}. \tag{3.11}$$

In highly viscous fluids, as the Earth mantle, the inertial forces, $\rho \frac{Dv_i}{Dt}$, are negligible with respect to viscous resistance and gravitational forces (infinite Prandtl number limit) [e.g., *Donea and Huerta*, 2002; *Gerya*, 2009], and the Navier-Stokes equation (3.11) simplifies to the Stokes equation of slow flow,

$$\frac{\partial \sigma'_{ij}}{\partial x_j} - \frac{\partial P}{\partial x_i} + \rho g_i = 0. \tag{3.12}$$

3.2.4 Constitutive equations

As mentioned in Section 3.1, viscous and/or visco-plastic approaches are commonly used to simulate the mantle and the lithosphere in subduction experiments. In the experiments presented here, the mantle is always modeled as a Newtonian fluid ($\eta \approx cte$). For the lithosphere, the viscosity, η, is assumed to be constant in each material or strain-rate dependent.

The non-linear, strain-rate dependent viscosity for the lithosphere is considered and calculated according to the following expression [*Ranalli and Murphy*, 1987],

$$\eta_l = \eta_0 \cdot \dot{\varepsilon}_{II}^{\left(\frac{1}{n}-1\right)}, \tag{3.13}$$

where η_0 denotes the reference viscosity, n is the power-law exponent and ε_{II} the second invariant of the strain-rate tensor.

The visco-plastic rheology represents the crust layer of the oceanic lithosphere, mimicking weakening that occurs during bending. After reaching an absolute shear stress limit, σ_{yield}, plastic yielding occurs and it is implemented through the Byerlee's criterion,

$$\sigma_{yield} = c_0 + \mu \rho g z, \tag{3.14}$$

where c_0 is the cohesion at zero confining pressure, μ is the friction coefficient, g is the gravity and z is the depth.

3.3 Analog Modeling

The study of geodynamic processes in a laboratory began 200 years ago. Sir James Hall was the first scientist to develop a laboratory experiment to study the folding of layered sedimentary rocks [*Hall*, 1815]. The scaling theory, later improved by many scientists [*Hubbert*, 1951; *Ramberg*, 1967; *Ramberg*, 1981; *Weijermars and Schmeling*, 1986; *Davy and Cobbold*, 1991; *Richard*, 1991; *Ribe and Davaille,* 2013] was firstly developed by Hubbert in 1937 providing new insights in quantifying the results obtained and compared them with the natural prototype [*Hubbert*, 1937]. Laboratory experiments of plate tectonics started to be performed in the 1970s. The first subduction analog models were developed by Jacoby in 1973 using water and a rubber sheet to model the mantle and the subducting plate [*Jacoby*, 1973]. Since then, a wide variety of analog materials with different rheological peculiarities have been used in subduction experiments [*Schellart and Strak*, 2016].

3.3.1 Modeling subduction

Materials used in analog modeling simulate the physical behavior of natural rocks. Commonly used materials in subduction experiments are the glucose syrup and the silicone putty to simulate the long-term viscous behavior of the mantle and the plate respectively [e.g., *Funiciello et al*., 2003; *Bellahsen et al*., 2005; *Funiciello et al*., 2006; *Funiciello et al*., 2008; *Guillaume et al*., 2009; *Guillaume et al*., 2010; *Duarte et al*., 2013; *Guillaume et al*., 2013; *Strak and Schellart,* 2014; *Király et al.*, 2018a]. Models using these materials and approximating the lithosphere as a single viscous layer under isothermal conditions are used to study the consequences of the different driving and resisting forces on the subduction process. This approach of the lithospheric strength profile (Figure 3.1), despite not being very detailed, prevents the simulation of strain localization in the lithosphere, which actually occurs in a generalized and distributed manner and allows the experiments to be completely dynamic [*Chen et al.*, 2016; *Schellart and Strak*, 2016].

Other analog modeling approaches, using diverse analog materials, are also used in subduction experiments according to the specific needs. Indeed, some models consider the lithosphere with a rheological layering to allow investigate the effect of the strength of the brittle and ductile layers on subduction evolution. Moreover, a vertical temperature gradient may be imposed to simulate a temperature-dependent lithospheric strength profile. This approach allows simulating the effect of temperature variation during the deformation of the model [*Chemenda et al*., 2000; *Boutelier et al*., 2003; *Boutelier and*

Oncken, 2011; *Boutelier and Cruden*, 2013]. In addition, kinematic and material inflow conditions may be applied during the course of the experiment being slab motion externally controlled [e.g., *Buttles and Olson*, 1998; *Kincaid and Griffiths*, 2003; *Kincaid and Griffiths* 2004; *Druken et al*., 2011; *Druken et al*., 2014; *MacDougall et al*., 2014].

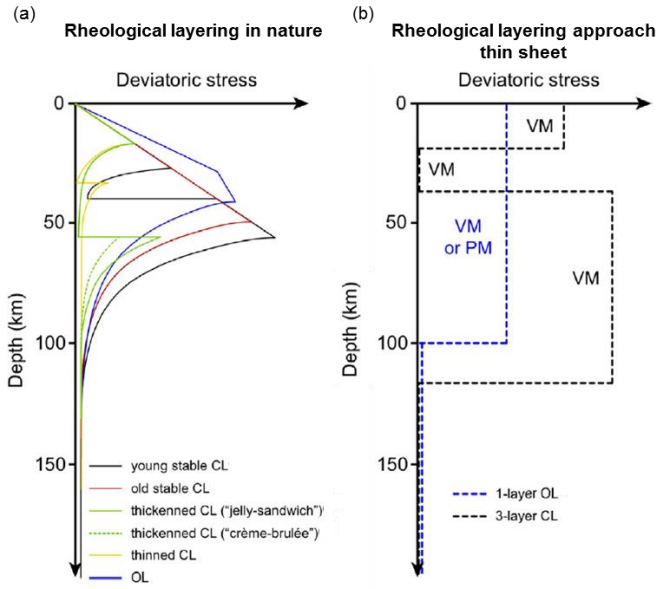

Figure 3.1 Schematic strength profiles of the rheological layering observed in nature and the thin sheet approach used in modeling geological and geodynamic processes. OL: oceanic lithosphere. CL: continental lithosphere. VM: viscous materials. PM: plastic materials. Modified from *Schellart and Strak* [2016].

3.3.2 Analysis and visualization

Monitoring and subsequent data analysis of the experiments are key factors to obtain relevant results. Due to the continuous technological advances, this process is continuously improved every day. Commonly, analog modelers record pictures of their experiments at a constant rate allowing visualizing the evolution of the model. In this way, the experiment can be later analyzed through post-processing tools. The type of images recorded depends on the purpose of the experiment. In general, two or three different views (top and sides) are employed to obtain information about the evolution of the model at surface and at depth. Moreover, to investigate the kinematics of subduction experiments, reference marks as bands, lines, and circles may be drawn in the model [e.g., *Funiciello et al*., 2003; *Schellart*, 2004a*; Duarte et al*., 2013; *Chen et al*., 2016]. Moreover, the different colors of the materials used may provide a good contrast using them as markers [e.g., *Schellart*, 2004a]. To study the mantle flow pattern on analog subduction

models, tiny air bubbles may be created within the viscous fluid representing the mantle (e.g., glucose syrup) to manually track their trajectory using post-processing tools [*Schellart*, 2008; *Schellart* 2010a]. A more detailed description of the recording and quantification in analog modeling, as well as approaches, scaling and materials used can be found in [*Schellart and Strak*, 2016].

3.3.3 Preparation of the experiment

Analog models require a thorough preparation before running the experiment. In this sub-section, the experimental procedure of the analog models of double polarity subduction presented in this thesis is detailed.

Materials and its initial layout are chosen depending on the specific goals of the experiments. A series of experiments is defined to test the influence of one or several parameters in the behavior of the system. As many previous analog models of subduction systems, a high density and low viscosity syrup is used to simulate the mantle as a Newtonian fluid, and silicone putty is used to simulate the oceanic plates as a single thin sheet.

The experiments are performed in a 150 x 150 x 50 cm^3 Plexiglas tank filled with the syrup (Figure 3.2). An impermeable layer is placed at 11 cm depth as analog of the upper/lower mantle boundary. Two cameras are placed to obtain pictures of the model from the top and an oblique position during the development of the experiment.

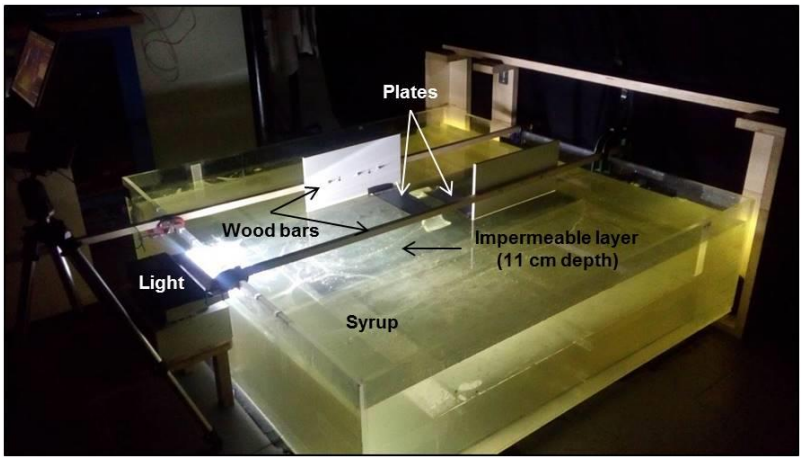

Figure 3.2 Real experimental setup. The tank is full of viscous syrup representing the mantle. The plates are made of silicone putty and fixed at their trailing edge to a wood bar. The experiment is illuminated with a light from a side position.

The density contrast of the lithosphere with respect to the mantle is controlled by adding iron fillings to the silicon representing the plate (Figure 3.3a). This has a negligible effect on its rheology. The mixing takes about 3-4 days until the mixture is uniform. The physical properties of the mixture are given in Chapter 4 (Section 4.1.2). The second step is to shape the plates; the silicone putty must have the dimensions and thickness required by each experiment. This is done using molds. Due to the high viscosity of the silicone, around 24 hours are required for the silicone putty to sit on the mold (Figure 3.3b). An important factor to control during the preparation of the plates is the occurrence of air bubbles within the silicone, as they can cause a variation in its density largely affecting the evolution of the model. To avoid this problem, air bubbles within the plates are continuously checked and punched with a needle to remove them. The viscosity contrast between the lithosphere and the mantle is controlled in the models by changes in temperature. This is effective as the viscosity of the syrup representing the mantle has a much stronger dependence on temperature than that of the silicone putty. Due to the dimensions of the tank, the easier way to control its temperature is by controlling the room temperature. Therefore, the laboratory temperature must be checked and corrected continuously before and during the experiments. Its values must remain between 21 ºC and 22 ºC.

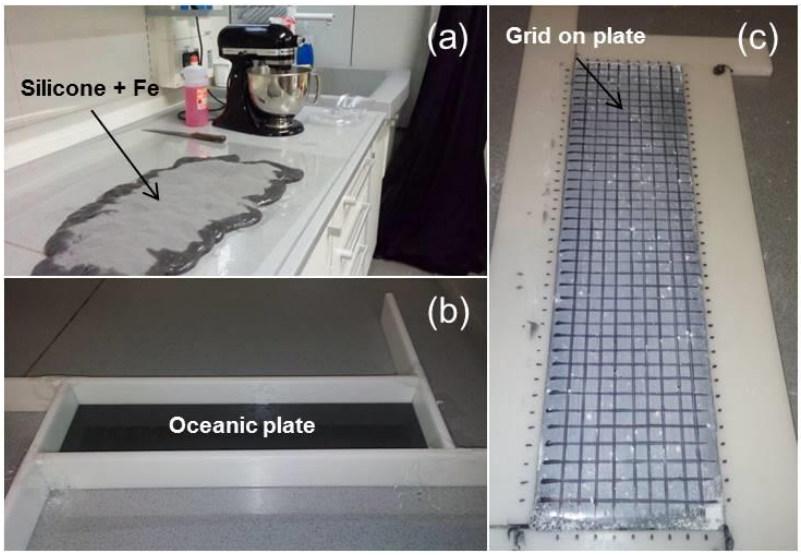

Figure 3.3 Images showing the oceanic plates preparation (a) Mixing pure silicone with Fe fillings. (b) Silicone putty sitting in a mold to produce an oceanic plate shape. (c) A grid is drawn on top of the silicone putty to observe and measure deformation.

Just before the initiation of the experiment, a grid is drawn on the plates to be used as markers and be able to analyze their deformation during the entire evolution (Figure 3.3c). Two other steps must be taken into account regarding the preparation of the syrup. First, syrup reacts with air and tends to crystalize forming a thin but hard layer on its surface that might interfere with the normal behavior of the experiments. To avoid this hard layer during the experiment, the syrup must be thoroughly stirred before starting the experiment. Second, the movement of the mantle can be observed by tracking the movement of air bubbles. The stirring, therefore, has also the role of creating micro-bubbles within the syrup. The experimental setup is completed by preparing the cameras, the computers, the light that illuminates the experiment and mounting the wood bars for fixing the trailing edges of the plates in order to simulate the rollback behavior (Figures 3.2 and 3.4).

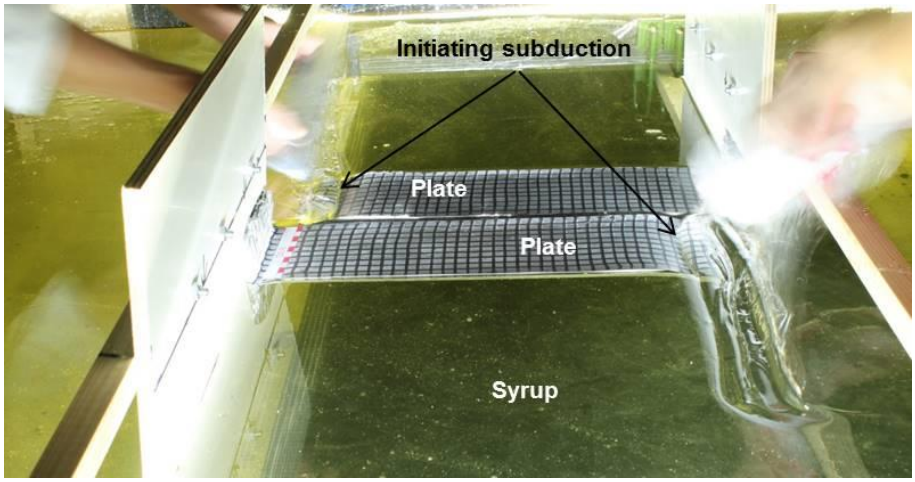

Figure 3.4 Image showing how plate subduction is initiated in the laboratory. The process is initiated by sinking simultaneously both plates into a depth of ~3 cm.

The process of placing the plates on the syrup is one of the most difficult tasks in preparing the experiment. The plates start deforming as soon as they are out of the mold, so they must be placed on the syrup as quick as possible without imposing any deformation on them and in the right location. Moreover, once on the syrup, the plate's trailing edges are attached to the woods. Finally, subduction is started by pushing down the slabs by adding some syrup on top of the leading edges of the plates (Figure 3.4). During the experiment, the two cameras record pictures every 30 seconds and their

operation is continuously controlled. The duration of the experiment depends on the model configuration and might be around 3-4 hours.

Once the experiment has finished, the subducted plates must be recovered and cleaned as they will be reused in the next experiment. Silicone putty and syrup cleaning (removing any amount of syrup that might have been mixed with the silicone putty and vice-versa) is key to keep the physical properties of the materials unaltered (densities and viscosities). While not used, the syrup tank must be kept covered to minimize crystallization. Finally, the laboratory temperature is kept to the desired value and controlled during all the experimental period to guarantee that the temperature of the materials, especially glucose syrup within the tank is homogeneous.

3.4 Numerical Modeling

The first 2D numerical model of subduction was performed in 1970 [*Minear and Toksöz*, 1970], when the Plate Tectonics theory was broadly accepted. Since then, numerical techniques have improved rapidly providing a useful tool to better understand subduction processes and the complex dynamics of the Earth in general. However, numerical geodynamic modeling requires advanced computational techniques consuming large amounts of computer sources. The size of the problems, particularly in three dimensions, requires the use of high performance parallel computers to carry out many calculations simultaneously. Actually, the first 3D numerical models, with the objective of study the mantle convection, were performed in 1985 [*Baumgardner*, 1985; *Machetel et al.*, 1986].

3.4.1 Numerical approaches

The equations of conservation of mass and momentum presented in Section 3.2 do not present a closed analytical solution. The velocity and the pressure, therefore, must be obtained using numerical approximate methods. There are many techniques proposed to attack partial derivative equations (PDE), two of the more usual are the Finite Difference (FD) and the Finite Element (FE) methods. These techniques have their own properties and each one behave better under different conditions. Different authors, therefore, make use of one or the other depending on their preferences and situations. In geodynamics both are widely used.

Finite Differences are based on linear expressions that approximate derivatives. These approximations are based on a regular grid of points (or mesh) that somehow determines the accuracy of the approximation. The system of partial differential equations is transformed into a system of algebraic equations that are simpler to solve [e.g., *Gerya*, 2009; *Patankar*, 1980]. In the case of linear PDE the system obtained is a system of linear equations that can be solved by many well known methods.

Finite Elements, on the other hand, transform the PDEs into equivalent integral equations that are approximated in a mesh having less restrictions than FD [e.g., *Oden*, 1991]. After discretization, FE also generates a system of linear equations but this system is usually a bit more expensive to construct than in the case of FD.

Both methods rely on a mesh. The fields can be described in the mesh in two different ways: in an Eulerian framework or in a Lagrangian framework. In an Eulerian description the knots or nodes of the mesh are fixed in space and the material "flows" on top of it. This is commonly used to describe large deformations and fluid behavior. In a Lagrangian description, the nodes are attached to the material and move when the material deforms. This description is used mostly in the description of solids and in multiphase problems.

Geodynamic simulations are complex. They involve large deformation of mantle material, better described in an Eulerian framework, and multiple materials easier to describe in a Lagrangian framework. In practice, geodynamic models require a combination of both Eulerian and Lagrangian descriptions. This combination is used in most codes, independently of the discretization technique chosen.

The wide range of physical and temporal scales, and the many coupled physical processes also impose a need for computational efficiency. These codes are continuously improving and the increase of computational resources and parallelization allow carrying out higher resolution models with sophisticated and more realistic rheologies and processes.

3.4.2 Applied numerical codes

In this thesis, two different numerical codes have been applied to perform 3D numerical subduction experiments: i) *UNDERWORLD*, developed in Melbourne University, Australia and ii) *I3ELVIS,* developed at ETH Zurich, Switzerland. Both codes have been tested in real geodynamic studies.

UNDERWORLD [*Moresi et al.*, 2003] solves the mechanical flow problem using mixed finite elements with unknowns of velocities and pressures. The code is open source and can be freely downloaded. It is designed to be expandable with the aim of simplifying the addition of new processes and equations. It is implemented in the C language and uses a distributed memory approach that allow for very large scalability in parallel.

I3ELVIS [*Gerya and Yuen*, 2007] uses finite differences for the discretization. It uses a staggered grid with velocities, pressures, stresses and strain rate unknowns. The code is proprietary and cannot be obtained without authorisation of the authors. It is highly optimised for geodynamic simulation, implemented in the C language and uses a shared memory model that is faster than the distributed memory, but less scalable.

Both codes used a mixed Lagrangian-Eulerian approach with Particle-in-Cell (PIC) [PIC, *Harlow*, 1955] to describe phase location and transport the material properties and history. That is, material deformation is tracked on moving material points which are then used to create the integrals in the finite element form, combining therefore a standard Eulerian Finite Element mesh with Lagrangian particles. The Stokes problem is solved with the Uzawa method and its inner iterations are solved using a multigrid technique.

UNDERWORLD and *I3ELVIS* allow calculating complex multiphase visco-plastic and thermo-mechanical problems with strong variations in viscosity and thermal conductivity. They can be run on a local machine although for 3D high resolution models, a cluster is necessary. The codes are supported on Linux-based OS (desktop and supercomputers) and Mac OS X (Power PC and Intel). They require 300-500 MB for a compiled copy of the code, 340 MB for software dependencies and enough space for the output data (~270 GB-1TB/model).

3.4.3 Modeling subduction

Modeling implies simplification and abstraction. In the case of a subduction system, nature is extremely complex involving a wide variety of physical and chemical processes and multi scales in time and space. The model used will depend on the particular process that is under study. A variety of approaches are commonly used to explore different aspects of the subduction system. The choice of the model type is set by determining the appropriate domain size, the effects of boundary conditions, the material properties and the observations to which the model results are compared. Some subduction models incorporate temperature dependence [e.g., *Zlotnik et al*., 2007; *Mishin et al*., 2008*; Duretz et al*., 2012; *Chertova et al*., 2014; *Ruh et al*., 2015]. Others, for computational simplicity,

consider the problem as purely mechanical, where only buoyancy forces within the system drive the flow [e.g., *OzBench et al*., 2008; *Mason et al*., 2010; *Capitanio*, 2014; *Capitanio et al.*, 2015]. This simplification is commonly used in 3-dimensional modeling where models are computationally exhausting.

Different restrictions may be applied to the boundaries of the numerical box domain. That is, boundary conditions are free-slip (stress tangential to the boundary and velocity perpendicular to the boundary are zero), no-slip (stresses and velocities on the boundary are zero) and/or periodic (flow out on one side boundary reenters the box on the opposite side boundary). In addition, some dynamic models apply kinematic boundary conditions that change with time to explore how plate kinematics is related to the slab dynamics in the mantle.

The mantle is modeled with a linear (Newtonian) rheology. The 660 km discontinuity can be modeled as a viscosity jump of several orders of magnitude (e.g., $\eta_{lm}{\sim}10^2\eta_{um}$, being η_{lm} the viscosity of the lower mantle and η_{um} the viscosity of the upper mantle) [e.g., *Stegman et al*., 2006; *Yamato et al*., 2009; *Mason et al*., 2010], or by a no-slip rigid boundary when simulating slabs that do not penetrate to the lower mantle [e.g., *Schellart and Moresi*, 2013; *Farrington et al*., 2014; *Király et al*., 2017]. The latest assumption is frequently applied as a first-order approximation of the 660 km discontinuity with the main objective of reducing the size of the computational domain.

Concerning to the slab, a three-layered rheology representing a first-order approximation of an oceanic lithosphere profile is commonly used in numerical modeling [*Stephenson and Cloetingh*, 1991]. In this case, the decoupling of the slab from the surface is handled by implementing plastic rheology to the top layer, defining the crust (see also Section 3.2.4). This creates a shear zone that decouples the subducting plate from the top of the surface [e.g., *Christensen*, 1996; *Tetzlaff and Schmeling*, 2000; *Schellart and Moresi*, 2013; *Király et al*., 2016]. As in analog modeling, other numerical models of subduction have adopted a purely viscous slab [e.g., *Schmeling et al.*, 2008]. In this case, the decoupling of the slab from the surface is handled by adding a sticky-air layer: a low-density, low-viscosity phase imposing low shear stresses along its interface with the mantle/plate and allowing the system to develop a surface topography.

Another common assumption in subduction experiments is to neglect Earth's sphericity. Although it may be an influential factor in large-scale subduction systems, it has been demonstrated to have negligible effect on the subduction dynamics [*Morra et al.*, 2006].

3.4.4 Analysis and visualization

The results of numerical models are post-processed and analyzed through a wide variety of 3D visualization and data analysis programs. In this thesis, the *ParaView* [Kitware Inc.] software is used to obtain a 3D dynamic view of the models and to analyse physical parameters such as mantle velocities, effective stresses (equation 3.3) within the plates and the mantle and plates deformation through the effective strain rate (equation 3.7). Moreover, numerical computing softwares as *Matlab* [Mathworks, Inc.] can be used to calculate trench retreat velocities by identifying the position of the center point of the trench in each saved time step of the evolution. The accuracy of this calculation is mostly determined by the resolution of the model. The energy dissipation rate ($dW = dt \cdot \dot{\varepsilon}_{ij} \cdot \tau_{ij}$) within the model is also calculated and plotted through the *Matlab* software.

3.5 Analog vs. numerical modeling

Nowadays, studies of subduction dynamics involve either laboratory or numerical simulations. While analog modeling provides a very high resolution and a physical realism, numerical modeling allows to fully control the physical parameters of the model. Besides the advantages and disadvantages of each method, several differences in the model setup may be taken into account. Analog models require a parameter scaling to compare results to natural case studies [*Ribe and Davaille*, 2013]. Boundary effects have to be considered and minimized by lubricating the lateral walls or by using large box sizes (> 20-30 cm from the plates to the wall) [e.g., *Funiciello et al.*, 2006; *Peral et al.*, 2018]. On the other hand, numerical modeling allows introducing geometries and physical parameters similar to those observed in nature. A range of specific boundary conditions may be applied to reproduce as well as possible the natural conditions. In contrast to analog experiments, where plates are usually modeled as purely viscous, subducting plates in numerical experiments commonly consist of three layers representing a first-order approximation of an oceanic lithosphere profile. In addition, the symmetry of most numerical models allows modeling only half-space of the system, increasing the model resolution and saving computation time [e.g., *Piromallo et al*., 2006; *Mason et al*., 2010; *Király et al*., 2016]. The choice of the modeling technique may depend on the observations to be reproduced. The use of both methods, despite being different, are complementary helping to better understand the behavior of a specific geodynamic process.

CHAPTER 4

Analog experiments of subduction systems with opposite polarity in adjacent segments

Chapter 4

Analog experiments of subduction systems with opposite polarity in adjacent segments

A series of analog models based on viscous syrup (representing the mantle) and silicone putty (representing the subducting plate) have been designed to simulate the evolution of subduction systems with opposite polarity in adjacent plate segments. The goals of this chapter are: 1) to understand the first order dynamics of the complex mantle flow generated in such subduction systems; 2) to analyze the interaction between the subducting plates in terms of their respective deformation and trench velocities; and 3) to test the influence of the width of plates and the initial separation between them on the evolution of the system.

The results presented in this chapter have been published in the scientific journal *Tectonics* (*Peral et al.,* 2018), being the first analog models of double polarity subduction in adjacent segments presented to the scientific community.

4.1 Model setup

The experimental setup adopted is widely used in analog modeling of subduction processes [e.g., *Griffiths et al*., 1995; *Guillou-Frottier et al*., 1995; *Faccenna et al*., 1996; *Becker et al*., 1999; *Funiciello et al.*, 2003; *Bellahsen et al*., 2005] (see Section 3.2). The following sections describe the assumptions made, the materials used, the scaling of

parameters in laboratory and nature, the different models performed and the measurements realized for the presented experiments.

4.1.1 Assumptions

The analog models presented here are based on the following assumptions:

1. The slab is modeled as a viscous body. The slab and mantle rheologies are simplified using a Newtonian fluid although experimental data suggest that in the natural prototype the upper mantle materials can also follow a non-linear rheology in regions of large stress [*Brace and Kohlstedt*, 1980].

2. The system is isothermal. This is equivalent to considering that the slabs are in a quasi-adiabatic condition, which is a good approximation as long as the subduction velocities are greater than 1 cm yr^{-1} [*Bunge et al.*, 1997; *Wortel*, 1982].

3. Slab pull is the only driving force acting on the experimental system. No external boundary conditions acting on the trenches are applied. The velocity of plates is forced to be zero at their trailing edges such that the retreating rate equals the amount of subduction ($v_s = v_t$, Figure 2.4) if internal deformation is negligible. This condition maximizes the effects associated with toroidal flow and is therefore an upper bound in quantifying its effects.

4. Despite the overriding plate may be of large influence on subduction evolution [*Yamato et al.*, 2009], it is not included into the setup in order to run simplified models with clear cause-effect relationships. Hence, the same low viscosity as the mantle is used for all the plate boundaries. This assumption implies that the overriding plates move passively with the retreating trenches.

5. The experimental setup uses a Plexiglas bottom to simulate the 660 km discontinuity. This implies that the upper/lower mantle boundary is considered as impermeable. This choice is justified by the fact that the lower mantle viscosity is at least one order of magnitude higher than the upper mantle, and the timescale of the process is of the order of a few tens of millions of years [e.g., *Davies*, 1995; *Guillou-Frottier et al.*, 1995; *Christensen*, 1996; *Funiciello et al.*, 2003].

6. There is no imposed mantle flow in the experimental setting in order to isolate the mantle advection produced by the slabs. Hence, the only momentum within the mantle is that caused by the plate/slab system.

7. The reference frame of these models is the box boundary, which can be considered as the experimental analog of the mantle reference frame.

4.1.2 Materials and scaling parameters

The double subduction system is approximated by two linear viscous layers representing the oceanic plates and the upper mantle. The oceanic plates are made up by silicone putty (pure silicone with ~42 wt% Fe fillings to obtain the required density), which is a viscoelastic material that at experimental strain rates acts as a Newtonian high viscosity fluid [*Weijermars*, 1986; *Grotenhuis et al.*, 2002]. The upper mantle is approximated by a syrup that behaves as a Newtonian low-viscosity and high-density fluid.

The models have been scaled respecting the standard scaling procedure commonly used in a natural gravity field ($\vec{g}_{\text{model}} = \vec{g}_{\text{nature}}$) [e.g., *Weijermars and Schmeling*, 1986]. A summary of the parameters used in the models and their corresponding values in nature is shown in Table 4.1. The scale factor for length is 1.6×10^{-7} (1 cm in the experiment corresponds to 60 km in nature). The scale density contrast between the oceanic plate and the upper mantle is ρ_l-$\rho_m \approx 60$ kg/m^3, whereas the average viscosity ratio is $\eta_l/\eta_m \approx 215$. These values are close to those estimated in nature which range from 40 to 80 kg m^{-3} for the density contrast and from 10^2 to 10^3 for the viscosity ratio [e.g., *Funiciello et al.*, 2008; *Stegman et al.*, 2010]. With these scale ratios, 1 min in the evolution of the model corresponds to 1 Myr in nature.

Table 4.1 Scaling of parameters in laboratory and in nature for the presented experiments.

Parameter	Symbol	Units	Laboratory	Nature
Gravitational acceleration	g	m/s^2	9.81	9.81
Upper mantle thickness	H	m	0.11	660000
Oceanic lithosphere thickness	h	m	0.0135-0.0145	81000-87000
Lateral distance between plates	d	m	0.005-0.1	30000-600000
Density contrast	$\Delta\rho=\rho_l-\rho_m$	kg/m^3	60	~75
Viscosity ratio	η_l/η_m	----	188-256	10^2-10^3
Characteristic Time: $\frac{t_{nat}}{t_{mod}} = ((\Delta\rho\, h)_{mod}\, \eta_{nat})/((\Delta\rho\, h)_{nat}\, \eta_{mod})$	t	s	60 (1 min)	1.3×10^{13} (1 My)

To simplify the comparison of results from different models, kinematic parameters are normalized to obtain dimensionless quantities. Trench velocities are normalized by the Stokes velocity v_s, which is specific for each setup:

$$v_{norm} = \frac{v}{v_S} = \frac{v}{(\rho_l - \rho_m)\cdot g \cdot H \cdot h/\eta_m}, \quad (4.1)$$

where v is the magnitude of the measured velocity, g is the gravity acceleration, ρ_l is the plate (silicone) density, ρ_m is the mantle (syrup) density, h is the oceanic lithosphere thickness, H is the mantle thickness and η_m its viscosity. As pointed out by *Capitanio et al.* [2007], the normalized velocity is also a measure of the slab geometry such that for the case presented here, in which subduction occurs purely due to trench retreat, v_{norm} = 1/tan (α) being α the dip angle of the slab. Therefore, higher v_{norm} results in smaller slab dip.

Time is normalized relative to the time taken by the slab to arrive at the lower mantle (t') according to a single plate reference model,

$$t_{norm} = \frac{t}{t'}, \tag{4.2}$$

that for the models presented here is t' = 20 minutes.

4.1.3 Experimental procedure and measurements

Experiments were designed to analyze the behavior of a double subduction system with opposite retreating directions in adjacent plate segments. Figure 4.1 shows the scheme of the experimental setup previously introduced in Section 3.3.3 (see also

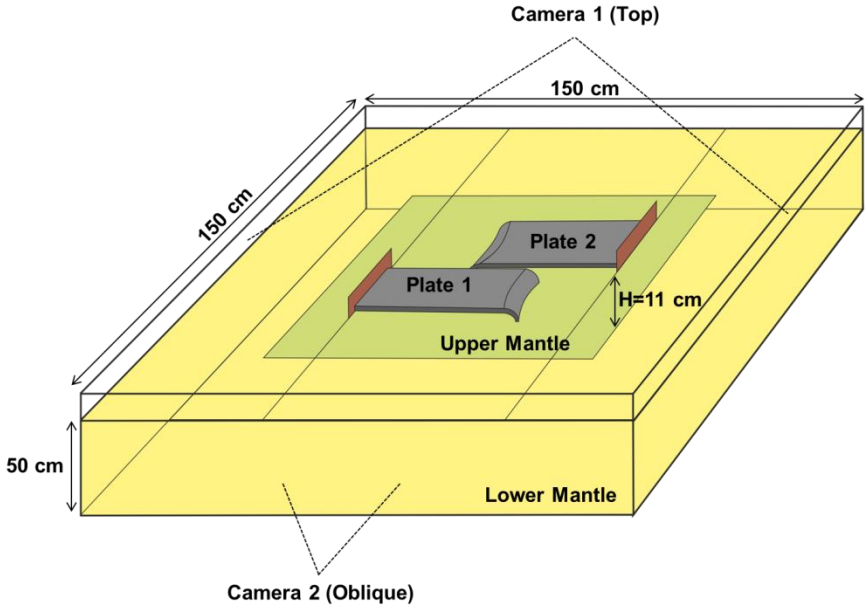

Figure 4.1 Scheme of the experimental setup. The tank is full of viscous syrup (in yellow) representing the mantle. The oceanic plates are made by silicone putty and subduct in opposite directions. Both plates are fixed at their trailing edge to enforce slab rollback. A fixed base (in green) is placed at 11 cm depth to simulate the upper-lower mantle transition. Two cameras are placed above the experiment (camera 1) and in an oblique position (camera 2) to observe the evolution of the system.

Figure 3.3). Plates are fixed at their trailing edge and subduction is started by deflecting simultaneously the leading edge of both plates inside the syrup up to a depth of 3 cm (≈200 km in nature) (Figure 3.5). Twelve analog experiments with two slabs, varying the width of the plates and the distance between them, have been run. Additionally, 6 single plate subduction models have been run as reference examples, two of them including a stationary side plate to investigate the role of the adjacent passive lithosphere. Table 4.2 summarizes the model experiments indicating the geometric characteristics and the relevant physical parameters.

The width of the plates varies from 10 cm to 30 cm (600 km to 1800 km in nature) and the initial distance between them varies from 0.5 cm to 10 cm (30 km to 600 km in

Table 4.2 Geometric characteristics and physical parameters of the laboratory experiments.

Double subduction models											
Exp	**d_0** (cm)	**Plate 1**		**Plate 2**		**ρ_l** (kg/m³)	**ρ_m** (kg/m³)	**η_l** (Pa·s)	**η_m** (Pa·s)	**γ**	**V_{Stokes}** (mm/min)
		w(cm)	**h**(cm)	**w**(cm)	**h**(cm)						
E1	2	10	1.30	10	1.30	1499	1445	40470	216	188	211
E2	1	10	1.40	10	1.40	1499	1445	40049	213	188	230
E3	0.5	10	1.30	10	1.30	1499	1445	40530	211	192	215
E4–Mod4	0.5	10	1.35	10	1.35	1499	1445	40470	213	190	219
E5	0.5	20	1.35	20	1.35	1499	1445	40771	202	202	234
E6–Mod3	0.5	20	1.40	20	1.40	1511	1445	38728	151	256	396
E7–Mod2	0.5	30	1.40	30	1.40	1499	1445	39929	195	205	251
E8	10	10	1.33	10	1.33	1511	1445	39509	176	224	322
E9	10	20	1.40	20	1.40	1511	1445	39809	174	229	344
E10–Mod1	10	30	1.45	30	1.45	1511	1445	39929	179	223	347
E11–Mod5	0.5	30	1.40	10	1.35	1511	1445	38968	172	227	341
E12	10	30	1.40	10	1.40	1511	1445	39689	167	237	358
Single subduction with lateral fixed plate											
E13-P2 fixed	0.5	20	1.40	20	1.35	1511	1445	39268	167	235	350
E14-P2 fixed	0.5	20	1.40	20	1.40	1511	1445	38908	163	239	368

Single Subduction (Reference models)								
Exp	**w** (cm)	**h** (cm)	**ρ_l** (kg/m³)	**ρ_m** (kg/m³)	**η_l** (Pa·s)	**η_m** (Pa·s)	**γ**	**V_{Stokes}** (mm/min)
E15	10	1.35	1499	1445	40530	209	194	226
E16	20	1.35	1499	1445	40170	204	197	231
E17	20	1.35	1511	1445	38968	167	233	345
E18	30	1.35	1511	1445	40290	206	195	280

d_0: lateral distance between plates; w: plate width; h: plate thickness; ρ_l: plate density; ρ_m: mantle density; η_l: plate viscosity; η_m: mantle viscosity; $\gamma = \eta_l/\eta_m$; V_{Stokes}: Stokes velocity. Mod: model.

nature). A grid of 1 x 1 cm^2 is drawn on the upper surface of each plate to quantify the deformation during the evolution of the model (Figures 3.3c and 3.4).

Models are monitored with two cameras taking photographs every 30 seconds in top view and from an oblique position with respect to the model. Post-processing image tools are used to analyze the trench retreat velocities, the trench curvatures and the lateral distance between plates during the experiment. Moreover, the toroidal mantle flow is observed on the top-view photos through the microbubbles created in the syrup to track the fluid movement and quantified using the Particle Image Velocimetry technique [i.e., PIVlab software; *Thielicke and Stamhuis*, 2014].

The trench retreat velocities of each plate are calculated by tracking the location of the two edges and the center of the trench. The retreating rate is calculated as a weighted average of these points to reduce the effect that the increase in trench curvature can cause on the apparent trench retreating rate. In order to quantify the trench curvature the trench geometry is represented as a circular segment. The curvature *c* is then defined as,

$$c = \frac{r_2}{r_1}, \tag{4.2}$$

where r_1 is the chord and r_2 the sagitta of the section (Figure 4.2). The curvature is therefore zero for a straight trench and it increases for curved trenches.

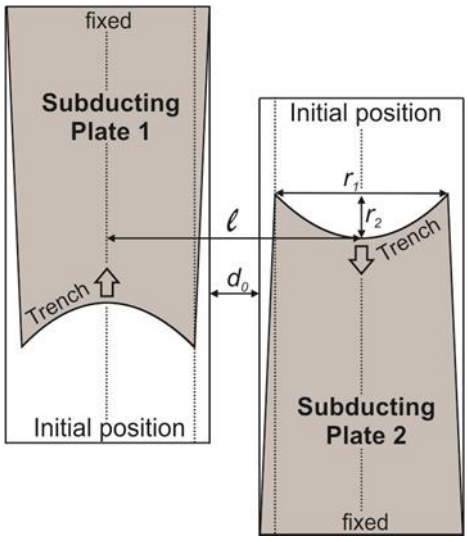

Figure 4.2 Simplified sketch of the model setup (top view). Plates are fixed at their trailing edge. The initial separation between plates (d_0) is the distance between the lateral edges before subduction starts. The lateral distance between plates (ℓ) is defined as the perpendicular distance between the centers of the trenches. The trench curvature (c) is defined as r_2/r_1.

The lateral displacement of the plates is measured by quantifying the variations of the distance ℓ between the centers of the trenches (Figure 4.2).

It is worth noting that, as in any experimental approach, internal inhomogeneities of the materials and laboratory procedures could introduce spurious uncertainties in the results. The noise observed in the data is mainly a consequence of the inevitable unevenness and non-uniformity in making up the experimental setup. Despite these limitations, the experimental results presented in the following section are robust enough to shed light on the dominant processes involved in the models.

4.2 Results

To understand the results presented here, it is important to recall that the basic kinematics of single plate subduction processes results from the balance of the acting forces that, in the absence of the upper plate, includes the gravitational slab pull, viscous shear with the ambient mantle, and viscous resistance energy term to downward plate bending (Figure 2.4). Alike numerous analog and numerical experiments with fixed trailing edge ($v_s = v_t$; [e.g., *Funiciello et al.*, 2003; *Schellart*, 2004a]), the single plate subduction models E15 to E18 (Table 4.2) show a characteristic evolution of the subducting lithosphere during its descend into the upper mantle and its interaction with the 660 km discontinuity as described in Section 2.1. The results presented here are focused on phases 2 and 3 of double subduction systems as defined in Section 2.3, in which steady state subduction has been reached. Variations of the trench retreat velocities and the trench curvature as a function of time are calculated.

To illustrate the most outstanding results five double subduction models have been selected showing the whole range of the analyzed variables. Indeed, models 1 and 2 show the role of the initial separation between plates, model 3 shows how the mantle flow is modified in such subduction system and models 4 and 5 show the effects of the plate width (Table 4.2).

4.2.1 Model 1 – Wide and distant plates

Model 1, composed of two plates of 30 cm width and spaced 10 cm, is designed to study the behavior of the system when the interaction between plates is very weak. In this model, plates are slightly thicker (1.45 cm, Table 4.2) than in the rest of the models and

the viscosity contrast between the plates and the mantle is $\frac{\eta_l}{\eta_m} = 223$ (Table 4.2). Figure 4.3 shows the normalized trench retreat velocity v_{norm} and the trench curvature c of both plates as a function of the normalized time t_{norm}. Normalized velocities keep almost constant during phases 2 and 3 showing similar values for both plates ($0.47 \pm 0.04 \cdot 10^{-2}$). The trench curvatures of both plates increase linearly with time showing nearly symmetric shapes and values. Comparing this model with its corresponding reference model (single subduction system of a 30 cm width plate, model E18 in Table 4.2), a very similar behavior is obtained in terms of retreating velocity and trench symmetry. Finally, the distance ℓ (Figure 4.2) between the centers of the trenches remains roughly constant during the whole experiment indicating that there is no net separation between plates.

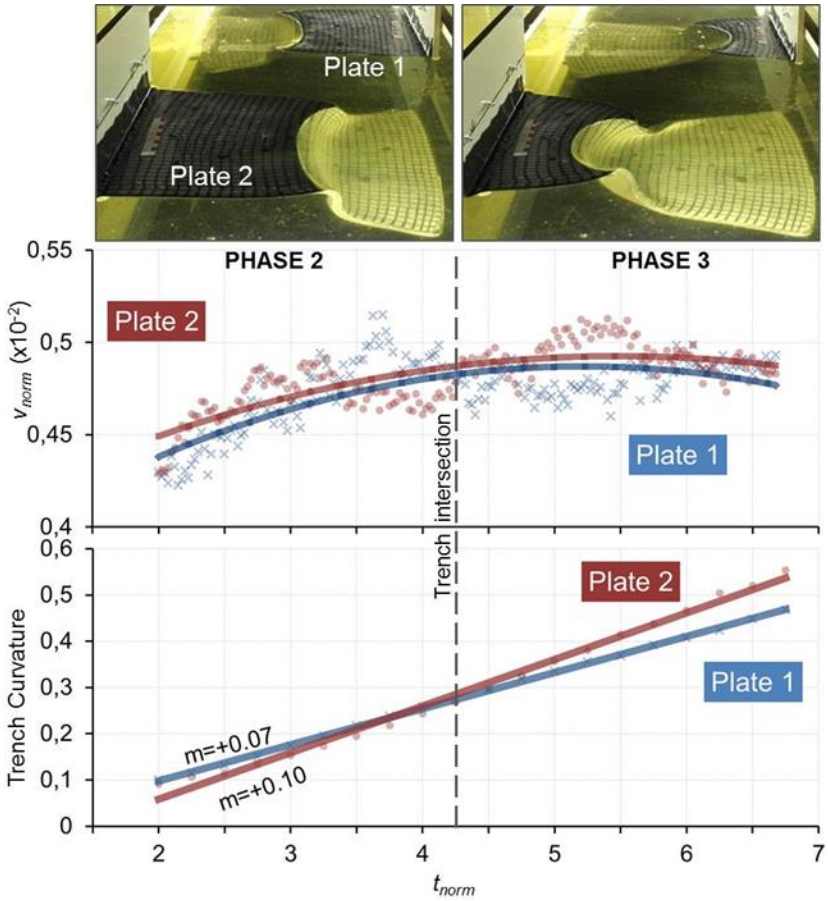

Figure 4.3 Evolution of double polarity subduction Model 1 during phase 2 (approaching trenches) and phase 3 (diverging trenches). Both plates are 30 cm wide with an initial separation between them of d_0= 10 cm. Upper and lower graphics show the normalized retreating velocity and curvature of the trenches vs normalized time (see text). Crosses and dots indicate measurements and thick lines correspond to a second order polynomial regression (upper graphic) and linear regression (lower graphic).

4.2.2 Model 2 – Wide and near plates

Model 2 is composed of two 30 cm wide plates with an initial separation of d_0 = 0.5 cm. This model is used, alongside with Model 1, to study the influence of the initial separation between plates on the dynamics of the mantle flow and plates interaction. Figure 4.4 shows the normalized trench retreat velocity and trench curvature of both plates as a function of the normalized time.

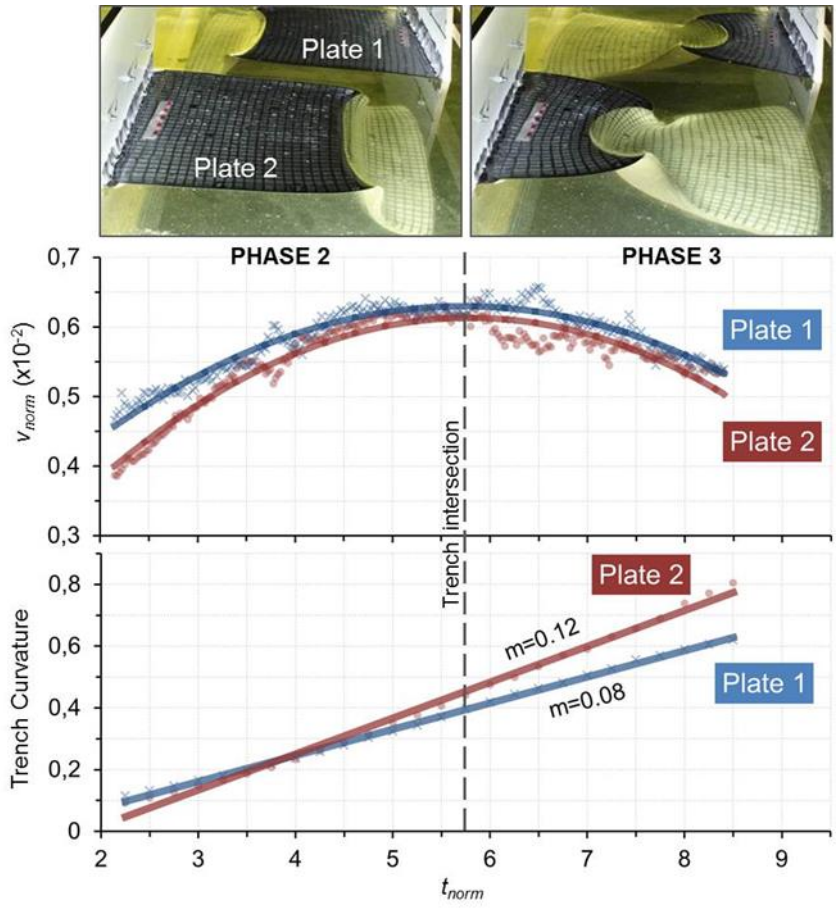

Figure 4.4 Evolution of double polarity subduction Model 2 during phase 2 (approaching trenches) and phase 3 (diverging trenches). Both plates are 30 cm wide with an initial separation between them of d_0 = 0.5 cm. Upper and lower graphics show the normalized retreating velocity and curvature of the trenches vs normalized time (see text). Crosses and dots indicate measurements and thick lines correspond to a second order polynomial regression (upper graphic) and linear regression (lower graphic).

The most outstanding effect of reducing the initial separation between plates is the acceleration/deceleration of the retreat velocities and the variation with time of the distance between plates. Velocities tend to increase during the trench-approaching phase

2 varying from around $0.42 \cdot 10^{-2}$ to $0.62 \cdot 10^{-2}$, and decreasing to $0.52 \cdot 10^{-2}$ during phase 3 while trenches diverge. Since $v_{norm} = 1/\tan(\alpha)$, it is expected that during phase 2 the dip angle decreases as the normalized trench velocity increases, whereas in phase 3 the dip angle increases as trench velocity decreases. Unfortunately, the experiments do not allow measuring the evolution of the dip angle with enough accuracy and this aspect cannot be confirmed. Alike Model 1, the curvature of the trenches increases linearly with time. Both, normalized trench velocities and curvatures reach slightly higher values than in Model 1.

The lateral distance between plates ℓ increases during phase 2 resulting in a maximum increment of Δl = 0.4 cm or 1.3% relative to the initial position. During phase 3, l decreases progressively as the trenches approach the trailing edge of the respective plates, which are subjected to fixed boundary conditions.

4.2.3 Model 3 – Induced toroidal mantle circulation

Model 3 is chosen to show how the toroidal component of the mantle flow and the plate deformation patterns are modified in a double subduction system. The model consists of two 20 cm wide plates with an initial separation of 0.5 cm. The top camera allows tracking the syrup flow through the movement of exposed microbubbles in a horizontal section at ~1 cm depth as well as the deformation of the subducting plates observing the distortion of the grid drawn on their surfaces. The patterns obtained in this model can be extrapolated to the rest of the tested configurations. Figure 4.5 shows the inferred horizontal displacements occurring in the syrup (red arrows) and the plates (white arrows) before, during and after trenches pass each other.

During phase 2 (Figure 4.5a), the mantle flow delineates toroidal convective cells around the outer edges of the trenches of both plates whereas in the inner edges, the convective cells are less vigorous. Linked to these toroidal cells, there is an outward flow perpendicular to the outer sides of the plates, which tends to vanish in the region between both plates because the cells have opposite polarity, particularly when the trenches align with each other. The divergent displacement of both plates, indicated by the white arrows, is the combination of the stress perpendicular to the trench generated by the slab pull, and the drag produced by the outward flow of the syrup.

In the transition from phase 2 to phase 3 (Figure 4.5b), the toroidal flow around the outer edges of the trenches persist. The perpendicular distance ℓ between the centers of the trenches (see Figure 4.2) becomes higher and the region between the plates is

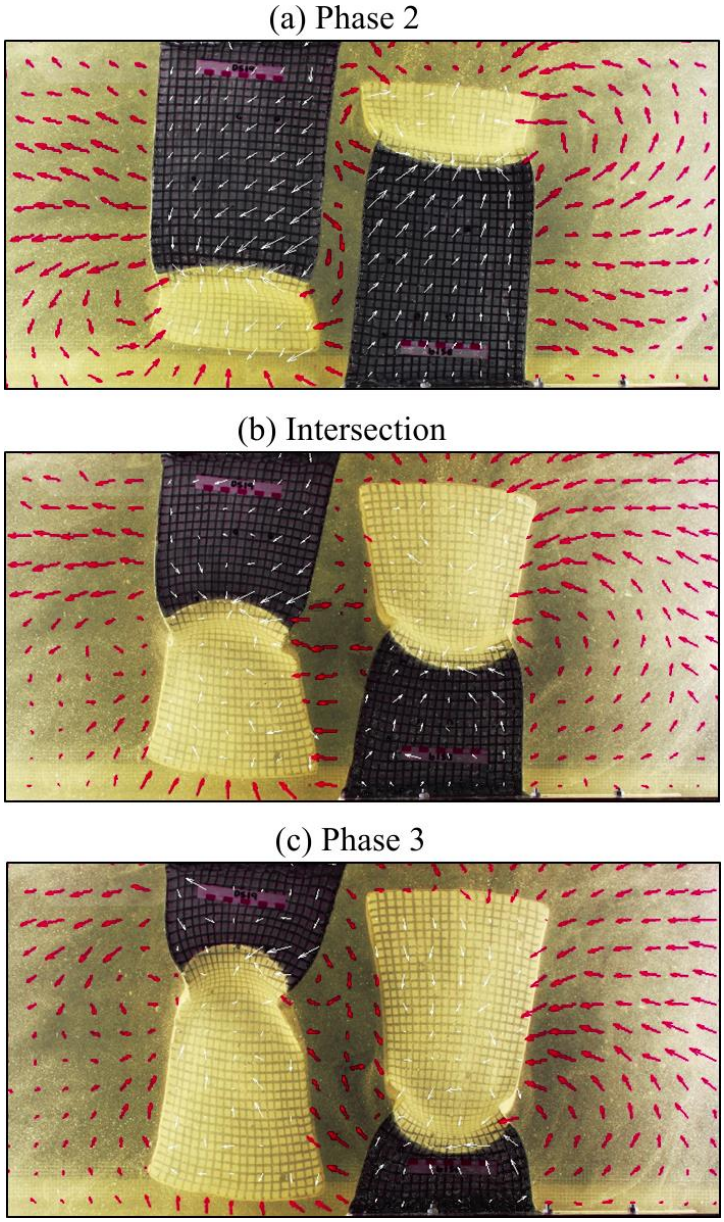

Figure 4.5 Syrup (mantle) flow (red arrows) and plate deformation (white arrows) corresponding to Model 3 (Table 2) during approaching trenches (a) phase 2, trenches intersection (b), and diverging trenches (c) phase 3.

occupied by a single convective cell in which the outward flow of the syrup from the central parts of one plate is directed to the trench of the opposite plate and vice-versa. The displacement of the plates depicted by the white arrows is quite random being well defined only near the trenches.

During phase 3 (Figure 4.5c), the toroidal flow around the outer edges of the trenches appears well defined and, as most of the plate is already subducted and the trench approaches the fixed trailing edge, the lateral outward drag is less vigorous. The flow in

the inter-plate region is weakened and actually vanished in its center because of the opposite directions of the generated toroidal cells around the inner edges of the trenches.

4.2.4 Model 4 – Narrow and near plates

Model 4 is composed of two 10 cm wide plates with an initial separation distance of d_0 = 0.5 cm and is designed to analyze the effects of the plate width on the dynamics of the system. The behavior of the system (Figure 4.6) is very similar to that for wide and near plates (Model 2) with similar normalized velocities and slightly lower acceleration/deceleration, indicating that the retreating velocity is not very sensitive to the width of plates. In contrast, the curvature of the trenches is almost three times lower for the narrow plates.

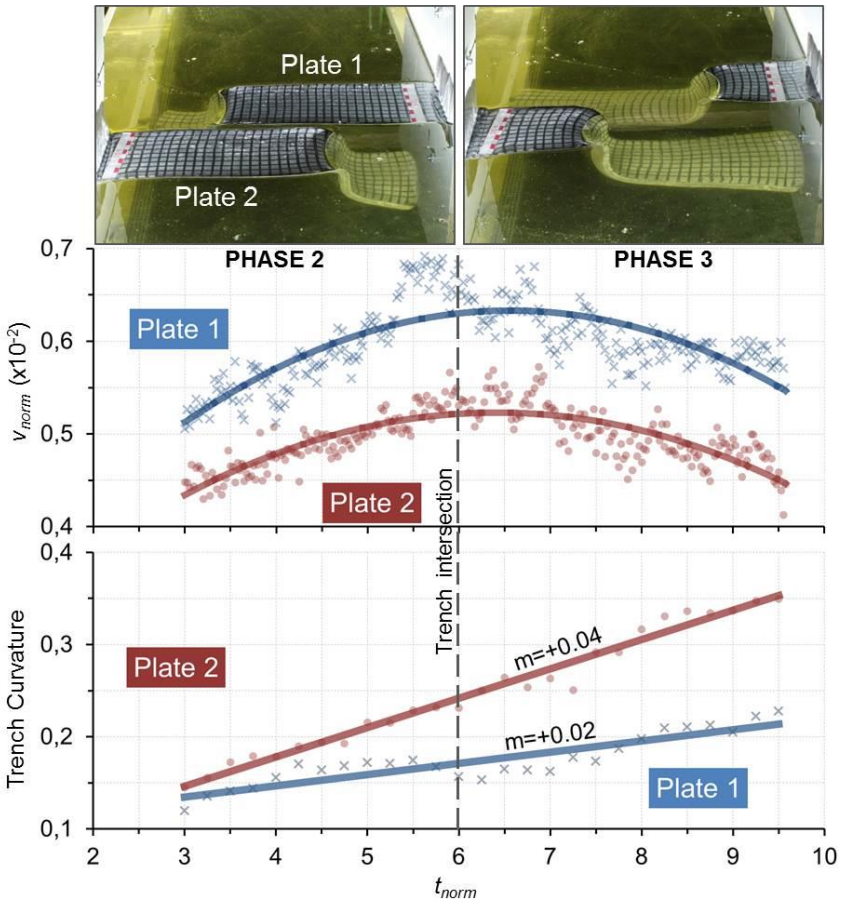

Figure 4.6 Evolution of double polarity subduction Model 4 during phase 2 (approaching trenches) and phase 3 (diverging trenches). Both plates are 10 cm wide with an initial separation between them of d_0= 0.5 cm. Upper and lower graphics show the normalized retreating velocity and curvature of the trenches vs normalized time (see text). Crosses and dots indicate measurements and thick lines correspond to a second order polynomial regression (upper graphic) and linear regression (lower graphic).

The normalized retreating velocity during phase 2 increases from around $0.50 \cdot 10^{-2}$ to $0.67 \cdot 10^{-2}$ for plate 1, and from around $0.43 \cdot 10^{-2}$ to $0.55 \cdot 10^{-2}$ for plate 2. During phase 3 the normalized retreating velocity of plate 1 decreases to $0.55 \cdot 10^{-2}$, whereas for plate 2 the retreating velocity decreases to $0.45 \cdot 10^{-2}$. Trench curvature of both plates increases linearly during all the retreating process disregarding the relative position of the trenches. However, results show a larger curvature for plate 2. The correlation between trench retreating velocities and trench curvature of both plates suggests that the higher the velocity is the smaller the curvature is (Figure 4.6). The noticeable distinct behavior between the two plates may be due to small differences in plate thickness (± 0.5 mm), since these are within the possible variability of the experimental setup and suffice to produce the observed velocity variations.

The lateral distance between plates increases during phase 2 ($\Delta\ell$ = 0.5 cm), resulting in a maximum increment of ~5% from its initial value. During phase 3, ℓ decreases, because of the fixed position of the trailing edge of plates.

4.2.5 Model 5 – Wide/Narrow near plates

Model 5 is designed to study the interaction of two near subducting plates (d_0 = 0.5 cm) with different widths. In this case plate 1 and plate 2 are 30 and 10 cm wide, respectively. Figure 4.7 shows that the normalized trench retreating velocity for the wider plate 1 increases during phase 2 from $0.46 \cdot 10^{-2}$ to $0.55 \cdot 10^{-2}$ keeping this value almost constant during phase 3. In contrast, the narrower plate 2 shows a smooth variation of the normalized velocity around an average value of $0.43 \cdot 10^{-2}$ during both phases. A weak relative maxima velocity of $0.46 \cdot 10^{-2}$ during phase 3 at t_{norm}= 4.5 can be identified in Figure 4.7.

The trench curvature of both plates increases linearly with time, showing maximum curvatures of 0.56 for plate 1 and 0.28 for plate 2. While plate 1 shows a nearly symmetric shape, the narrower plate 2 is affected by the near plate 1 slab, and undergoes an asymmetric deformation. The distance between plates ℓ increases ($\Delta\ell$ = 0.8 cm, i.e. 3.9% from the initial position) during phase 2 and decreases during phase 3 forced by the fixed position at their trailing edges. This lateral displacement is essentially undergone by the narrower plate 2.

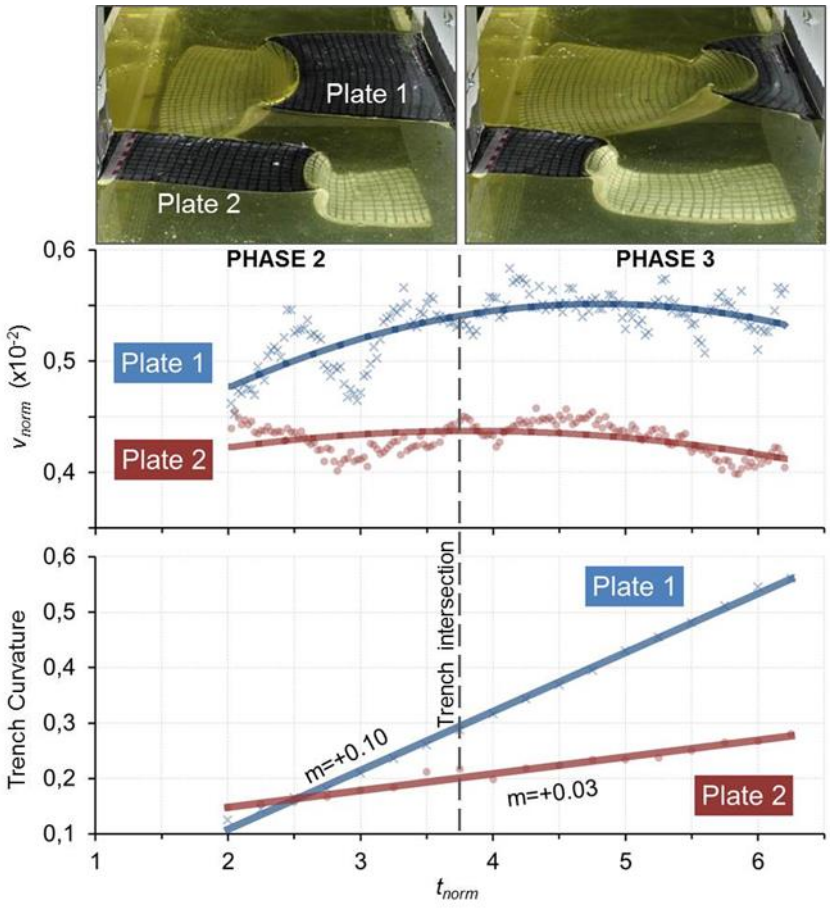

Figure 4.7 Evolution of double polarity subduction Model 5 during phase 2 (approaching trenches) and phase 3 (diverging trenches). Plate 1 and Plate 2 are 30 cm and 10 cm wide, respectively, with an initial separation between them of d_0= 0.5 cm. Upper and lower graphics show the normalized retreating velocity and curvature of the trenches vs normalized time (see text). Crosses and dots indicate measurements and thick lines correspond to a second order polynomial regression (upper graphic) and linear regression (lower graphic).

CHAPTER 5

Reproducing analog experiments of subduction systems with numerical modeling

Chapter 5

Reproducing analog experiments of subduction systems with numerical modeling

Combining computational and laboratory models of a given geodynamic experiment helps understanding its dynamics by complementing each method's weaknesses and strengths [*Panien et al*., 2006; *Mériaux et al*., 2018]. While laboratory experiments provide the physical realism and high temporal and geometrical resolution, numerical models allow for fully controlling and quantifying physical parameters, as velocity and stress, which cannot be directly obtained from laboratory experiments.

Here, numerical models aiming to reproduce analog experiments of complex double subduction systems developed in Chapter 4 are performed [*Peral et al.*, 2018]. In this regard, the geometrical setup and material parameters have been chosen to best represent values applied in the laboratory. The objectives of this chapter are twofold: First, to determine under which conditions the numerical models best reproduce complex analog experiments of subduction. And second, to better understand the dynamics of double subduction systems with opposite polarity in adjacent plate segments by combining analog and numerical approaches. In the first part of this chapter, I test the effects of boundary conditions, rheology and plate thickness on the evolution of single and double plate subduction systems. In the second part, I define a reference subduction system with opposite polarity to analyze plate deformation and mantle flow interaction by quantifying velocities, stresses and forces within the system, thus complementing previous experimental results. This reference frame is subsequently applied to the Westernmost Mediterranean region (Chapter 6).

The results presented in this chapter are submitted and under review to the Geochemistry, Geophysics, Geosystems journal of the American Geophysical Union.

5.1 Model setup

Geometrical and physical parameters of numerical models will be chosen to reproduce previous analog experiments [see Chapter 4; *Peral et al.,* 2018]. The numerical counterparts of single plate and double polarity subduction models have been performed by the three-dimensional code *I3ELVIS* (see Section 3.4.2). The following sections describe the setup of the different models performed here.

5.1.1 Assumptions

The numerical models presented here have been carried out under the following assumptions:

1. The geometry and dimensions of the model, as well as the rheological properties of silicon putty (plates) and glucose syrup (upper mantle) are the same as in the analog model described in Chapter 4.

2. The decoupling of the slab from the surface is handled by adding a layer of sticky-air.

3. The bottom of the model box, at 11 cm depth, is modeled as a rigid boundary assuming to be impenetrable as in the laboratory experiment [see Chapter 4; *Peral et al.,* 2018].

For more details about these assumptions see Section 3.4.3.

5.1.2 Numerical models

From previous analog experiments, only those with narrow and near plates for the double plate subduction system, and wide plates for the single plate system, have been selected as they show the most outstanding results in terms of plate interaction and trench deformation [see Chapter 4; *Peral et al.,* 2018].

To assess boundary effects acting on the subduction system, three Eulerian box sizes have been considered. Large, intermediate and small boxes measure 150 x 150 cm^2 (model N1), 80 x 80 cm^2 (model N2) and 30 x 40 cm^2 (model N3) in horizontal directions,

respectively. The largest box model corresponds to the real dimensions of the tank used in the laboratory experiment (Figure 3.3). Due to the relatively large cell size in model N1, plates are initially spaced 2 cm while in the rest of the models the initial lateral distance is of 1 cm, corresponding to the separation that is observed in the laboratory experiments immediately after subduction initiation. All models have a height of 12 cm. The initial distribution of markers is characterized - from bottom to top - by 11 cm of mantle and 1 cm of "sticky-air". The density of the mantle material is 1445 kg/m^3, the plates have a density of 1505 kg/m^3 and the "sticky-air" layer has a density of 1 kg/m^3 (Table 5.1). All models but one have a linear viscous rheology for both plates and mantle, with values listed in Table 5.1. Plates have an initial thickness of 1 cm, 1.2 cm or 1.35 cm and are located at the top of the mantle, in contact with the "sticky-air" layer (Figure 5.1). Plate dimensions are 30 cm long and 10 cm wide for double-plate and 10 cm or 30 cm wide for

Table 5.1 Geometric characteristics and physical parameters of single and double subduction models.

NUMERICAL MODELS										
Mantle							**Plates**			
ρ_m (kg/m^3) **1445**							ρ_l (kg/m^3) 1505			
Double subduction models										
Model	**d** cm	**l** cm	**w** cm	**h** cm	**Newtonian rheology**		**Box domain** cm	**Resolution** cm	**Box BCs**	
					η_l Pa·s	**η_m** Pa·s			**L**	**B**
N1	2	30	10	1.35	40470	213	150x12x150	0.5x0.1x0.5	FS	NS
N2	1	30	10	1.35	40470	213	80x12x80	0.3x0.1x0.3	FS	NS
N3	1	30	10	1.35	40470	213	40x12x30	0.2x0.1x0.2	FS	NS
N4	1	30	10	1.35	40470	213	150x12x150	0.5x0.1x0.5	NS	NS
N5	1	30	10	1.35	40470	213	80x12x80	0.3x0.1x0.3	NS	NS
N6	2	30	10	1.35	40470	213	40x12x30	0.2x0.1x0.2	NS	NS
N7	1	30	10	1.35	40470	213	80x12x80	0.3x0.1x0.3	FS	FS
Single subduction models										
Model	**l** cm	**w** cm	**h** cm	**Newtonian rheology**			**Box domain** cm	**Resolution** cm	**Box BCs**	
				η_l Pa·s		**η_m** Pa·s			**L**	**B**
N8	30	10	1.35	40470		213	80x12x80	0.3x0.1x0.3	FS	NS
N9	30	30	1.35	38728		151	80x12x80	0.3x0.1x0.3	FS	NS
N10	30	30	1.35	40290		206	80x12x80	0.3x0.1x0.3	FS	NS
N11	30	30	1.00	40290		206	80x12x80	0.3x0.1x0.3	FS	NS
N12	30	30	1.35	38900		389	80x12x80	0.3x0.1x0.3	FS	NS
N13	30	30	1.20	38900		389	80x12x80	0.3x0.1x0.3	FS	NS
N14	30	30	1.00	38900		389	80x12x80	0.3x0.1x0.3	FS	NS
Model	**l** cm	**w** cm	**h** cm	**Power-law rheology**			**Box domain** cm	**Resolution** cm	**Box BCs**	
				η_0 Pa·s	**n**	**η_m** Pa·s			**L**	**B**
N15	30	30	1.35	1000	1.5	206	80x12x80	0.3x0.1x0.3	FS	NS

ρ_m: mantle density; ρ_l: plate density; d: lateral distance between plates; l: plate length; w: plate width; h: plate thickness; η_l: plate viscosity; η_m: mantle viscosity; BCs: Boundary conditions; L: lateral; B: Bottom; FS: Free-slip; NS: No-slip.

single plate models (Table 5.1). Plates are fixed at their trailing edges by predefined null nodal velocity in all directions at a distance *s* of 39 cm to each other parallel to the plate extent (Figure 5.1A). To initiate density-driven subduction, a small slab perturbation is initially imposed at their leading edges where the slab penetrates 3 cm into the mantle. One additional model has been conducted with a non-linear, strain-rate dependent viscosity for the subducting plate (model N15; equation 3.13).

Subduction of the plate(s) in the numerical models is dynamically self-consistent in the sense that it is driven by density contrast only and no material flux is allowed into and out of the model domain. All models exhibit a no-slip condition at the top boundary. Lateral and bottom boundary conditions are variably prescribed as no-slip or free-slip to test their effect on mantle flow and subduction retreat (Table 5.1).

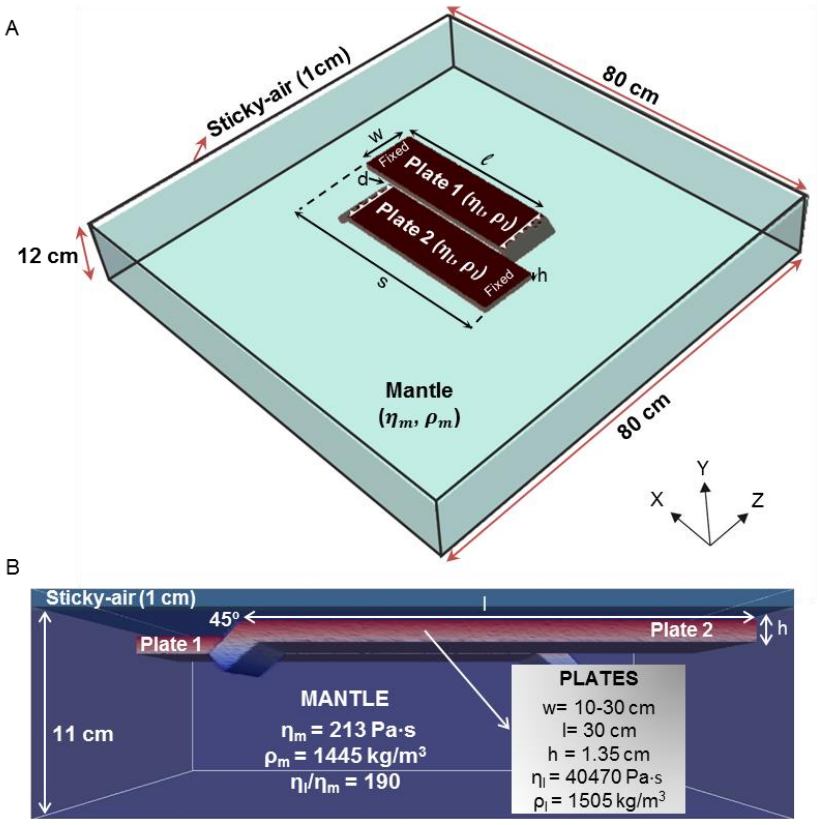

Figure 5.1 Scheme of the 3D numerical model of double subduction with opposite polarity in adjacent segments with similar material parameters and geometry as in laboratory experiments. Plates are fixed at their trailing edges to enforce rollback. Subduction is initiated by a small slab reaching 3 cm depth. Different configurations varying the size of the box and boundary conditions have been tested. Dimensions shown in (A) correspond to models N2, N5 and N7 (Table 5.1). A) Oblique view. B) Lateral view.

5.2 Comparing analog-numerical experiments

Preliminary numerical models have been run reproducing the laboratory conditions to better understand how the numerical/analog modeling constraints affect the final results in the natural prototype rather than to the laboratory experiments itself. A 3-step parametric study has been performed. First, numerical models of double subduction systems with 10 cm wide plates have been designed to test the effects of variable model domain size. Second, the importance of applied numerical boundary conditions is investigated. Finally, numerical models with a single 30 cm wide plate have been conducted to reveal the effects of plate stiffness by varying plate viscosity and thickness. Geometric and physical parameters of all presented models are listed in Table 5.1.

Same as in Chapter 4, results are described taking into account the three different phases of evolution of a subduction system with opposite polarity in adjacent segments described in Section 2.3, considering that the intersection of the trenches is defined as the transition from phase 2 to phase 3.

5.2.1 Influence of domain size

The size of the domain in the models might have some influence in the results if the walls are not far enough from the subduction system. If the lateral walls are too close, the mantle cells will be influenced and the dynamics of the system might be affected. I tested the same subduction system using three different domain sizes and numerical models with different box sizes produce similar plate geometries during all the phases of subduction (Figure 5.2). Phase 1 is not shown in this section as the trenches are too far from each other to produce any interaction between plates. Phase 2 shows that plates tend to approach each other, this effect being more intense for the medium and small box experiments. In phase 3, subduction continues and the slabs show a flattened asymmetric shape lying on the bottom of the model due to the lateral bending in the x-z plane acting on the contiguous lateral sides of the plates. This asymmetric deformation is less intense in model N1, where plates are initially more separated. The flow pattern at 6 cm depth from the top of the model domain is similar in all models (Figure 5.2), though the radius of the toroidal flow is smaller as the box size decreases. The maximum mantle velocities (1.4 mm/min) at this depth are registered in front of the trench and behind the slab during the entire subduction process.

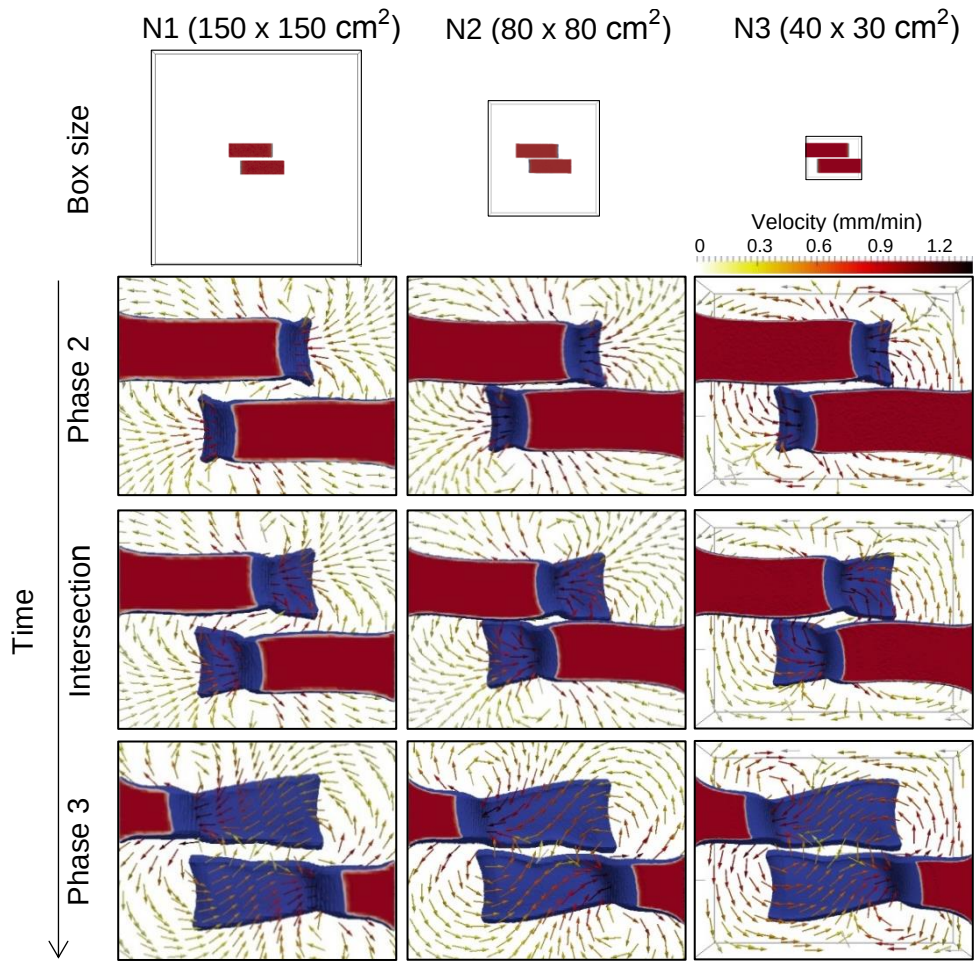

Figure 5.2 Temporal evolution of numerical double subduction models with 10 cm wide plates and different box sizes (models N1, N2 and N3). Upper row displays the model box size for each column. Intersection stage corresponds to the transition between Phase 2 and Phase 3. Color arrows indicate the velocity field in the x-z plane (top view) at 6 cm depth from the top of the model domain. Blue and red colors denote the subducted and the buoyant parts of the plate, respectively. Note that models N1 and N2 do not show the mantle flow over the whole box.

Figure 5.3 shows the amount of trench retreat versus time for models with different box sizes. Trench retreat is calculated at the center of the trench by locating its position at each timestep. Trenches retreat in an irregular way in all cases showing a slight acceleration during phase 3 that is more evident in model N2 (80 x 80 cm^2) (Figure 5.3).

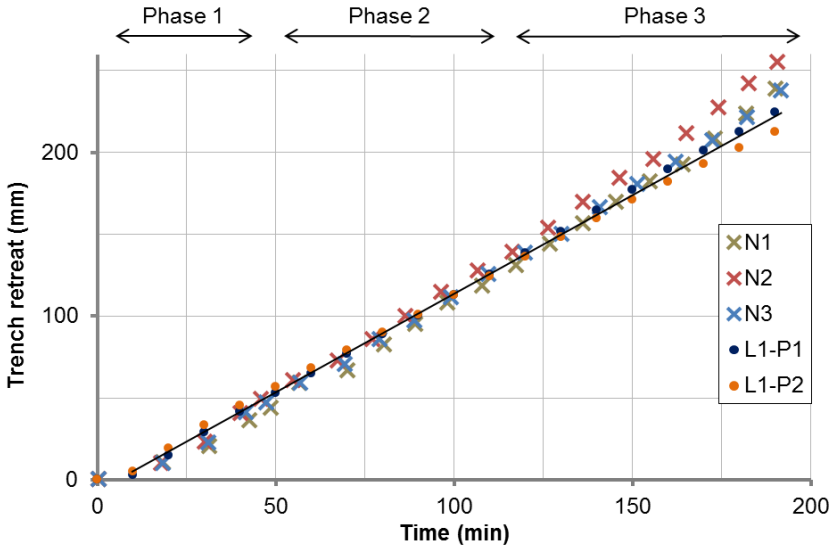

Figure 5.3 Trench retreat vs time corresponding to numerical models N1 (150 x 150 cm²), N2 (80 x 80 cm²), N3 (30 x 40 cm²) and laboratory experiment L1 (150 x 150 cm²). For the analog experiment the trench retreat of both plates (P1 and P2), as well as the corresponding linear regression line, is shown as they may differ influenced by the model setup.

5.2.2 Influence of lateral boundary conditions

Figure 5.4 illustrates the temporal evolution of trench retreat of models with free-slip (N1, N2 and N3) and no-slip (N4, N5 and N6) conditions in the lateral boundaries. Applying free-slip conditions allows mantle material to move along the lateral walls of the box with no resistance. Contrary, no-slip lateral boundary conditions prevent lateral flow

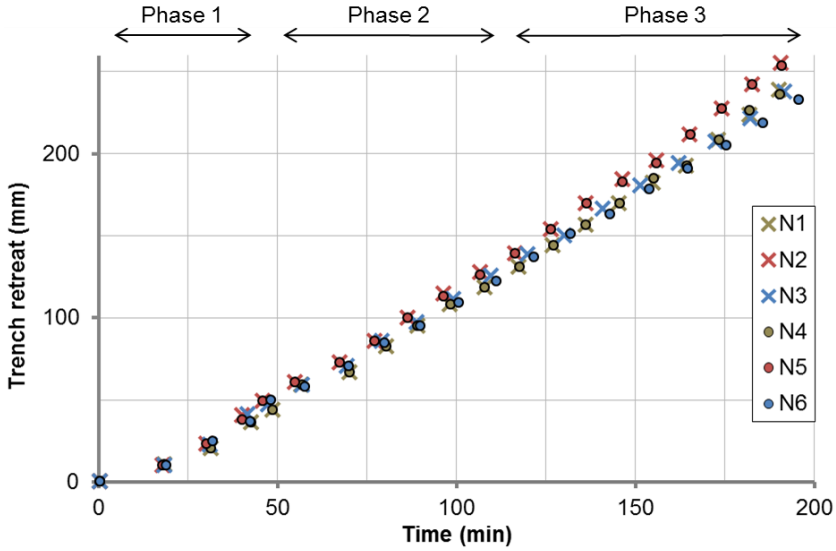

Figure 5.4 Trench retreat vs time corresponding to numerical models N1/N4 (150 x 150 cm²), N2/N5 (80 x 80 cm²) and N3/N6 (30 x 40 cm²) applying different boundary conditions at the lateral walls of the box (x: free-slip; o: no-slip).

on the surface of the walls. Under these conditions and depending on the model size domain velocities within the mantle may be reduced causing slower retreating of the plates.

Results show no noticeable differences in the resulting trench retreat related to these two end-member boundary conditions for models with box size of 150 x 150 cm^2 and 80 x 80 cm^2. However, models N3 and N6 (box size 40 x 30 cm^2) show a measurable offset with free-slip boundaries resulting in a slightly faster trench retreat (Figure 5.4).

5.2.3 Influence of bottom boundary conditions

Laboratory experiments show that subducted plates, although slightly, deform and slip over the bottom side of the box and therefore, the no-slip bottom boundary condition is not strictly fulfilled [*Peral et al.,* 2018; see also Figure 5.12]. Here I explore the effects of considering free-slip or no-slip boundary conditions at the bottom of the model domain, and show that they strongly modify the shape of the two slabs when reaching the base of the model (Figure 5.5).

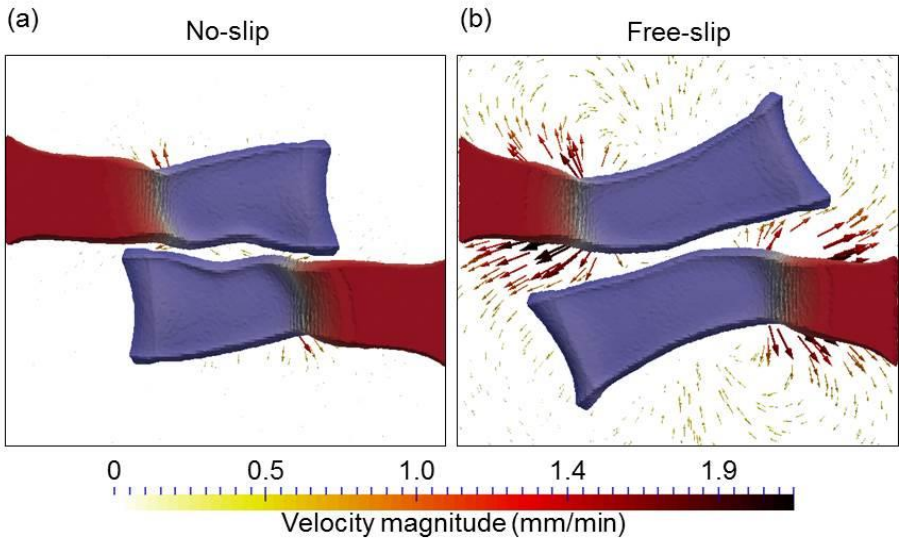

Figure 5.5 Numerical model of double subduction with opposite polarity of 10 cm wide plates during phase 3 (t=148 min) with no-slip (a) (model N2) and free-slip (b) (model N7) boundary conditions at the bottom of the box. Color arrows show the mantle flow close to the base of the model domain.

A double subduction model with no-slip boundary condition at the bottom implies zero horizontal velocity for the mantle and the slab material when it reaches the base of the model domain. Therefore, lateral movement and stretching of the plate lying on the

floor of the model is restricted (Figure 5.5a). On the other hand, free-slip boundary conditions at the bottom allow the slabs to stretch in horizontal directions and slabs can move laterally along the bottom boundary depending on the resulting velocities (Figure 5.5b). The resulting trench retreat velocities are 15% higher for free-slip than for no-slip conditions and the toroidal mantle flow at this depth produces a lateral movement of both slabs that is not observed for the no-slip models.

5.2.4 Influence of plate rheology and plate thickness

Laboratory experiments of single and double subduction [Chapter 4; *Peral et al.,* 2018] have shown that the trenches of subducting plates exhibit a more intense curvature than numerical models when applying identical spatial and rheological parameters (Figures 5.6a, 5.6b). This effect, which is more pronounced for wider plates [*Peral et al.,* 2018], arises the question whether the rheology of the plates and the mantle differ for laboratory and numerical models. Therefore, a series of numerical models with a 30 cm wide single plate has been conducted to test the effects of plate rheology and thickness on the subduction process and particularly on the trench curvature (see Table 5.1 and Figure 5.6).

Results show that the trench curvature, defined as the ratio between the chord and the sagitta of the circular segment delineated by the trench (see Section 4.1.3), decreases and the deformation and stretching of the slab increases with a decreasing viscosity ratio between the lithosphere and the mantle ($\gamma=\eta_l/\eta_m$). Reducing the viscosity ratio to $\gamma = 100$ is not sufficient to reproduce the slab deformation observed in the laboratory experiment (Figure 5.6c). Furthermore, the trench curvature slightly decreases (Figure 5.6c). However, reducing simultaneously the viscosity ratio to $\gamma = 100$ and the plate thickness to 1.2 cm maintains the trench curvature showing a more pronounced slab deformation (Figure 5.6d). A similar effect has been observed for a non-Newtonian plate viscosity (Figure 5.6e). The numerical model that best represents the laboratory experiment in terms of plate deformation (slab deformation and trench curvature) is obtained by reducing the plate thickness to 1.0 cm (Figure 5.6f). However, the evolution of this model (model N11) is notably slower (214 min) than that corresponding to laboratory experiment (150 min).

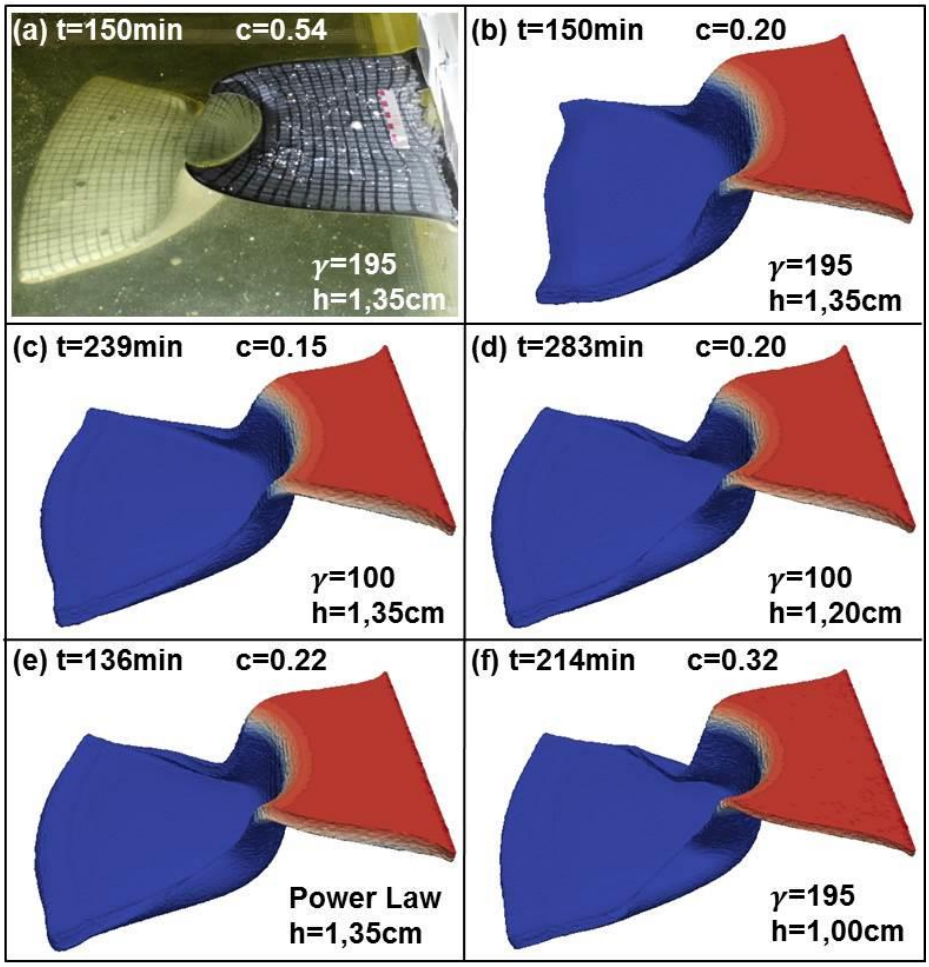

Figure 5.6 Single subduction model of 30 cm wide plate at time evolution t carried out in the laboratory and by numerical modelling applying different contrast viscosity ($\gamma = \eta_l/\eta_m$) and plate thickness (h). (a) Laboratory experiment L2; (b) Numerical model N10; (c) Numerical model N12; (d) Numerical model N13; (e) Numerical model N15; (f) Numerical model N11. See parameters in Table 5.1. c indicates the trench curvature defined as the ratio between the chord and the sagitta of the circular segment delineated by the trench (equation 4.2).

5.2.5 Results

Reducing the computational domain allows to increase the model resolution without increasing the computational cost and therefore, to simulate the laboratory experiment with more spatial accuracy. Regarding to the size of the computational domain, negligible differences in terms of plate geometry and trench retreat velocity are obtained when reducing the numerical domain from 150 x 150 cm^2 to 80 x 80 cm^2 and 40 x 30 cm^2 for 10 cm wide plates (Figures 5.2, 5.3). In terms of trench retreat, the numerical model that best matches the laboratory experiment is model N3 (40 x 30 cm^2), which allows the highest resolution (Table 5.1). However, the toroidal flow for this model is narrower than those for the medium and large models, due to the proximity of the lateral walls to the slabs. The effect of applied free-slip/no-slip lateral boundary conditions on the trench retreat

velocity is only noticeable for the small-box numerical models (Figure 5.4). Indeed, the velocity magnitude observed on the lateral walls of the box for models with free-slip lateral boundary conditions indicate the stronger influence of the lateral walls on the mantle flow for the small box model N3 (see Figure S1 in the Supplementary material).

The choice of bottom boundary conditions strongly affects the slab geometry, independently from the model domain size (Figure 5.5). The slab deformation and temporal evolution of the subduction system observed in the laboratory experiment is better reproduced by numerical models having no-slip boundary conditions at the bottom of the model domain.

The strong effect of rheology and plate thickness on plate deformation is evident from the results obtained from numerical models of single subduction with 30 cm wide plates (Figure 5.6). The model with non-linear viscosity plate (model N15; Figure 5.6e) shows the best similarity with the laboratory experiment in terms of plate deformation and time evolution, indicating that the materials used in the laboratory may be not perfectly linear viscous. On the other hand, changing the plate thickness or the viscosity contrast between plate and mantle strongly affects the temporal evolution of the subduction system (Figure 5.6).

To study the evolution of subduction processes with opposite polarity in adjacent plate segments I choose a numerical setup consisting of a medium box size (80 x 80 cm^2) with boundary conditions of free-slip at the lateral walls and no-slip at the bottom of the model domain (model N2; see Table 5.1). This model shows the best trade-off between numerical resolution, trench curvatures, deformation of plates, and trench retreat velocities. To make it comparable with analog results, viscosity values for plates and mantle are adopted from previous laboratory experiments (see Chapter 4).

5.3 Numerical model of subduction with opposite polarity in adjacent segments

In the following, I present the results obtained from the numerical model N2 consisting of two 10 cm wide plates with an initial separation of 1 cm (Table 5.1). The interaction between both plates is investigated by analysing (1) mantle flow, (2) stress and energy dissipation, (3) plate deformation and (4) trench retreat velocity. Results are compared with those from a numerical model of single plate subduction (model N8) and

the respective laboratory experiment (model L1, Table 5.1) complementing the results of both modeling methodologies.

5.3.1 Mantle flow

The mantle velocity field induced by the double plate subduction process is calculated at different times and depth levels (fully shown in the Supplementary material; Figures S2-S5). Figure 5.7 shows the three-component velocity field at 6 cm depth of the model domain corresponding to intermediate mantle depths, and the horizontal mantle flow direction in the background.

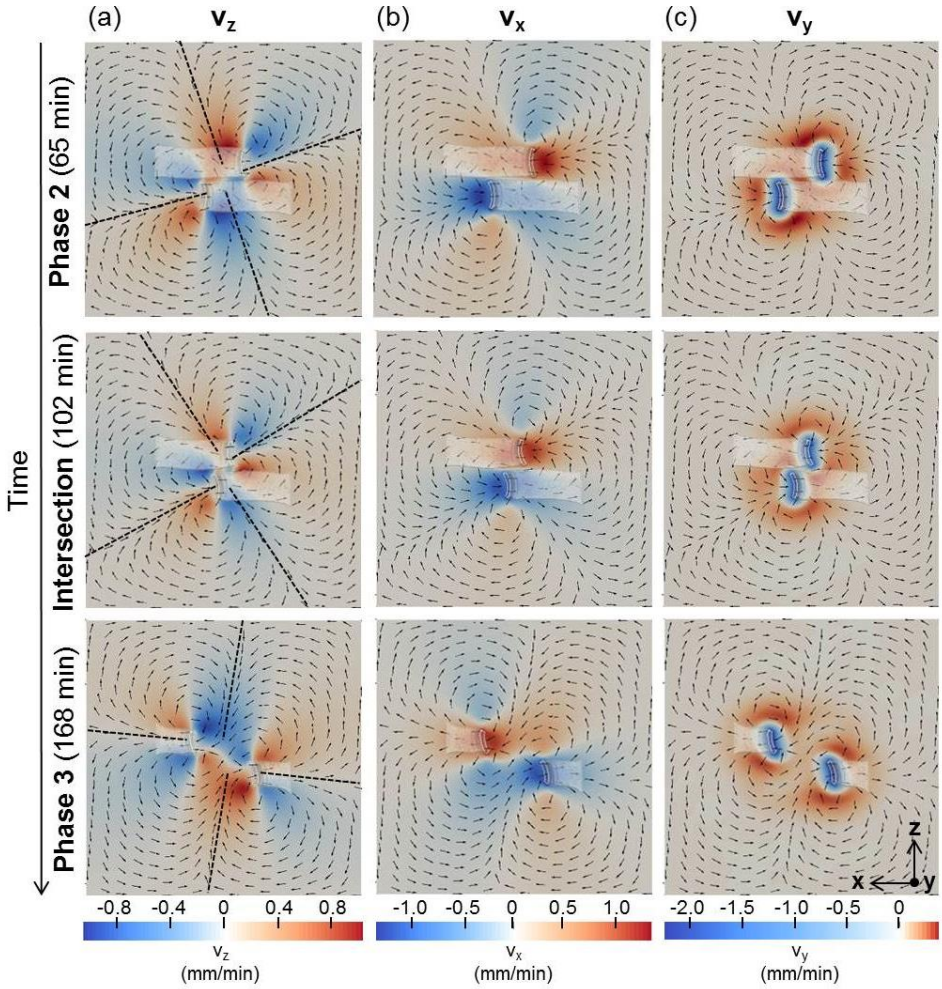

Figure 5.7 Temporal evolution of double subduction model N2, shown in top view. Black arrows show the flow direction in the x-z plane at 6 cm depth from the top of the model domain. Background colors indicate the velocity magnitude of the (a) v_z, (b) v_x and (c) v_y components. Stippled straight lines mark the directions of convergent and divergent flows associated with the toroidal cells, which are roughly orthogonal and rotate counter clockwise through time.

The initial model geometry shows a rotational symmetry of second order with the rotation point at the center of the model. This symmetry pattern is also observed in the circulation of the mantle flow through the whole evolution of the system, which is characterized by four large toroidal cells with flows converging towards the front-side of the trenches and diverging outwards from the backside of the trenches. The symmetry axes of the cells are roughly orthogonal and rotate counter-clockwise through the different phases as a result of the progressive trench retreating (Figure 5.7). The orientation of these axes, as well as the size of the cells and its symmetry, depends on the initial geometry of the system (plate width, plate separation, and box size). In my experiment, during phases 1, corresponding from minutes 0-53, phase 2, corresponding from minutes 53 - 102, and early phase 3, corresponding from minutes 102 - 140, the induced toroidal mantle flow is asymmetrical with respect to the longitudinal axis (x-direction) of each plate particularly in the back-side of the trenches (see also Figure 5.8). The two toroidal cells around the adjacent lateral slab edges push the plates towards each other and merge into a single cell during trench intersection. During late phase 3 (>140min), the interaction between the adjacent plates vanishes and the toroidal flow cells become nearly symmetrical in the back-side of the trenches but strongly asymmetrical in the front-side.

The velocity component v_z, perpendicular to the plates, is the most affected by the interaction between the two plates (Figure 5.7a). During phases 1 and 2, this component is stronger at the external backside of the slabs because the inner toroidal cells associated with the return flow around the slab have opposite directions in the inter-plate region. Merging of the two inner toroidal cells is observed through the trench-parallel vectors in the inter-plate region during plate intersection. When slabs cross each other at 6 cm depth this component becomes stronger in the inter-plate region reaching its maximum value (1.1 mm/min). As phase 3 progresses, maximum values of v_z component are observed at the outer front side of the slabs. In contrast, the v_x component shows roughly the same pattern during the entire evolution, being higher in front of the slabs (Figure 5.7b). Maximum values ($v_{x\_max} \approx 1.5$ mm/min) are registered when ending phase 3. The vertical velocity component v_y at intermediate mantle depths shows a general upwelling affecting the regions around plates that is compensated by the plate's downwelling and the adjacent mantle drag. However, important variations are observed in the inter-plate region (Figure 5.7c).

Figure 5.8 shows the mantle flow of model N2 in three dimensions during trench intersection (Figure 5.8a) and the evolution of the velocity field along a cross-section

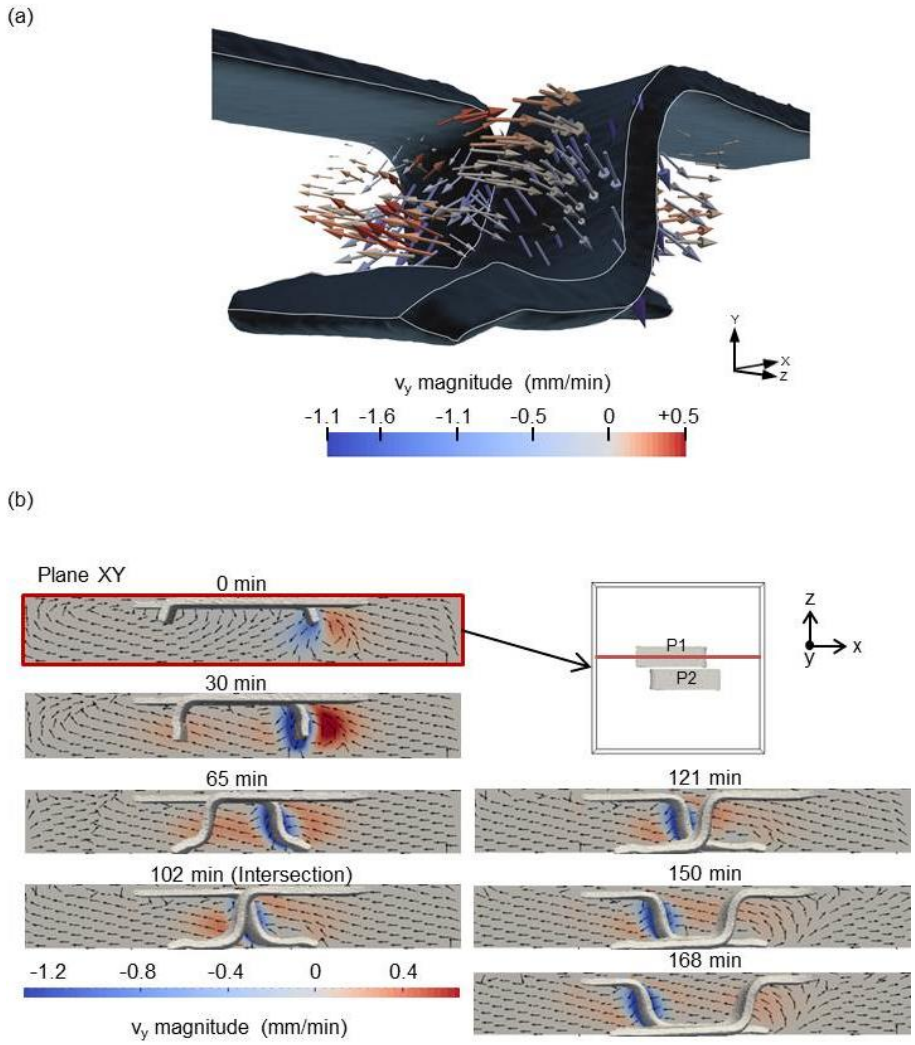

Figure 5.8 Double subduction model N2 showing: a) 3D view of the velocity field during intersection of trenches; b) time evolution of the flow direction in a cross-section through a subducting plate (see inset). Background colors indicate the vertical component of the velocity field v_y where red and blue correspond to upward and downward movement, respectively.

through one of the subducting plates (Figure 5.8b). The circulation in front and behind the slab is mostly poloidal incorporating the mantle material displaced by both plates in a vertical plane. Maximum upward velocities occur during Phase 1 (time evolution < 53 min) in front of the slab persisting through all the process but with a lower intensity. During Phase 2 (from 53 min to 102 min) there is a noticeable upward velocity component affecting the region behind the slab that is vanishing along Phase 3. In the inter-plate region, the mantle material flows upwards associated with the front side of the slabs (Figure S5). These upwelling flows approach each other as the subduction progresses changing during trench intersection when upwelling is associated with the backside of the slabs. During intersection, the mantle flow in the inter-plate region

changes direction generating a downward vertical flow that is not observed in other regions of the mantle or during other phases (Figures 5.7c and S2-S5).

5.3.2 Stress and energy dissipation

A different way of studying how plates interact each other through the generated mantle flow is analyzing the stress distribution and the total energy dissipated during the subduction process. Figure 5.9 shows the effective stress, σ_{II}, calculated at intermediate mantle depth (6 cm from the top of the model domain) and the direction of the horizontal velocity field. At this depth, effective stress values of 0.6 Pa are registered in the mantle regions adjacent to the slabs during the entire subduction process. However, as the subduction progresses, the stress increases from 0.05 Pa to more than 0.2 Pa in the vicinity of the internal sides of the slabs reaching the maximum values (> 0.45 Pa) in the inter-plate region during the trench intersection. In the course of phase 3, the mechanical coupling vanishes progressively. A similar stress distribution is observed at different depths of the mantle.

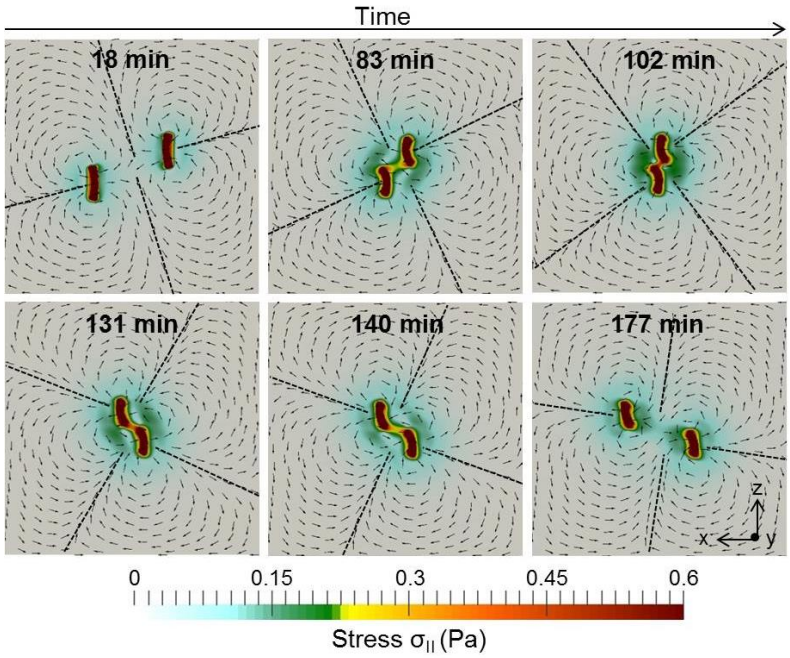

Figure 5.9 Temporal evolution of double subduction model N2, shown in top view. Black arrows show the flow direction in the x-z plane at 6 cm depth from the top of the model domain. White areas denote the location of the slabs. Background colors indicate the effective stress calculated in the mantle at this depth. Stippled straight lines mark the directions of convergent and divergent flows associated with the toroidal cells, which are roughly orthogonal and rotate counterclockwise through time.

Additionally, I have calculated and compared the energy rates dissipated by the mantle of both single and double plate subduction models as shown in Figure 5.10. In the double subduction model the maximum rate of energy dissipation occurs during phase 1 reaching ~$1.2 \cdot 10^{-6}$ W before the slabs arrive to the base of the box decaying rapidly to ~$0.3 \cdot 10^{-6}$ W. During phase 2 the energy dissipation rate increases again until $0.9 \cdot 10^{-6}$ W and decreases to a stable value of ~$0.7 \cdot 10^{-6}$ W until minute 150. From minute 150 to the end of subduction (minute 200) there is a steady increase in the energy dissipation rate up to $0.9 \cdot 10^{-6}$ W. The dissipated energy rate for the single plate model (model N8) shows a similar pattern with values that are slightly larger than half of those calculated for the double plate model. Indeed, the total dissipated energy calculated for a single plate (0.0044 J) is half of that corresponding to a double plate system (0.009 J) considering 200 minutes of evolution in both cases. This released energy represents ~16% of the total potential energy of the system, the rest being partly held as potential energy as plates are still subjected to their trailing edges, and partly being dissipated by plate deformation.

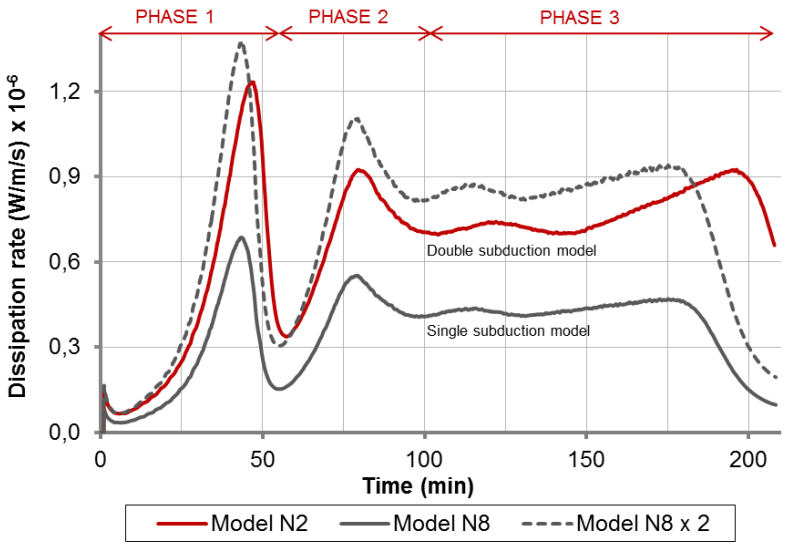

Figure 5.10 Energy dissipation rate associated with mantle flow of numerical models N2 (double subduction) and N8 (single subduction). Dashed line would correspond to the energy dissipation rate of two isolated plates. The indicated phases refer to the double subduction model.

5.3.3 Plate deformation

To analyse the plate deformation in the double subduction process corresponding to model N2, I have calculated the mantle velocity field at 1.2 cm depth from the top of the model domain (Figure 5.11), and the second invariant of the strain rate undergone by the

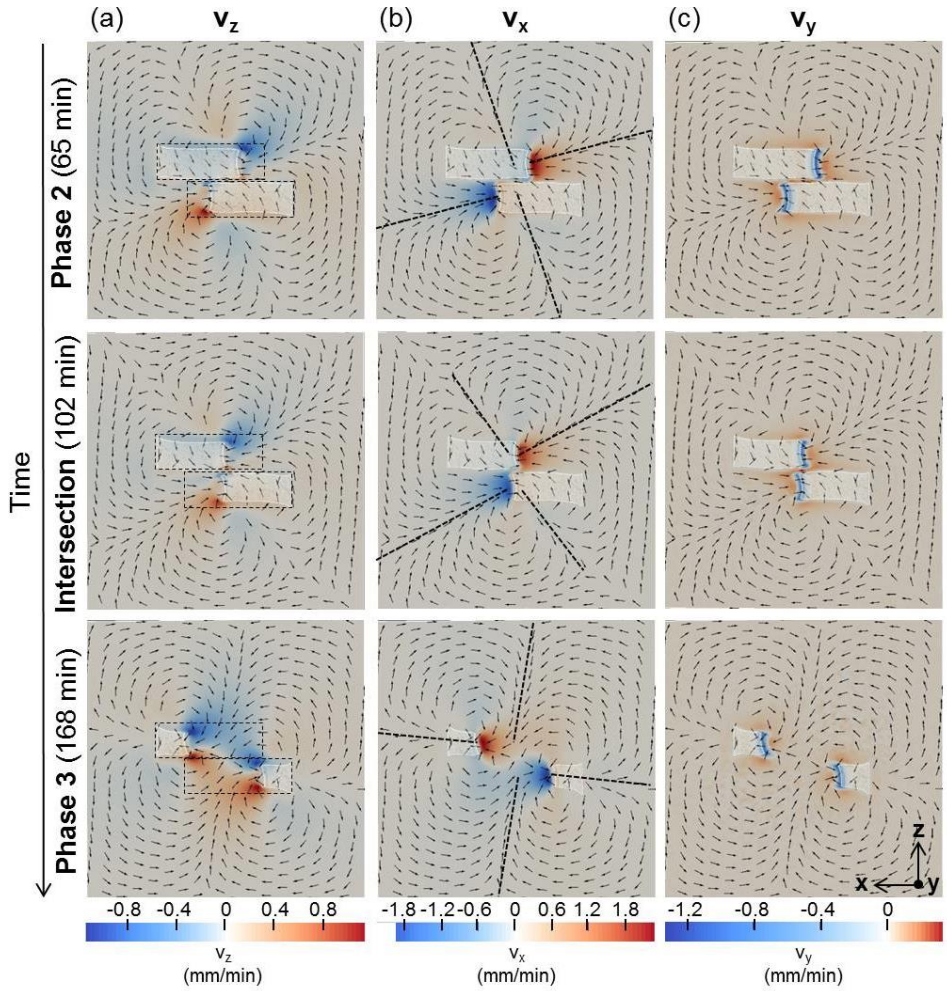

Figure 5.11 Uppermost mantle flows and plate deformation of double subduction model N2, shown in top view. Black arrows show the flow direction in the x-z plane at 1.2 cm depth from the top of the model domain. Background colors indicate the velocity magnitude of the (a) v_z, (b) v_x and (c) v_y components. Dashed rectangles in panel (a) indicate the initial geometry of plates.

plates (Figure 5.12). The velocity field observed at the plate level indicates that, from the beginning of the experiment until early phase 3, the mantle flow pushes the plates towards each other in a direction perpendicular to their respective longitudinal axes producing a lateral movement of both plates (Figure 5.11). This is also observed in Figure 5.12 in which strain rate increases from the centre of the plates to their borders as a result of lateral movement. A lateral bending is produced on the plates when trenches intersect, which is enhanced at depth in the inter-plate region as subduction progresses. Trenches show a symmetric curvature that slightly decreases with time accompanied of a counter clockwise rotation due to the lateral movement of plates (Figures 5.11, 5.12). As expected, the highest strain rates occur in the regions where plates bend vertically, i.e. near the trench and at the bottom of the model where plates get horizontal.

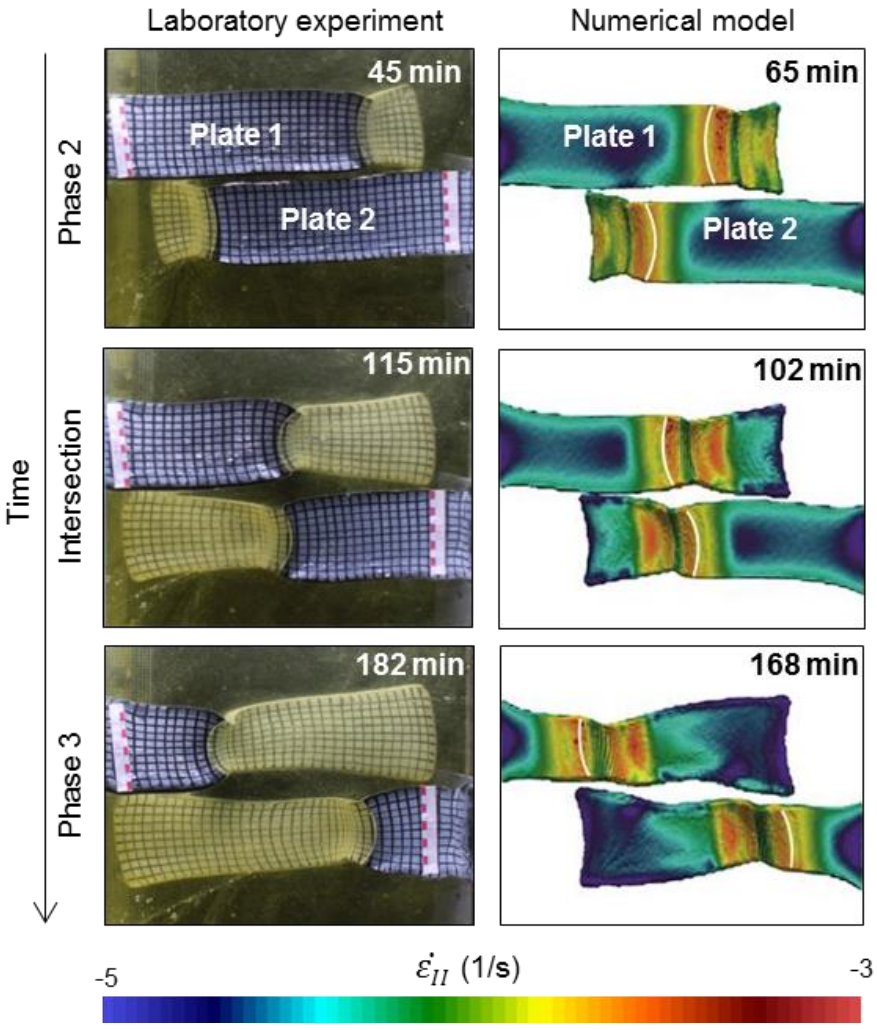

Figure 5.12 Temporal evolution of double subduction models with 10 cm wide plates carried out in the laboratory (model L1) and by numerical modelling (model N2), shown in top view. Colors indicate the second invariant of the strain rate (logarithm scale).

5.3.4 Trench retreat velocity

Figure 5.13 shows the time evolution of trench retreat velocity for single and double plate subduction systems. In the double subduction model, trench retreat velocities of both plates are equal due to the symmetry of the initial setup and only one is shown. Phase 1 is characterized by a fast trench retreat until ~40 min, followed by a velocity decrease until the tips of the plates reach the base of the model box at around 53 min (Figure 5.13). During phase 2, trench retreat velocity increases again reaching a maximum of ~1.6 mm/min followed by a short period of velocity decrease before trenches intersect at around 102 min. Phase 3 is characterized by a progressive increase in retreat velocity reaching maximum values of ~ 1.9 mm/min at the late stage of evolution. The single plate model (model N8) shows similar trench retreat velocity

variations during all phases of the subduction process although is slightly faster reaching a maximum velocity of 2.1 mm/min during phase 1 (Figure 5.13).

The higher trench retreat speed computed in the single plate model relative to the double plate model is consistent with the calculated energy dissipation rate, which is slightly higher than half of that for the double plate model (Figure 5.10). As the total energy is exactly half, the time over which the energy rate is integrated must be lower and therefore, the velocity faster.

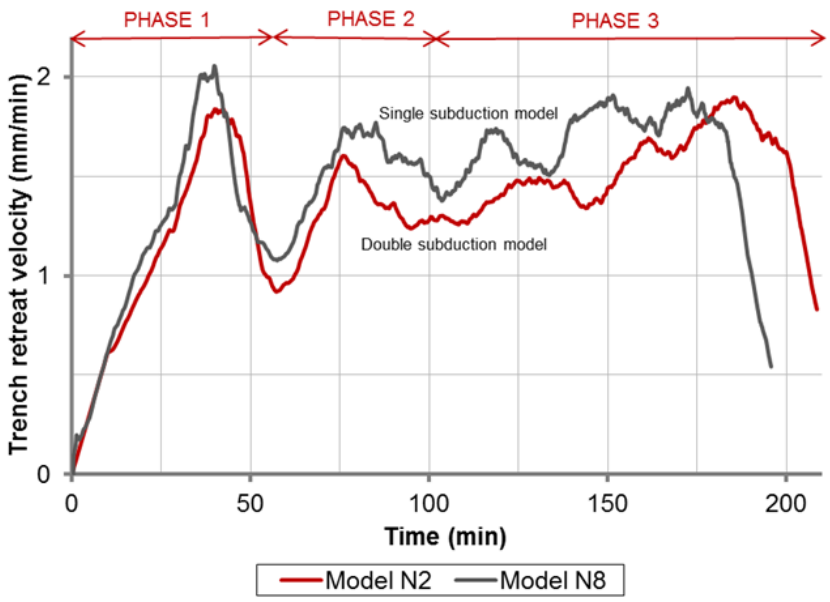

Figure 5.13 Trench retreat velocity vs time of numerical models N2 (double subduction) and N8 (single subduction). The indicated phases refer to the double subduction model where only one plate is shown due to symmetry of the initial setup.

Supplementary material

(Figures S1 to S5)

This supplement contains five figures including more detailed information about the numerical models of subduction systems with opposite polarity in adjacent segments presented in Chapter 5. Results are discussed in the main text.

Figure S1

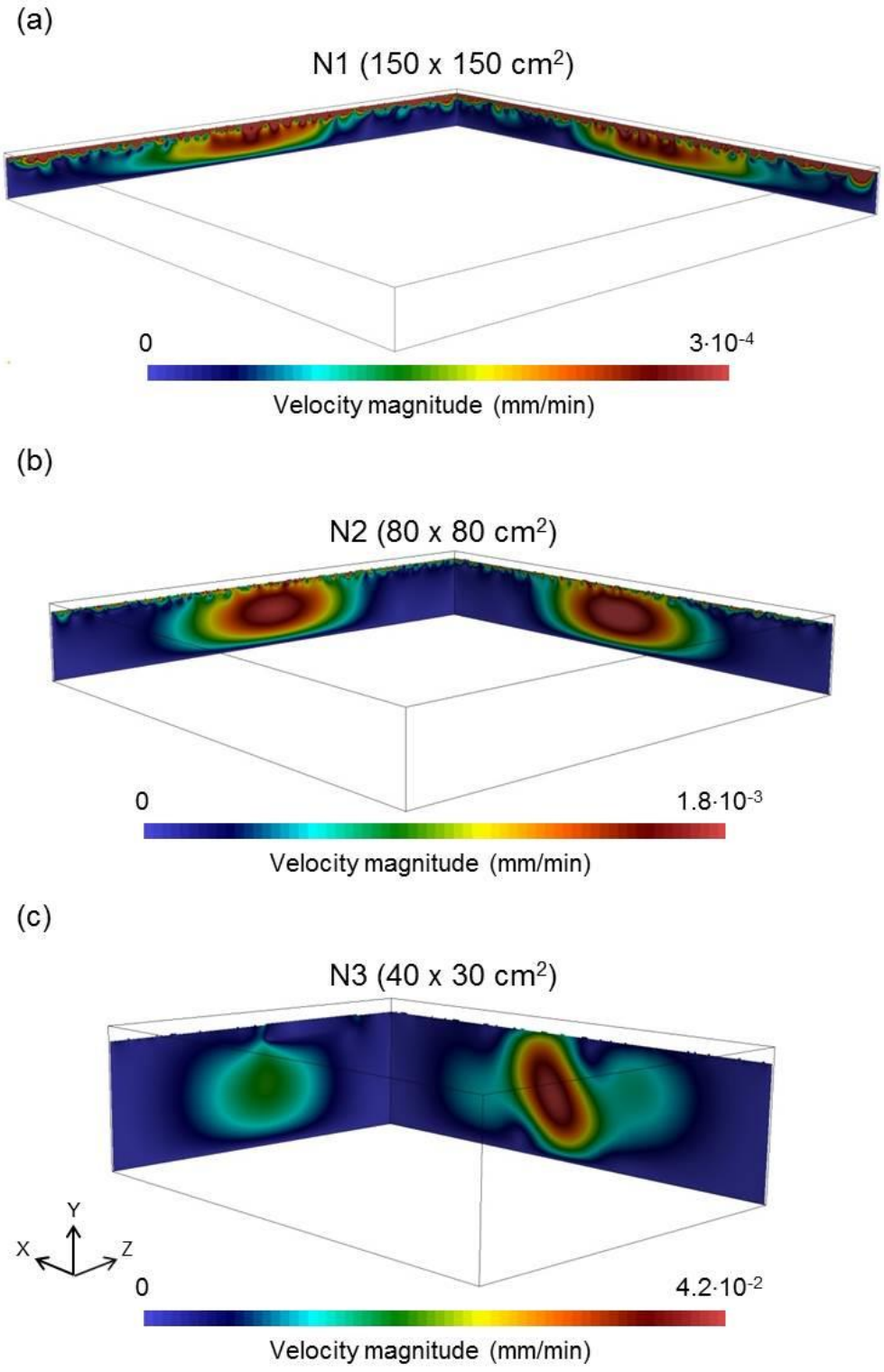

Figure S1 Velocity magnitude on the side walls for models (a) N1, (b) N2 and (c) N3. Note that the size of the model boxes is not on scale with respect to each other.

Figure S2

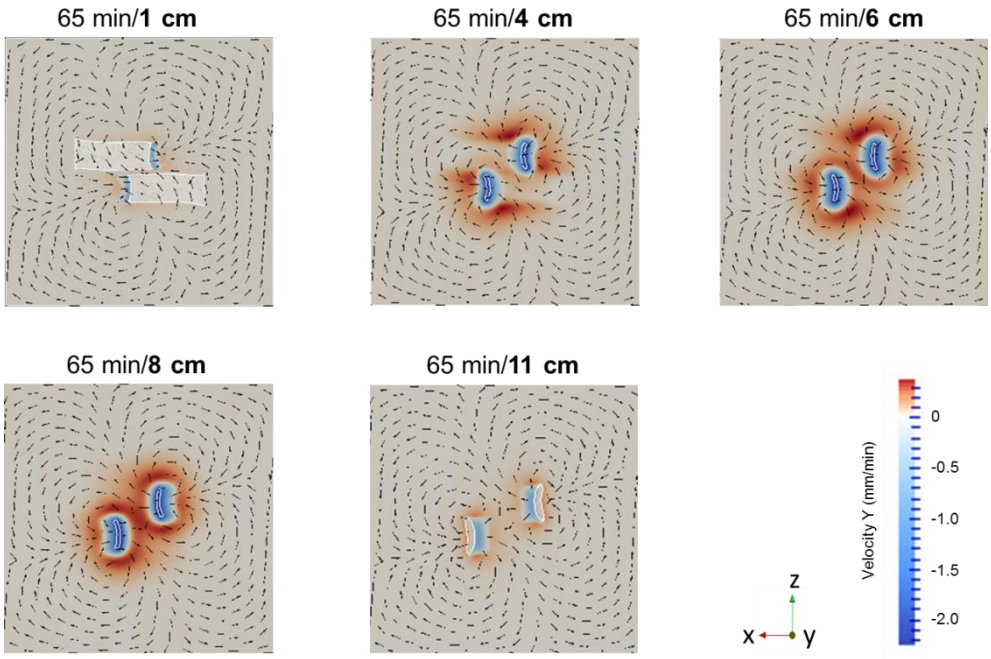

Figure S2 Double subduction model N2 at minute 65 showing the velocity field in the x-z plane at different depths from the top of the model domain. Colors indicate the velocity magnitude of the vertical component v_y. Red colors indicate upward mantle flow while blue colors indicate downward mantle flow.

Figure S3

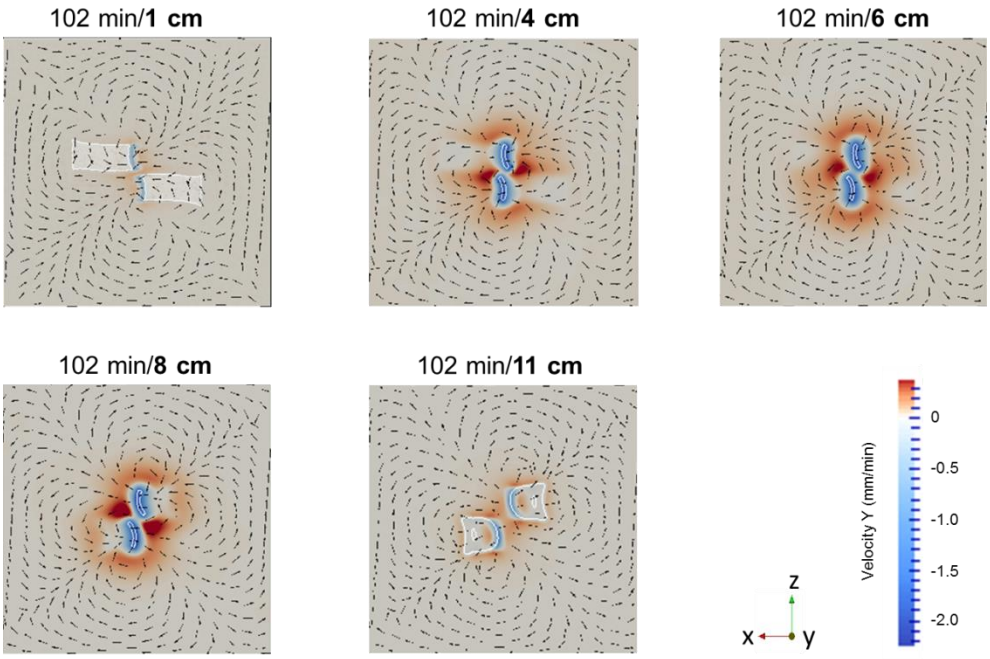

Figure S3 Double subduction model N2 during intersection (minute 102) showing the velocity field in the x-z plane at different depths from the top of the model domain. Colors indicate the velocity magnitude of the vertical component v_y. Red colors indicate upward mantle flow while blue colors indicate downward mantle flow.

Figure S4

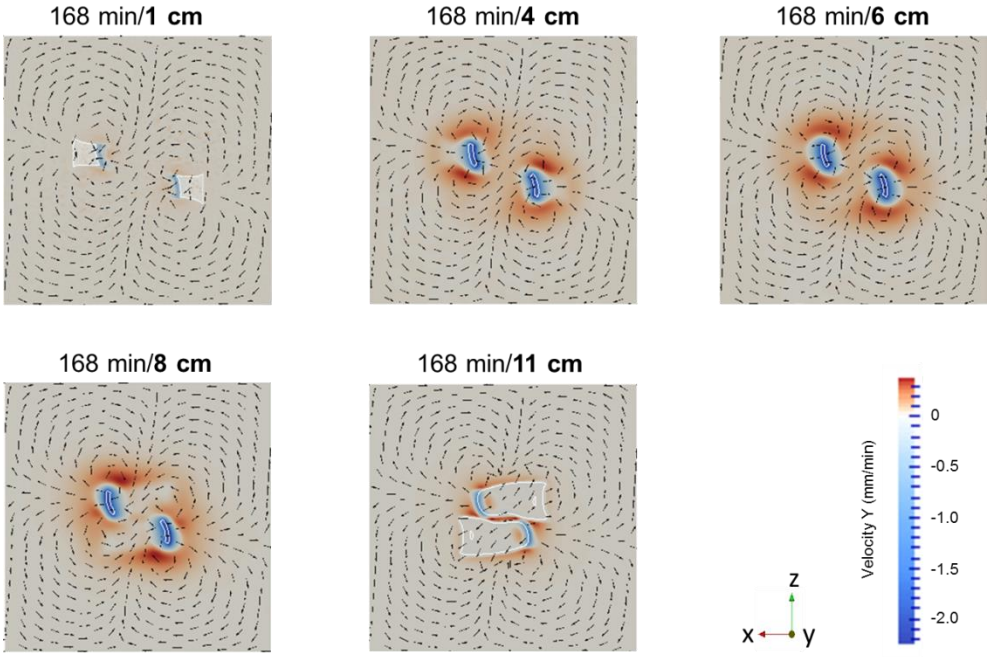

Figure S4 Double subduction model N2 at minute 168 showing the velocity field in the x-z plane at different depths from the top of the model domain. Colors indicate the velocity magnitude of the vertical component v_y. Red colors indicate upward mantle flow while blue colors indicate downward mantle flow.

Figure S5

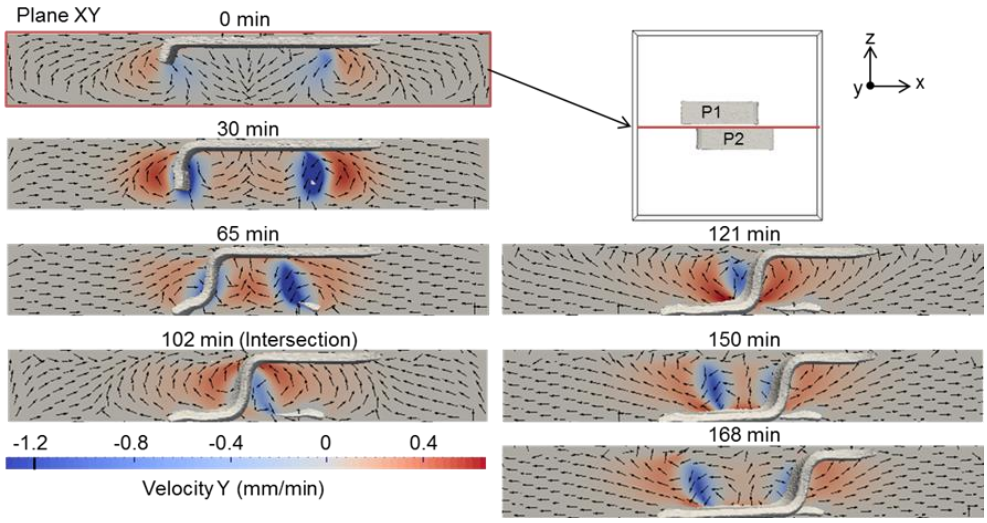

Figure S5. Time evolution of double subduction model N2 showing the velocity field in the inter-plate region. Colors indicate the velocity magnitude of the vertical component v_y. Red colors indicate upward mantle flow while blue colors indicate downward mantle flow.

CHAPTER 6

The Alboran and Algerian basins (Westernmost Mediterranean). A case study of double subduction with opposite polarity in adjacent segments

Chapter 6

The Alboran and Algerian basins (Westernmost Mediterranean). A case study of double subduction with opposite polarity in adjacent segments

In this Chapter, I present a 3D numerical model of the geodynamic evolution of the Westernmost Mediterranean region based on the interaction of two subducting plate segments retreating in opposite directions. Such setup was proposed by *Vergés and Fernàndez* [2012] and further supported by *Casciello et al.* [2015] and *Fernàndez et al.* [2019] to reconcile the formation of the Betic-Rif arc and the accretion of high pressure and low temperature (HP/LT) metamorphic complexes in the Kabylies (northern Algeria) and the Betic-Rif orogen (southern Iberia) in a unique tectonic evolution. Despite of that, there is no consensus on the geodynamic evolution of this region. To date, only a 3D geodynamic study based on numerical modeling has been performed to analyze the most plausible tectonic scenario among those proposed during the last two decades [*Chertova et al.*, 2014]. These authors conclude that the model proposed by *Vergés and Fernàndez* [2012] comes close to the presently observed slab morphology though they favor a model based on the westward migration of a single subduction slab initially located beneath the Balearic Promontory.

The numerical model presented here shows that double polarity subduction is a feasible mechanism in the tectonic scenario of the Westernmost Mediterranean. The time evolution of the two adjacent plate segments retreating in opposite directions and the

formation of the arcuate trench associated with the Betic-Rif orogen is consistent with the recent kinematic model of Iberia-Africa proposed by *Macchiavelli et al.* [2017] and the opening of the Alboran and Algerian basins. Mantle flow and slab plate deformation are analyzed showing that the effects of the interaction between both plates in such tectonic scenario are similar to that obtained in previous numerical models of double polarity subduction (see Chapter 5).

6.1 Geological setting

The Alboran and the Algerian basins are located in the westernmost part of the Mediterranean, confined between the Iberian Peninsula and northwestern Africa (Figure 6.1). These basins and the surrounding mountain ranges are associated with the NW-SE convergence between the African and Eurasian plates and the closure and subsequent subduction of the Ligurian-Tethys oceanic segments and their formation is genetically associated with the Apennines in Italy and the Tellian system in North Africa [e.g., *Carminati et al*., 1998; *Gueguen et al*., 1998; *Rosenbaum et al*., 2002; *Faccenna et al*., 2004; *Rosenbaum and Lister*, 2004; *Spakman and Wortel*, 2004; *Platt et al*., 2013; *Faccenna et al*., 2014a; *Royden and Faccenna*, 2018]. The Betic-Rif system has an arcuate structure and shows five major tectonic domains: a) the Guadalquivir and Gharb foreland basins and their continuation into the Gulf of Cadiz, b) the non-metamorphic External Betics and Rif units, c) the Flysch units separating the external and the internal units, d) the HP/LT metamorphic complexes of the Internal Betics and Rif units, and e) the Alboran Basin occupying the inner part of the arcuate system. The Alboran Basin is considered as a back-arc basin mainly formed during the Miocene and characterized by a thin continental crust in the west, a magmatic-arc crust towards the east and an oceanic crust in the easternmost part [*Platt and Vissers*, 1989; *García-Dueñas et al*., 1992; *Maldonado et al*., 1992; *Comas et al*., 1999; *Torne et al*., 2000; *Booth-Rea et al*., 2007]. Exposures of HP/LT metamorphic complexes are also observed in the Kabylies (Algeria) at the NE of the Tellian system. Contrary to the Betic-Rif, the Tellian system is an East-West oriented linear mountain belt formed on the southern margin of the Algerian Basin. The geometry and nature of the crust and lithosphere of this region are not so well defined due to the scarcity of geophysical studies, particularly onshore. Offshore studies show that the crust of the Algerian Basin is mainly oceanic with an approximate thickness of about 5 km [*Vidal et al*., 1998; *Mauffret et al*., 2004; *Mauffret et al*., 2007*; Leprêtre et al*., 2013; *Medaouri et al*., 2014].

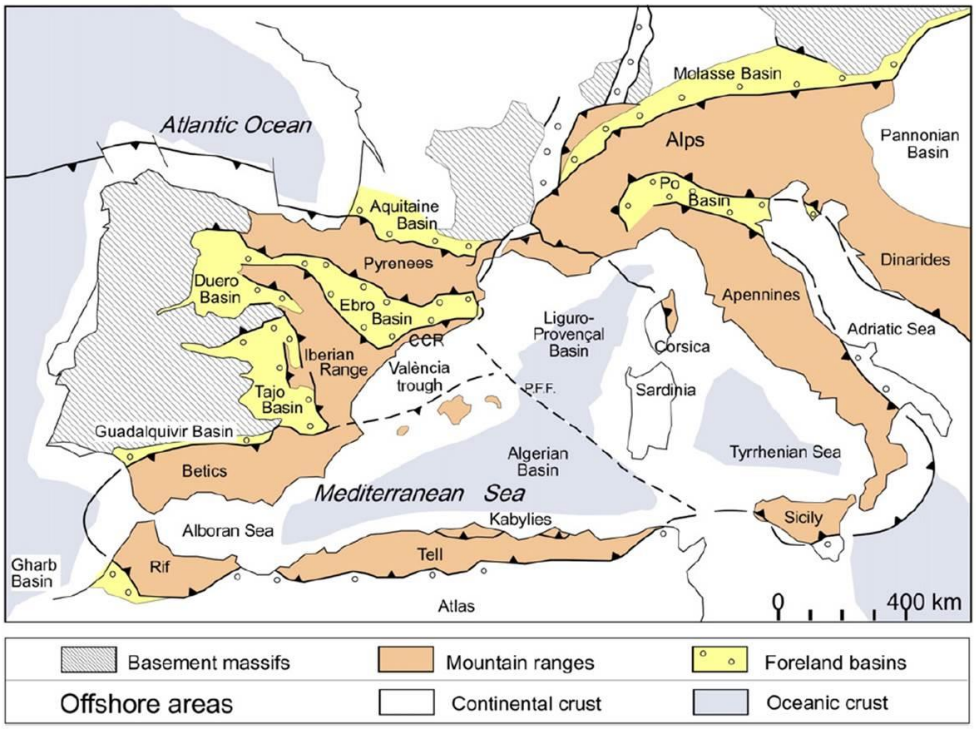

Figure 6.1 Tectonic map of the Western Mediterranean showing the main orogenic belts and foreland basins [*Vergés and Sàbat*, 1999].

The complex geological history of the Westernmost Mediterranean still generates a focus of debate among the geoscientific community. Indeed, several tectonic reconstructions of this region have been proposed over the last decades based on different geological processes [e.g., *Andrieux et al.*, 1971; *Platt and Vissers*, 1989; *García-Dueñas et al.*, 1992; *Royden*, 1993; *Lonergan and White*, 1997; *Calvert et al.*, 2000; *Doblas et al.*, 2007; *Jolivet et al.*, 2009; *Handy et al.*, 2010; *Carminati et al.*, 2012; *Vergés and Fernàndez*, 2012; *Van Hinsbergen et al.*, 2014]. Currently, the most accepted geodynamic process driving tectonic changes in this region is the subduction rollback, supported by recent high resolution tomographic models and geochemical data from magmatic rocks [e.g., *Duggen et al.*, 2004; *Duggen et al.*, 2005; *Duggen et al.*, 2008; *Fichtner and Villaseñor*, 2015]. However, the initial geometry and subsequent evolution of the rollback process is still under discussion. Some authors suggest an initial NW dipping slab limited to the Balearic margin (Figure 6.2A) [e.g., *Spakman and Wortel*, 2004; *Van Hinsbergen et al.*, 2014]. Others propose an initial long N-NW dipping subduction zone that extends from Gibraltar to the Balearic Promontory (Figure 6.2B) [*Rosenbaum et al.*, 2002; *Faccenna et al.*, 2004; *Jolivet et al.*, 2009; *Carminati et al.*, 2012; *Do Couto et al.*, 2016]. Finally, a S- to SE-dipping initial subduction under North Africa is also proposed [*Gelabert et al.*, 2002; *Vergés and Fernàndez*, 2012].

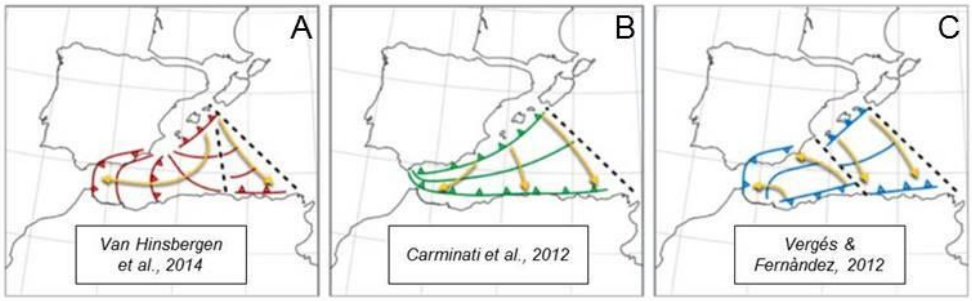

Figure 6.2 Three different scenarios of the evolution of the Westernmost Mediterranean. (A) Scenario A starts from an initial short subduction zone near the Baleares [e.g. *Van Hinsbergen et al.*, 2014]. (B) Scenario B starts from a long initial trench along the Gibraltar-Baleares margin [e.g. *Carminati et al.*, 2012]. (C) Scenario C involves a tectonic history of the region starting from a S-SE dipping subduction zone under African margin [e.g., *Vergés and Fernàndez, 2012*]. Yellow arrows represent the direction of the rollback. Black dashed lines represent the proposed transform faults. Modified from [*Chertova et al.*, 2014].

According to *Vergés and Fernàndez* [2012], a double polarity subduction process is involved in the evolution of this region. Their hypothesis, based on plate reconstructions models and tectonic, sedimentary and metamorphic data sets, suggests the existence of two opposite dipping subductions in adjacent segments during the late Oligocene-Miocene: (i) a subduction dipping to the northwest and retreating to the southeast, related to the migration of the Kabylies (Algerian-Tethys segment), and (ii) another subduction dipping to the southeast and retreating to the northwest originating the Betic-Rif arc (Alboran-Tethys segment) (Figures 1.1 and 6.2C). An important point of this reconstruction is the initial configuration of the Ligurian-Tethys domain during the Late Cretaceous, considering that the Iberian and the African margins were strongly segmented due to transtensive tectonics during the early Jurassic. Indeed, the boundary between the two opposite subduction zones is described as a transform fault of the originally segmented Ligurian Tethys domain [*Frizon de Lamotte et al.*, 2011; *Schettino and Turco*, 2011]. This assumption, moreover, is consistent with the opposite vergence of HP/LT metamorphic complexes in the Betic-Rif (Internal units) and the Tellian (Kabylies units) systems that can be connected with this NW-SE old Ligurian-Tethys transform fault (Figure 1.1). Another important consideration of the geodynamic model proposed by *Vergés and Fernàndez* [2012] is the timing of the subduction-related orogenic processes starting in Late Cretaceous. In this way, the Alboran back-arc basin was formed close to its present position in contrast to the other afore mentioned geodynamic models in which it traveled for several hundred kilometers after subduction initiation.

6.2 Model setup

The numerical model is set up to reproduce a simplified version of the tectonic evolution of the Westernmost Mediterranean region with the main goals of reproducing the formation timing of the Alboran and Algerian basins and the position and arcuate shape of the lithospheric slab beneath the Betics-Rif orogen. The model must be consistent with the tectonic scenario inferred from plate reconstruction models in the region. Following the assumptions made in Chapters 4 and 5, and in published numerical models of subduction [e.g., *Stegman et al*., 2010; *Piromallo et al.*, 2006; *Li and Ribe*, 2012; *Király et al*., 2016; *Mériaux et al*., 2018], the model setup does not include overriding plates and tectonic convergence between Iberia and Eurasia to simplify the numerical calculations. Therefore, the considered tectonic domains are: the Alboran-Tethys and the Algerian-Tethys plate segments retreating in opposite directions, and three continental blocks corresponding to the Iberia and African plates (Figure 6.3). The Alboran-Tethys segment dips to the southeast with the trailing edge fixed to the Iberia margin, and the Algerian-Tethys segment dips to the northwest with the trailing edge fixed to the African margin. A continental African block west to the Alboran-Tethys plate segment is included simulating the transition between the Tethys and the Atlantic oceans.

The domain of the numerical experiment is 1320 x 660 x 1830 km in the X (north-west), Y (depth) and Z (north-east) directions, respectively, and encloses the actual approximate region from latitude 34°N to 44°N, and from longitude 10°W to 10°E (Figures 6.3 and 6.4a). A regular mesh (128 x 64 x 192) is used with 40 particles per element in the initial setup. This results in a total of 1.572.864 elements and 62.914.560 markers. The dimensions of the tectonic domains are assigned considering the plate kinematic reconstruction of the region proposed by *Machiavelli et al*. [2017] since Upper Cretaceous (83.5 Ma). Since the model does not include tectonic convergence, an initial subduction of ~150 km is needed to create self-sustained subduction [e.g., *McKenzie*, 1977; *Royden and Faccenna*, 2018]. The Iberia-Africa convergence is characterized by moderate N-S velocities of 4.5 mm/yr between 83.5 - 71 Ma followed by a quiescent period from 71 to 33 Ma amounting a total convergence of ~90 km in NW-SE direction (Fig. 6.3). An additional convergence of 50-70 km must be added related to the relative movement between Africa and Iberia during the period between 115 and 83.5 Ma [*Macchiavelli*, pers. comm.].

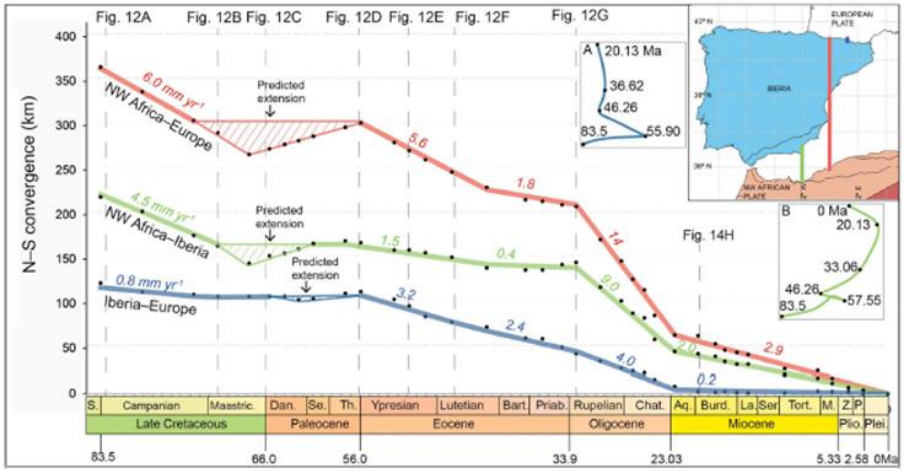

Figure 6.3 Diagram showing the N-S convergence rates between NW Africa and Europe (in red), between NW Africa and Iberia in the Betic domain (in green) and between Iberia and Europe in the Pyrenean domain (in blue) since 83.5 Ma. Figure from *Macchiavelli et al.* [2017].

Therefore, the kinematic reconstruction between Iberia and Africa indicates that at late Eocene – early Oligocene, the Ligurian-Tethyan domains already underwent a subduction of about 150 km. At that time (~35 Ma) the dimensions of the non-subducted Alboran-Tethys and Algerian-Tethys domains were of ~700 x 390 km and ~600 x 620 km, respectively (Fig. 6.4).

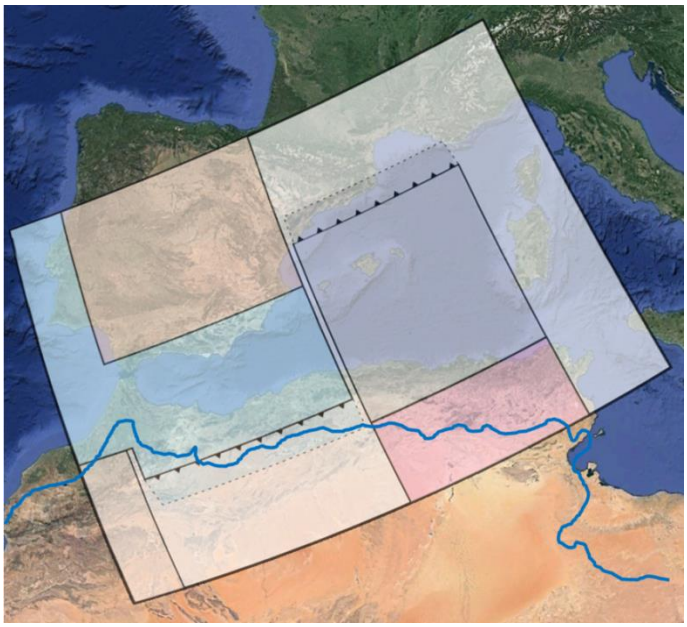

Figure 6.4 Scheme of the model setup above a present day map of the Western Mediterranean. Note that the model setup initiates at ~35 Ma so the relative position between Iberia and Africa was over a greater distance. In blue, the position of the coast line at 35 Ma according to *Macchiavelli et al*. [2017].

The setup of the numerical model is summarized in Table 6.1 and Figure 6.5. Both plate segments initiate the subduction process with a typical dip angle of 45° [e.g., *Royden and Faccenna*, 2018] and an initial subduction of 150 km.

Table 6.1 Main parameters of the numerical model of the Alboran-Algerian system (model A1) and the reference model (model A2).

NUMERICAL MODELS OF THE ALBORAN AND ALGERIAN BASINS				
Model		**#Oceanic segments**		**Numerical resolution (km)**
A1: Alboran-Algerian system		2		10.3x10.3x9.5
A2: Reference model		1		10.3x10.3x9.5
	Rheology	**h (km)**	**ρ (kg/m^3)**	**η (Pa·s)**
Mantle				
	viscous	660	3300	10^{20}
Oceanic segments				
Layer 1	visco-plastic	16	3210	10^{22}
Layer 2	viscous	16	3400	$10^{23.5}$
Layer 3	viscous	38	3400	10^{22}
Continental segments				
	viscous	110	2700	10^{25}

h: thickness; ρ: density; η: viscosity.

The rheological behavior of the oceanic and continental plate segments and mantle are simplified as follows (Figure 6.5). Mantle is considered isoviscous with a viscosity value of 10^{20} Pa·s [*Ranalli and Murphy*, 1987]. Continental segments are also considered isoviscous and almost rigid with a value of 10^{25} Pa·s. In the model, the role of continents is to act as backstops to impose rollback with fixed trailing edge and therefore, there is no need to impose a more complex viscosity structure. The oceanic domains, initially spaced 30 km representing a transform zone, are the key domains in the model and hence a more complex layered structure is implemented. The oceanic domains consist of three rheological layers: (1) an upper part, representing the crust and behaving viscoplastically, (2) a middle layer, purely viscous, with a high viscosity representing the cold part of the lithosphere and (3) a lower layer also viscous and representing the warmer part until the lithosphere-asthenosphere boundary (LAB) (Figure 6.5b). The rheology of these three layers is a simple version of the usual strength profile of the lithosphere (Figure 3.2a). The thickness assigned to each layer is chosen taking into account the numerical resolution of the model bearing in mind that layers cannot be smaller than a few elements in order to

be properly resolved (Table 6.1). The average density of the oceanic lithosphere is of 3357 kg/m^3, taking into account that the density of the first layer (3210 kg/m^3) results from considering 6 km of oceanic crust with an average density of 2900 kg/m^3 and 10 km of lithospheric mantle with an average density of 3400 kg/m^3 (Table 6.1).

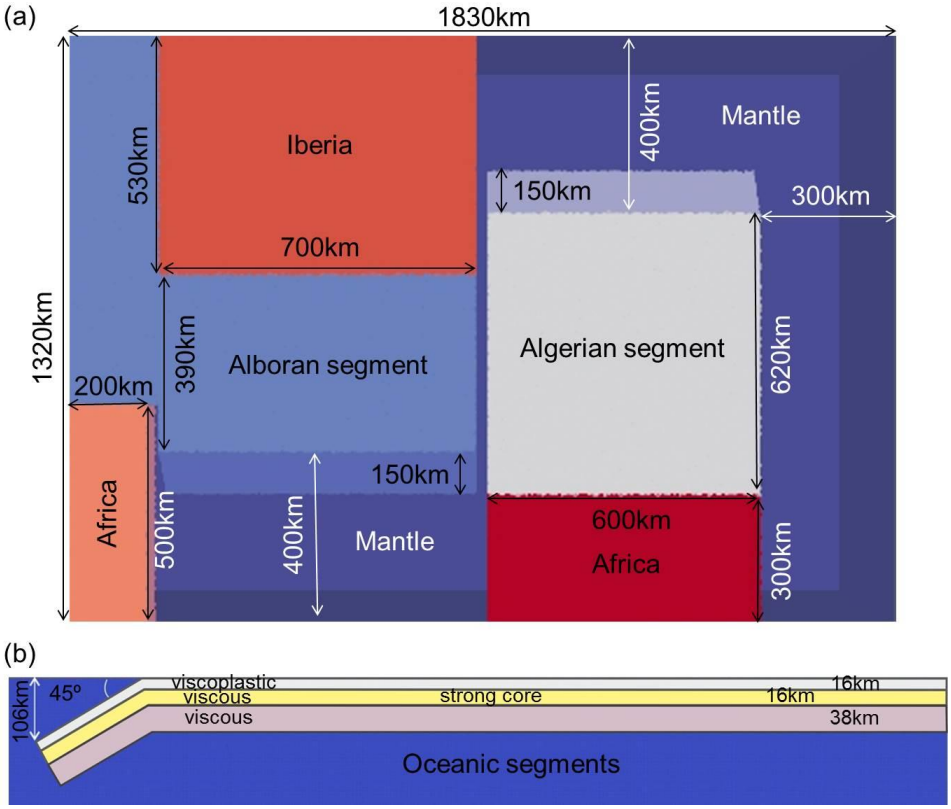

Figure 6.5 Scheme of the double polarity subduction model applied to the Westernmost Mediterranean region (model A1). (a) Top view of the model setup. (b) Lateral view showing the geometry and rheology of the oceanic plate segments.

Boundary conditions are adopted considering a closed domain with appropriate dimensions, i.e., there is no mass flow across the boundaries of the domain. Although this condition is not realistic when compared to nature, it is closer to nature if the walls of the domain are far enough from the system under study. The influence of the distance to the walls in a closed domain was studied in Section 5.2 concluding that a distance of half the width of the plate has negligible influence in terms of plate geometry and trench retreat. Mathematically this translates in imposing zero velocities in the normal direction to the boundaries and zero stresses in the tangential direction. Note that this implies that a plate in contact to a lateral wall cannot advance, as the normal velocity at the wall is imposed to

be zero. The bottom of the model represents the 660 km upper-lower mantle discontinuity which is assumed to be impenetrable with a no-slip boundary condition.

An additional single plate subduction model (model A2; Table 6.1) has been conducted as reference model in order to study the influence of the adjacent plate segment. All model parameters are summarized in Table 6.1.

6.3 Results

Unlike the previous analog and numerical models shown in Chapters 4 and 5, in the case of the Alboran-Algerian system and due to the reduced dimensions of the Ligurian-Tethys corridor, the intersection between the two retreating trenches occurs before the leading edges of the slabs reach the upper-lower mantle discontinuity. Therefore, only two stages are distinguished: stage 1 is defined as the time period while trenches approach each other, and stage 2 is defined as the time period while trenches diverge, i.e. after trench intersection. Results of this chapter are described referring to these stages according to the relative position of the trenches but regardless to the slab depth.

6.3.1 Time evolution

The time evolution of the Alboran-Algerian system is shown in Figure 6.6. The Alboran-Tethys slab shows an asymmetric shape suffering a tight curvature at the western side of the trench. From the beginning of the subduction process, the Algerian-Tethys segment tends to move laterally to the southwest approaching to the Alboran-Tethys segment but keeping a nearly symmetric and constant trench curvature (Figure 6.7; model A1). The trenches cross each other at 12 Ma, before the trailing edges of the slabs arrive to the upper-lower mantle discontinuity at 660 km depth (Figure 6.6). The Algerian-Tethys slab reaches the lower mantle at around 10 Ma whereas the Alboran-Tethys does so at around 6 Ma, the first showing a faster evolution. Moreover, the Algerian-Tethys segment undergoes a greater stretching and slab deformation during the entire evolution. The retreat of the Alboran-Tethys segment spans until 5 Ma in the eastern part when subduction is consumed but continues westwards increasing progressively the curvature of the trench (Figures 6.6 and 6.7).

Figure 6.6 Time evolution of the Alboran-Algerian system (model A1). White lines show the coasts lines of Iberia and Africa at 35 Ma. Note that the convergence between Iberia and Africa is not considered in the model.

6.3.2 Mantle flow

The toroidal component of the mantle flow induced by the subducted slabs of the Alboran-Algerian system at 200 km depth and different stages of its evolution is shown in Figure 6.7 (model A1). For comparison, the mantle flow corresponding to the single Alboran-Tethys slab is also shown (model A2). The numerical model of the Alboran-Algerian system shows a complex mantle flow pattern generating an asymmetric velocity field around both trenches (Figures 6.7 and 6.8). A coupling of the mantle flow generated by each slab is observed around their inner edges identifying three toroidal cells during the whole process (Figures 6.7a and 6.8).

Highest mantle velocities are registered close to the trenches during all the subduction process, being higher for the Algerian-Tethys segment (Figures 6.7 and 6.8). The flow pattern around this plate segment remains nearly constant throughout its evolution although showing changes in the velocity magnitude. On the other hand, the mantle flow pattern in front of the Alboran-Tethys segment is not fully constant changing slightly its direction after trenches intersect (Figures 6.7a, b and c).

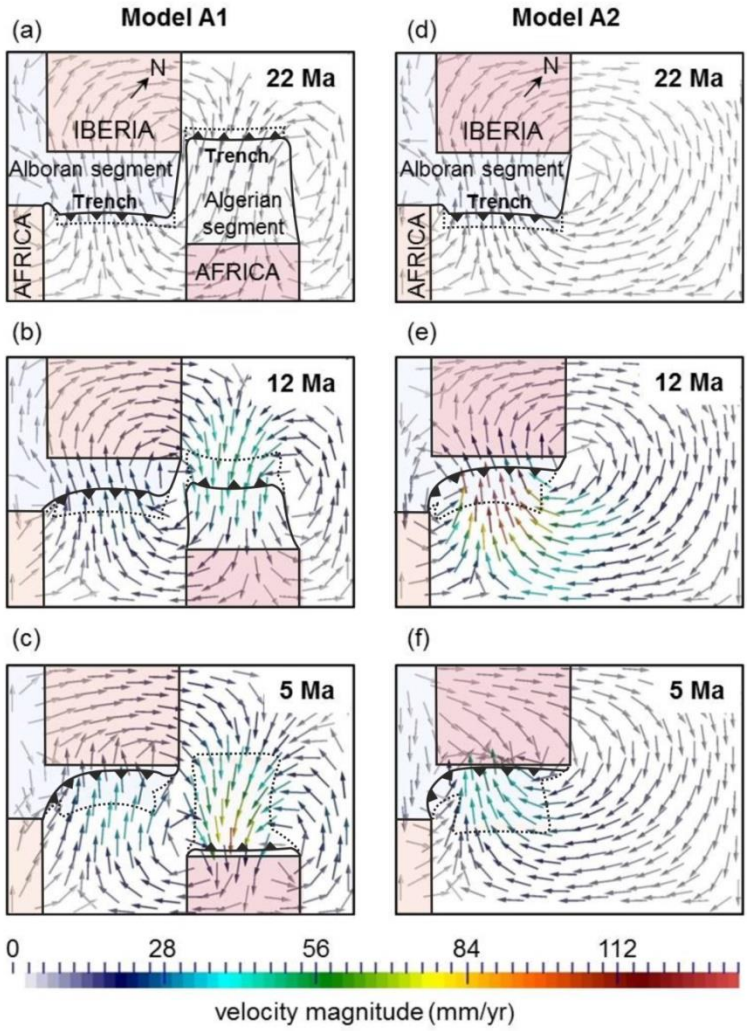

Figure 6.7 Top view showing the velocity field at 200 km depth of the Alboran-Algerian system (model A1) and the reference model (model A2) at different stages of the evolution.

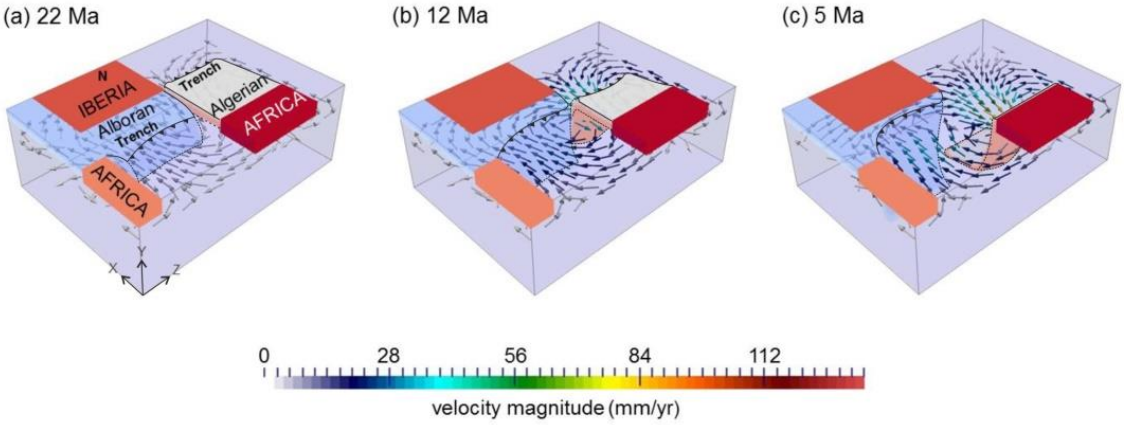

Figure 6.8 Time evolution of the Alboran-Algerian system (model A1) showing the velocity field at 200 km depth.

Figure 6.9 shows the evolution of the vertical mantle flow in a cross-section through the Alboran-Tethys and the Algerian-Tethys segments. The upward mantle flow is concentrated in front of the slabs reaching maximum rates of 30 mm/yr in the Algerian-Tethys segment while trenches cross each other (12 Ma; Figure 6.9b). The vertical velocity of the mantle flow has been also analysed at different depths during different stages of the evolution (Figure 6.10). Maximum downward values are registered always around the slabs reflecting the subduction of the plate segments, the Algerian-Tethys slab showing higher velocities (see also Figure 6.9). Maximum upward velocity values are registered at intermediate mantle depths in front of the slabs (Figure 6.9). The vertical flow in the inter-plate region evolves changing its direction during the two stages (Figure

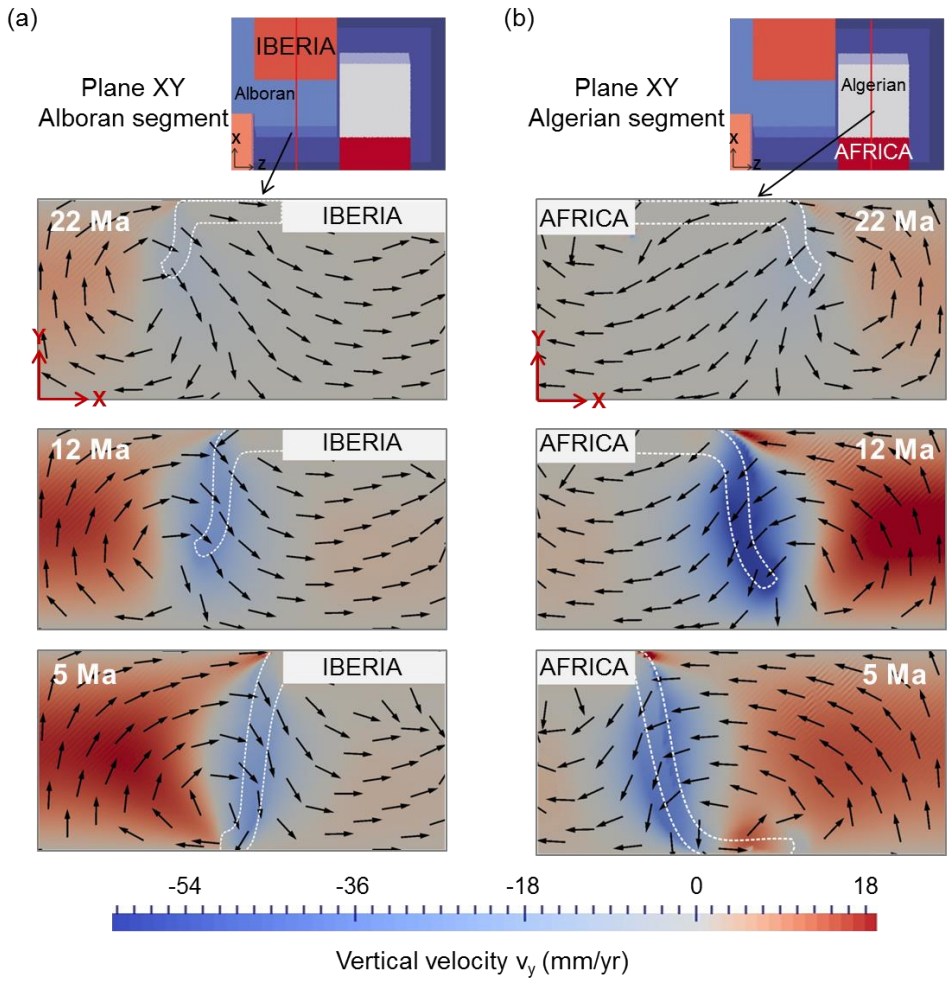

Figure 6.9 Numerical model of the Alboran-Algerian system (model A1) showing the evolution of the vertical mantle flow in a cross-section trough (a) the Alboran-Tethys segment and b) the Algerian-Tethys segment. White dashed lines denote the location of the slabs. Background colors indicate the vertical component of the velocity field v_y where red and blue correspond to upward and downward movement, respectively.

6.10). At stage 1, a nearly zero vertical mantle flow is observed. When trenches intersect (12 Ma), a predominant downward mantle flow is observed being stronger at intermediate mantle depths. In contrast, while trenches diverge (stage 2) a positive vertical mantle flow is observed at any depth.

Model A2, corresponding to a single Alboran-Tethys segment, shows a simpler toroidal mantle flow pattern where the cell around its eastern side has a greater radius of curvature due to the model setup. Unlike model A1, considering the Alboran-Algerian system, the toroidal flow pattern is kept constant during the entire evolution showing higher velocities due to the absence of the Algerian segment. Higher velocity magnitudes within the mantle are registered close to the trench (Figure 6.7, model A2).

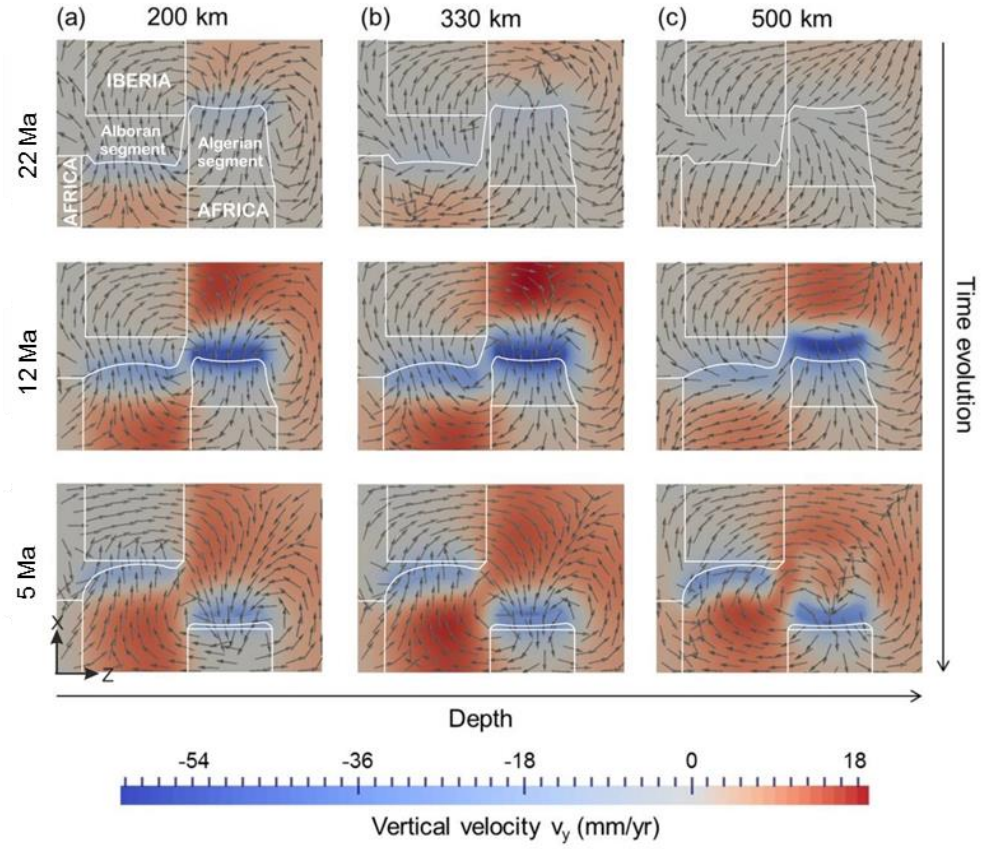

Figure 6.10 Temporal evolution of Alboran-Algerian system (model A1), shown in top view. Grey arrows show the velocity field in the x-z plane and background colors indicate the vertical velocity magnitude v_y at different depths. (a) 200 km depth. (b) 330 km depth. (c) 500 m depth.

6.3.3 Trench retreat velocity

The variations of the retreat velocities of the plate segments through time are relevant to date changes in the tectonic stress orientation, occurrence of magmatism and the opening of the present Alboran and Algerian basins. Thus, the trench retreat velocity of the subducting plate segments is calculated for the Alboran-Algerian system (model A1) and the single Alboran-Tethys segment (model A2). The results obtained, calculated at the central point of the trenches, are shown in Figure 6.11.

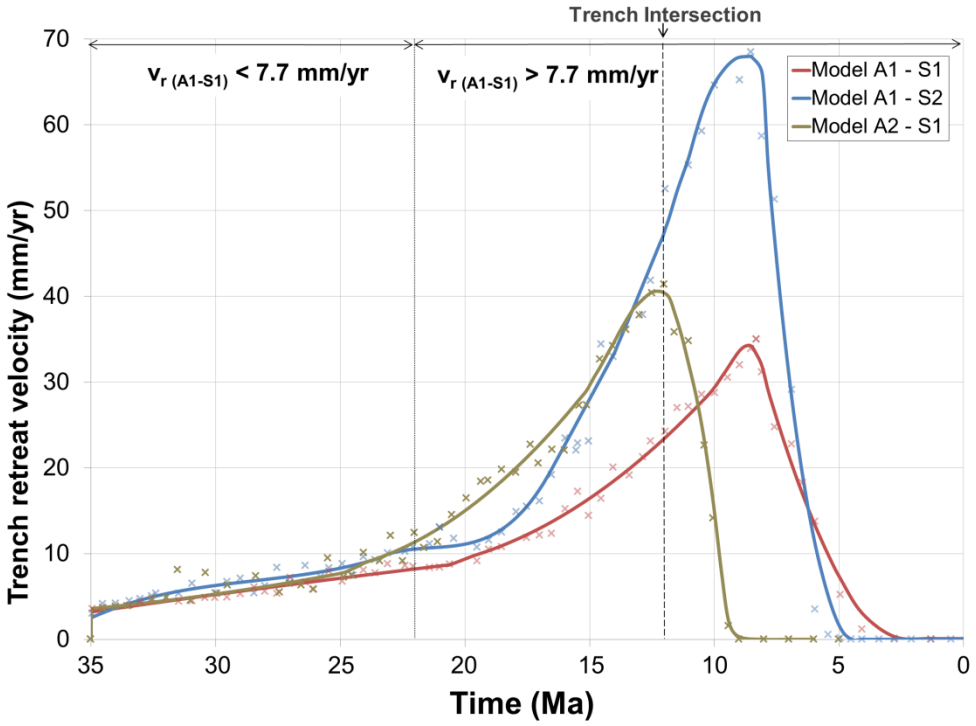

Figure 6.11 Trench retreat velocities vs. time of double polarity (A1) and single (A2) subduction models for the Westernmost Mediterranean region. S1: Alboran plate segment. S2: Algerian plate segment. $v_{r(A1-S1)}$: trench retreat velocity of the Alboran plate segment (Model A1).

Concerning to the Alboran-Algerian system, the trench retreat velocity (v_r) of the Alboran-Tethys segment shows a first period spanning from 35 to 22 Ma in wich v_r is less than 7.7 mm/yr which, according to *Machiavelli et al.* [2017], is the estimated convergence velocity between Iberia and Africa in NW-SE direction at that time (Figure 6.3). During a second period, from 22 to 8 Ma there is a progressive increase of v_r until a maximum value of 35 mm/yr. Afterwards, v_r decreases until zero in a short period of 5 Myr. The mean trench retreat velocity from 22 to 2 Ma is of 15 mm/yr. The Algerian-

Tethys segment shows a faster evolution reaching a maximum retreat velocity that is almost twice that of the Alboran-Tethys segment although during the first 10 Myr of evolution, both plate segments retreat at similar rates. The Algerian-Tethys segment reaches a maximum velocity of 68 mm/yr at 8.5 Ma decreasing very fast to zero in a period of 4 Myr due to the consumption of the subducting plate segment.

As mentioned in previous chapters, the differences in considering a single plate model are noticeable. Model A2 shows higher trench retreat velocities for the Alboran-Tethys segment than for the Alboran-Algerian system (model A1). The maximum reached velocity is 41 mm/yr at 12 Ma, thus occurring 4 My before the model A1. The retreat of the Alboran-Tethys segment ends at 9.5 Ma, just after the slab reaches the lower mantle discontinuity at 10 Ma and coinciding with its consumption.

6.3.4 Curvature evolution of the Alboran-Tethys slab

A major goal of the presented model is to reproduce the present curvature of the Alboran-Tethys slab, which governs the arcuate shape of the Betic-Rif orogen. Figure 6.12 shows the trench displacement of the Alboran-Tethys segment within the framework of the Alboran-Algerian system. Black thick lines denote the position of the trench at the indicated time and velocities are measured perpendicular to the trench at each time and position.

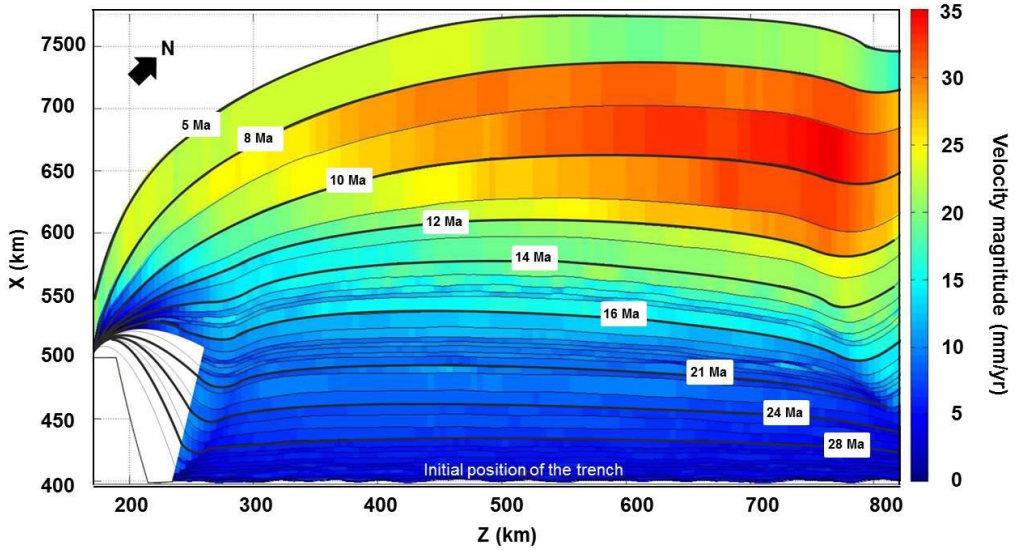

Figure 6.12 Trench retreat velocities vs time of the Alboran segment for model A1. Black thick lines denote the position of the trench at the indicated time. Velocities are measured perpendicular to the trench in each position.

The curvature of the Alboran-Tethys slab increases with time as the plate segment subducts. From the retreat initiation at 35 Ma until 16 Ma, the Alboran segment retreats to the northwest while the trench curvature shows a nearly symmetric shape with respect to its longitudinal axis (Figures 6.7a and 6.12). During this period of time both trench edges retreat along transform zones separating the Alboran-Tethys domain from the Algerian-Tethys domain to the northeast, and from the African continental domain to the southwest. After 16 Ma, the southwestern edge of the Alboran-Tethys segment is pinned at the end of the transform zone and consequently, the eastern edge retreats faster causing the curvature of the trench retreat to the southwest. The curved northeast-southwest orientation of the trench is evident at 12 Ma, coinciding with trench intersection (Figures 6.7b and 6.12). During the time period from 11 to 8 Ma, the trench retreat velocity reaches maximum values exceeding 30 mm/yr in the northeastern half of the segment. From this time on, the curvature of the trench continue to increase to the west-southwest but the retreating velocities decrease showing slightly higher values in the western side of the plate segment (Figure 6.12).

CHAPTER 7

Discussion

Chapter 7

Discussion

The motivation of this thesis was to study the dynamics of subduction systems characterized by opposite dip polarity in adjacent plate segments. The absence of previous studies analyzing the geodynamic evolution of these systems has defined the research strategy of the present work. Consequently, the thesis consists of three different parts combining analog experiments and numerical models of very simple double subduction systems and its application to the Westernmost Mediterranean region.

This chapter has been organized discussing separately the main results obtained in each part of the thesis with a final section wrapping up the common aspects that are significant for a better understanding of the dominant processes that operate in natural scenarios where double subduction with opposite polarity in adjacent plate segments are applicable.

7.1 Analog experiments of subduction systems with opposite polarity in adjacent segments

The interaction of two subducting plates having opposite vergence has been studied through analog modeling by comparing the evolution of the system with single plate subduction. The main distinct features characterizing the double polarity subduction system have been grouped in two main topics.

Induced mantle flow

The main difference between the double polarity subduction system presented and most of the earlier mentioned double-subduction studies (see Section 2.3) is that in models presented here the plates are located side by side and retreating in opposite directions. As a result, the interaction between the individual flow cells associated with each plate produces two effects on the combined mantle flow: i) the flow is not symmetrical with respect to the longitudinal axis of each plate, and ii) the opposed retreating directions preclude a steady state phase of the subduction process.

Figure 7.1 is an idealized cartoon, based on the syrup particle tracks recorded in the different experiments (e.g., Figure 4.5), illustrating the evolution of the mantle flow generated by the double-plate system. Once the plates have reached the impermeable layer at 11 cm depth simulating the upper/lower mantle boundary, the toroidal flow becomes the dominant mantle circulation component especially under fixed trailing edge conditions [e.g., *Stegman et al.*, 2006]. These conditions define an end member subduction setting where toroidal flow is maximal. The toroidal cells generated by the retreating slabs have opposite directions and their encounter induces a shear zone along the region between the two plates. The resulting asymmetric flow beneath each plate causes a net lateral mantle drag that tends to separate the plates (Figure 7.1a). As the two trenches retreat, the more external streamlines merge into a coherent toroidal convective cell connecting both trenches in a progressive feedback process that accelerates the trench retreat (Figure 7.1b). When the trenches become aligned, the toroidal cells merge into one cell and all the streamlines in the inter-plate region follow the same direction producing the maximum trench retreat velocities (Figure 7.1c). As the trenches move away from each other, the toroidal cells related to each slab in the inter-plate region tend to become independent reactivating the shear zone and slowing the trench retreat (Figures 7.1d, e). The mantle flow interaction in the inter-plate region becomes less and less active until subduction is completed.

This general behavior of the mantle has been described in *Király et al.* [2016], but unlike the analog models presented here, their numerical study does not show the progressive separation between the center of the plates. This is because only the half of the plates is modeled with their symmetry axis coinciding with the sidewalls of the model, which are subjected to free-slip boundary thus suppressing trench parallel motion. It must be noted, however, that the separation of plates observed in the analog experiments is favored by the absence of lithosphere at both sides of the double plate system. Despite this is an unrealistic condition in nature, the extensional stresses generated by the

asymmetric mantle flow will persist, whereas the possible shallow effects of the extension perpendicular to the plates are more debatable.

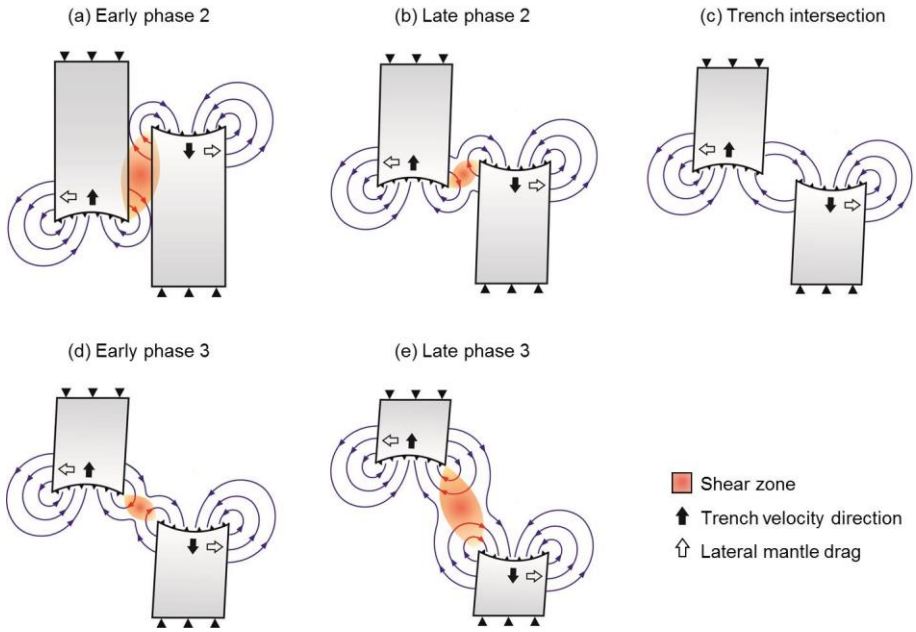

Figure 7.1 Idealized cartoon illustrating the evolution of the mantle flow generated by a subduction system with opposite polarity in adjacent segments. The opposite directions of the return flow in the inter-plate region generate a shear zone that tends to vanish as the trenches approach (a, b, c) and to increase again as the trenches diverge until subduction completes (d, e).

Plate interactions

The possible interactions between plates are associated with the stress propagation through the induced mantle flow and therefore the initial separation between plates must play a relevant role in the evolution of this double plate system. Comparing the normalized trench retreating velocities obtained for configurations with distant plates (Model 1, Figure 4.3) and near plates (Models 2 and 4, Figures 4.4 and 4.6), the velocity variations are related to the initial plate separation d_0 such that the nearer the plates are the higher the variation is. Actually, experiments with near plate configurations show an acceleration and deceleration in the trench retreat during phase 2 and phase 3, respectively. Maximum velocities are attained close to the moment when the trenches align with each other. In contrast, distant plate configurations show roughly steady state trench retreat velocities. This is in agreement with the results obtained by *Király et al.* [2016] showing that when plates are separated by distances larger than 600 km (10 cm in my experiments) the interaction between plates is negligible. Interestingly, Model 5,

encompassing near wide (30 cm) and narrow (10 cm) plates, shows also roughly steady state retreating velocities (Figure 4.7). The possible reason lies in the negligible effect that the narrow plate 2 produces on the wider plate 1. Consequently plate 1 behaves as an independent single plate pushing outwards plate 2 and causing small variations in its retreating velocities due to the large separation created between both plates. On the other hand, the strong toroidal flow related to plate 1 largely deforms the other, narrow plate.

The interaction between near plates generates a progressive lateral separation between the trench centers, which is more noticeable for narrow plates as evidenced by comparing Models 2 and 4. Plate separation is a measure of the lateral deformation of plates, which depends on the drag exerted by the mantle flow and the bending resistance related to plate viscosity such that the narrower the plates are, the larger the lateral separation between them is.

The trench curvature appears to be independent on the initial separation of plates and therefore on the plate interaction related to the opposite subduction polarity process, as evidenced by comparing Models 1 and 2 (Figures 4.3 and 4.4). A consequence of this is that trench curvature increases steadily throughout phase 2 and 3 as observed in all models. Note that the variations in the normalized trench retreating velocities are very low producing an unnoticeable change in the curvature trend line. Near-plate configurations seem to produce asymmetric trench curvatures though we cannot ascertain whether they are a consequence of the asymmetry in the generated mantle flow or to spurious errors in the experiment setup. By comparing Model 2 and 4 (Figures 4.4 and 4.6) and Model 1 and 5 (Figures 4.3 and 4.7), the trench curvature mainly depends on the plate width such that wider plates show larger curvatures in agreement with previous works [e.g., *Funiciello et al.*, 2003; *Schellart*, 2010a]. Trench curvature also depends strongly on the viscosity ratio between plates and underlying syrup and although this study is not designed to systematically analyze this dependence, it has been observed that trench curvature in experiment E5 (Table 4.2, $\frac{\eta_l}{\eta_m} = 202$) is significantly greater than in experiment E6 (Table 4.2, $\frac{\eta_l}{\eta_m} = 256$), with similar values for all the other parameters. Therefore, differences in curvature between Models 1 and 2 can be due to small variations in the viscosity ratio $\frac{\eta_l}{\eta_m}$ (Table 4.2). The curvature values calculated for the latest stages of Model 2, with plates 30 cm wide, are close to c = 0.8 meaning that the arc delineated by the trenches corresponds to ¾ of the circumference. Such closed arc-trenches are not easily observed in nature, where tightest arcs (e.g., Gibraltar Arc, Calabrian Arc, Scotia Arc, Caribbean Arc, Banda Arc, Carpathians Arc) show maximum values of c = 0.4-0.5. This

discrepancy between analog models and nature can be due to the absence of overriding plate in our experiments, which overestimates the curvature of the trench, as proposed by *Meyer and Schellart* [2013].

7.2 Reproducing analog experiments of subduction systems with numerical modeling

A suite of numerical models has been presented reproducing the conditions of previous laboratory experiments [Chapter 4; *Peral et al*., 2018] with the final goal of quantifying the physical parameters characterizing the evolution of a double polarity subduction system. In this section, the results obtained are discussed according to three main topics: (1) the choice of the numerical model, (2) the dynamics of double subduction models and (3) the comparison with previous analog experiments of double polarity subduction.

Setup of the numerical model

Results from numerical and laboratory models agree when considering an intermediate domain size (80 x 80 cm^2) with free-slip boundary conditions in the lateral sides and no-slip in the bottom of the numerical model. First order observations like timing of the process, plate and trench geometries, plate deformations and mantle flow are similar in both models. The two methodologies produce also slight differences. For example, the experimental uncertainties related to the handling process of the laboratory experiments can lead to asymmetries between plates in the initial stages of the evolution of the system or to slight modifications in the rheology of materials. However, it is found that these factors, which are complex to quantify, produce only second order differences.

Aside these differences related to inaccuracies from the experimental handling, there are some others related to simplifications made in the numerical approach. First, concerning to analog models, the mechanical contact between the plate and the bottom of the tank shows a non-negligible amount of friction that prevents lateral bending of the subducted lithosphere while allows for their stretching (Figure 5.12). When a free-slip condition is applied at the bottom of the numerical model, the generated geometries do not properly coincide with those observed in the analog models. However, the geometries become much similar when no-slip conditions are imposed. The situation resembling the behavior of the natural prototype is probably in between these two end-member cases

and hence, a calibrated amount of friction should be considered in future numerical models to tailor more realistic geometrical fits.

Second, numerical models cannot reproduce simultaneously the large trench curvature and the retreat velocity observed in laboratory experiments, particularly for wide plates, even when varying the model rheological parameters (Figure 5.6). The reasons for that can be i) the rheology of laboratory materials might have a slight non-Newtonian component, and/or ii) the syrup simulating the mantle reacts with the air generating a thin "crystalized" layer that might generate some surface forces not considered in the numerical model [e.g., *Mériaux et al.*, 2018].

Dynamics of double subduction systems: insights from numerical models

Mantle flow in an ideal single slab subduction system is characterized by a toroidal component that is symmetric relative to the longitudinal axis of the slab. In the case of two adjacent slabs with opposite polarity, the toroidal flows induced by each slab interact with each other generating different flow patterns in both the inter-plate and outer mantle regions. Consequently, the resulting toroidal component of the mantle flow becomes asymmetric relative to the slabs axes (Figures 5.7, 5.11).

Deformation of plates is coupled to the mantle flow and, therefore, it is affected by mantle flow asymmetry producing a lateral movement of the plates and slabs in double subduction systems (Figure 5.12). The deformation undergone by the slabs at depth (lateral bending) is related to the mantle drag exerted by the net outward flow trying to separate one plate from the other. This drag appears while trenches approach and its strength decreases with the distance between the slabs, so its effect is maximum during the intersection of the two trenches. A similar behavior has been reported by *Király et al*. [2016]. The interaction between the flows generated by the two slabs enhances the energy dissipation rate almost doubling its value. As a consequence, the trench retreat velocities in a double subduction system are slowed down with respect to a single subduction process (Figures 5.10, 5.13).

Despite the strong interaction between plates in a double subduction system, the evolution of the trench velocity through time shares some common features with the single subduction system. Obviously these similarities are stronger during the initial and final stages of the evolution, when the two slabs are distant and the interaction of their induced mantle flows is weaker. For example, as reported elsewhere [e.g., *Funiciello et al*.,

2003; *Schellart*, 2004a; *Funiciello et al*., 2006; *Strak and Schellart*, 2014], trench velocity increases rapidly at the beginning of the model whilst the slab is sinking and the negative buoyancy increases (Figure 5.13, 0 to ~40 min). When the slab reaches the bottom of the domain, the trench velocity slows down (40 to 55 min) and accelerates again (55 to 75 min) until the steady-state subduction is achieved (75 to 180 min). During the steady-state period, the single subduction system shows some minor periodic accelerations and decelerations (Figure 5.13) probably due to changes in the slab angle. These changes are not so evident in the double subduction system as the interaction between slabs and mantle flow can partly overprint the slab dip changes.

Comparing numerical and analog results of double subduction systems

Analog experiments of double subduction systems with opposite polarity in adjacent segments show that during the retreating process, plates tend to separate each other with the maximum separation coinciding with the trench intersection [Chapter 4; *Peral et al*., 2018]. Moreover, those results indicate that the rollback velocities slightly increase through time until reaching a maximum when trenches intersect each other and afterwards decrease again. These results, however, are not completely confirmed by the numerical models thus suggesting some differences in the interaction mechanisms between plates.

Because plates are not in contact with each other, the only mechanism responsible for differences between analog and numerical models is the stress field generated by the mantle flow during the retreat of the slabs. Stresses generated in the inter-plate region in both numerical and analog models, tend to drag the plates separating them from each other (Figure 4.5b, 5.9 and 5.12). Whereas in numerical models the resulting deformation of plates shows a lateral movement that brings the central parts of the plates closer together, analog models show a divergent displacement of the two plates (Figures 5.11, 5.12). This discrepancy can be explained by the different radii of the toroidal cells generated in both experiments, which seems to be larger in the numerical than in the analog models independently on the size of the modeling domain (Figure 5.2). The different mantle flow patterns generated in numerical and analog experiments and the associated energy dissipation are also responsible for the differences in the time evolution of the trench retreat velocities.

Restrictions in the computational resolution and implemented boundary conditions in numerical models, along with experimental uncertainties in the analog setup, could

generate these mantle flow differences. However, it is more likely that are the different rheological properties between analog and numerical materials which produce the distinct behaviour. Actually, I have shown the impossibility to reproduce both observed curvature and time evolution of wide plate experiments using linear rheologies. Concerning to the shapes of subducting plates, asymmetric trench curvatures are observed in both numerical and laboratory experiments (Figure 5.12) suggesting that these asymmetries are related to the mantle flow interactions associated with double subduction systems.

Reproducing numerically a laboratory experiment is not straightforward. Indeed, other authors already found differences in the sinking and retreating rates, as well as in plate morphology, when attempting to numerically reproduce laboratory experiments of single plate subduction [*Schmeling et al*., 2008; *Mériaux et al*., 2018]. Performing both models simultaneously could help us to control all the parameters affecting the evolution of the system. In addition, a more detailed study of the mantle flow in analog experiments is needed to better understand the observed differences.

7.3 The Alboran and Algerian basins (Westernmost Mediterranean). A case study of double subduction with opposite polarity in adjacent segments

The modeled subduction system with opposite polarity in adjacent segments explains the dominant geodynamic mechanisms acting on the Westernmost Mediterranean region allowing to correlate the obtained results with the temporal evolution of the subduction process, the initiation of the back-arc extension in the present Alboran and Algerian basins, and the present day geometry of the Alboran-Tethys slab.

According to *Macchiavelli et al*. [2017] the maximum convergence velocity (v_c) between Iberia and Africa in NNW direction is of 7.7 mm/yr and occurs between 33-22.5 Ma. Later on the convergence velocity decreases until 3.2 mm/yr until present. The initiation of extension in the Alboran Basin will occur when the trench retreat velocity is higher than the convergence velocity ($v_t > v_c$), otherwise the tectonic regime will be dominated by compression. The results obtained here indicate that during the first 8 Myr of evolution, i.e. between 35-22 Ma, the retreating velocity is lower than the convergence velocity and therefore, back-arc extension in the Alboran Basin would initiate at around 22 Ma (Figure 6.11), which roughly coincides with estimations from geological data (20-

23 Ma) [e.g., *Comas et al.*, 1999; *Gómez de la Peña et al.*, 2018]. Geophysical and geological observations also reveal that the retreat of the Alboran-Tethys slab became essentially inactive around 6-8 Ma [e.g., *Berástegui et al.,* 1998; *Iribarren et al.,* 2007] thus indicating that the tectonic activity related to slab retreat spanned over a period of 12-17 Myr. This time span matches perfectly the estimated duration of the retreating process from the presented model.

Tomographic models of the Westernmost Mediterranean region shows the presence of a predominantly oceanic subducted lithosphere that extends from under the Rif-Gibraltar region curving to the NE and E under the eastern Betics [e.g., *Villaseñor et al.,* 2015]. The arcuate geometry of the Alboran-Tethys slab produced by its NW- to W-retreating is consistent, as a first-order approximation, with tomographic observations though the observed curvature is higher than that reproduced by the model (Figure 7.2). To this respect however, it must be noted that the numerical model does not incorporate the Africa-Iberia convergence that, according to *Macchiavelli et al*. [2017], amounts 140-150 km in N-S direction from about 35 Ma to present. This convergence would produce a northward displacement of the pinning point of ~150 km and hence, a further tightening of the modeled slab.

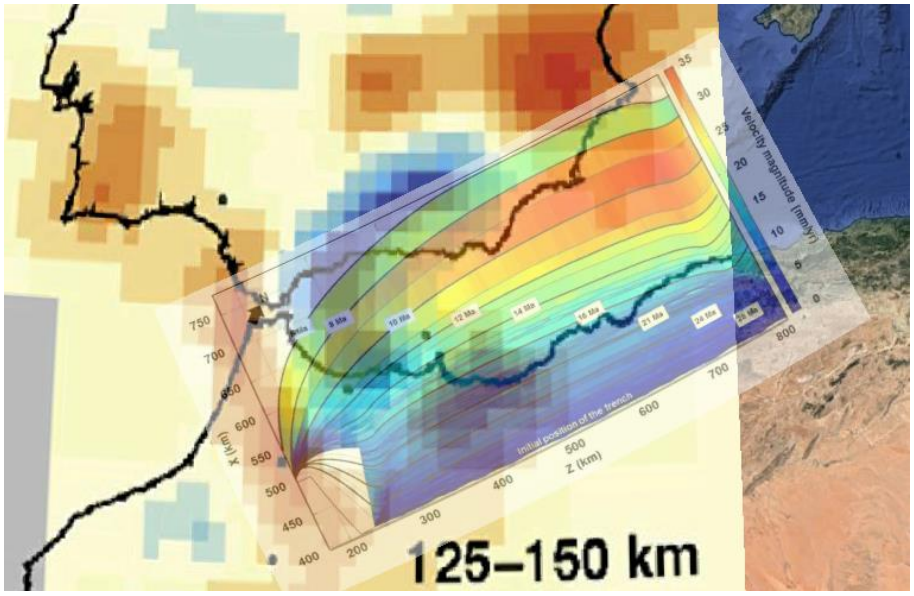

Figure 7.2 Trench evolution of the Alboran-Tethys (Figure 6.12) superimposed on tomographic image between 125 and 150 km depth of the Westernmost Mediterranean region from [*Villaseñor et al.*, 2015]

Figure 7.3 shows the calculated evolution of the trench position and the corresponding retreat velocities superposed on the geological map of the region. Maximum retreat velocities are located to the north-eastern Alboran Basin and the transition towards the Algerian Basin changing their orientation from NW to W in the western-central Alboran Basin since 12 Ma to present. This change of orientation of the retreat velocities are in agreement with the direction of tectonic transport reported by *Gómez de la Peña et al.* [2016] from multichannel seismic (MCS) profiles. Maximum retreat velocities occur between 12-8 Ma coinciding with volcanic manifestations in the SE-Iberian margin and the central-eastern regions of the Alboran Basin. This volcanism spreads over most of the Alboran Basin crust as evidenced by recent seismic MCS data [e.g., *Gómez de la Peña et al*., 2018].

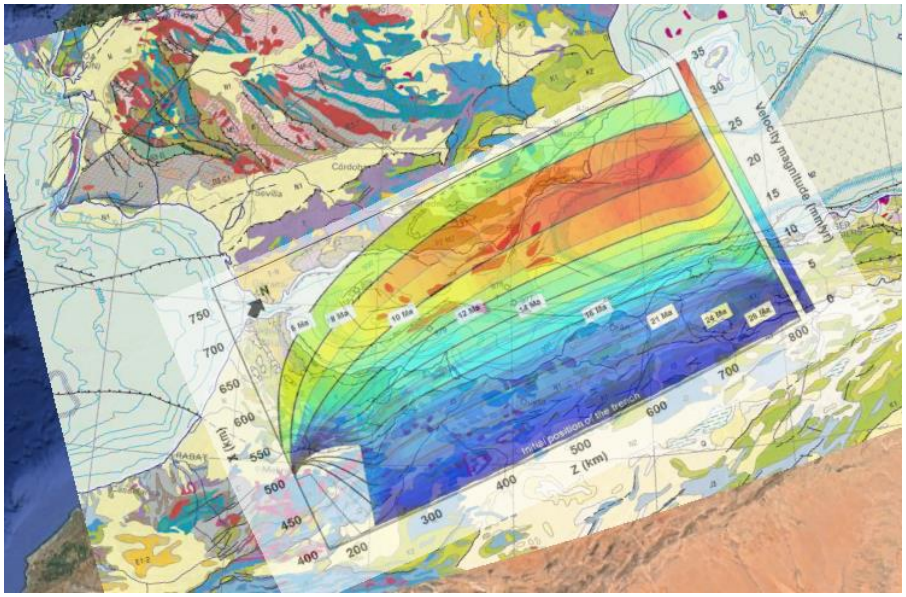

Figure 7.3 Trench evolution of the Alboran-Tethys (Figure 6.12) superimposed on the geological map of the Westernmost Mediterranean region (CCGM, 2016).

The volcanic geochemical signature in the Western Mediterranean varies from early Oligocene tholeiitic magmatic manifestations of the Malaga dykes, to Late Miocene-Quaternary calc-alkaline / HK calc-alkaline and alkaline magmas. This complexity is related to recycling and depletion of rocks due to subduction and rifting events operating in the region and therefore, the geochemistry of volcanic products do not always correspond to the present-day geodynamic setting in which they are sampled [e.g., *Lustrino and Wilson*, 2007; *Lustrino et al*., 2011*; Carminati et al*., 2012; *Melchiorre et al*., 2017]. *Melchiorre et al.* [2017] related the age, location, and type of the widespread

volcanism in the Western Mediterranean to the different evolutionary stages proposed by *Vergés and Fernàndez* [2012].

Subduction and related mantle flow produce changes in the rock fabric that results in a complex seismic anisotropy pattern that depends on depth, amount of subduction, slab geometry, trench displacement, and consequent mantle flow [e.g., *Faccenda and Capitanio*, 2013; *Di Leo et al*., 2014]. SKS based anisotropy onshore shows a clear alignment of the fast polarization directions (FPD) along strike of most of the Betic-Rif chain [*Díaz et al.*, 2015]. Though there are hardly any offshore anisotropy data, a common observation is the pronounced change of FPD from the Alboran Basin to the Algerian Basin. 3D azimuthally anisotropic model of Europe show FPD orientations changing from WSW-ENE in the Alboran Basin to NW-SE in the Algerian Basin at 70- 200 km depth [*Zhu and Tromp*, 2013; see their Figures 1 and S3]. In contrast, uppermost mantle anisotropy derived from Pn and Sn tomography shows distinct and almost perpendicular FPD patterns with a prominent NW-SE orientation in the southern margin of the Alboran Basin changing to NE-SW in the Algerian Basin [*Díaz et al.*, 2013; see their Figure 9]. These spatial and vertical anisotropy variations can be explained as the result of the complex interaction between the return flows associated with the opposite retreat of a double subduction system together with the northwest to west tectonic transport of the Betic-Rif units.

It must be said however that the great variety of magmatic compositions and their spatial distribution, as well as the limited availability of offshore anisotropy observations, allow for alternative geodynamic interpretations [e.g., *Faccenna et al*., 2004; *Spakman and Wortel*, 2004; *Duggen et al*., 2005; *Chertova et al*., 2014; *Van Hinsbergen et al*., 2014]. Among them, only the work by *Chertova et al.* [2014] is based on a 3D dynamic numerical model. These authors performed a numerical test suggesting that the most feasible model starts with a single northwest dipping subduction confined to the Balearic margin. These authors employ thermomechanical modelling of 3D subduction evolution to test three different tectonic evolution scenarios including the one studied here (Figure 6.2). Unlike the model presented in this thesis, only a single subduction zone under Africa starting from southeast dipping direction is considered by *Chertova et al*. [2014] when reproducing the model evolution of *Vergés and Fernàndez* [2012]. Moreover, the imposed initial geometry of the Alboran slab slightly differs from the presented in this work, considering an initial slab length of ~300 km and the trench starting at the north African margin ~300 km to the east from the actual Moroccan Rif. Despite their imposed limitations, they conclude that an initial southeast dipping subduction under the North

African margin is close to explain the present-day slab structure. Indeed, they managed to model the curved orientation of the Gibraltar arc being the upper part of the slab consistent with tomographic observations but they could not reproduce the deeper slab structure of the slab. It has to take into account that the range of variables of rheology, margin attributes and initial slab geometries tested by these authors where higher for their preferred model. Their preferred model, however, still requires the existence of several key tectonic structures to explain the slab rotation by more than 180°, the large westward displacement of the trench (> 600 km) and an average trench retreat velocity of 37.5 mm/yr over the last 16 Myr. This model, moreover, disregard the effects of shortening in the south-Iberian margin associated with the Betics Mountains building [*Fernàndez et al.*, 2019].

7.4 Final considerations

Experimental studies that use the combined analog and numerical techniques provide a broader overview of the different parameters characterizing the system under study. In particular, this thesis highlights the importance of using both methods to study subduction systems with opposite polarity in adjacent segments. Despite the differences observed through both methodologies, the final conclusions gain more strength while also provides novel insights on subduction modeling. As mentioned in Chapter 5, reproducing laboratory experiments by numerical modeling is not straightforward but it has allowed me to understand and select the most important parameters that characterize the double polarity subduction process and to perform in a more efficient way the numerical model of double polarity subduction applied to the Westernmost Mediterranean region.

In nature, the presence of several slabs, their reduced dimensions and the advancing or retreating trench migration velocities can produce changes in the stress, strain rate, pressure and temperature conditions in the mantle modifying the lattice preferred orientation of olivine crystals and therefore, the seismic anisotropy as manifested by shear-wave splitting. Similarly, the incorporation of sediments and hydrous fluids into the sub-lithospheric mantle during subduction and the rise of the asthenosphere through slab tears or in the backarc extensional basins can result in volcanic activity with a variety of geochemical signatures [e.g., *Lustrino et al.*, 2011; *Melchiorre et al.*, 2017].

Natural prototypes where double subduction systems with opposite polarity in adjacent segments have been proposed to occur coincide with regions under tectonic

convergence characterized by significant margin segmentation (e.g., Taiwan, *Lallemand et al.* [2001]; New Zealand, *Lamb* [2011]; the Western Mediterranean, *Vergés and Fernàndez* [2012]; the Alps-Apennine junction, *Vignaroli et al.* [2008]). However, extracting conclusions applicable to these natural scenarios is difficult as the presented study is based on oversimplified models of double subduction systems. Main limitations are the lack of overriding plates, the assumption of a viscous rheology for the lithosphere and upper mantle, and the simplified geometry of the system.

Despite these limitations, it can be conjectured on some expected observations derived from the complex interaction between the plates and the upper mantle. The time evolution of the effective stress at intermediate upper mantle depths observed on the numerical models (Figure 5.9) indicates that shear deformation in the mantle is distributed asymmetrically around the subducting slabs being maximum during the trench intersection. These changes of the deformation loci with time and depth together with the changes in the induced mantle flow would promote a complex seismic anisotropy pattern as observed for instance in Indonesia [*Di Leo et al.*, 2012] and the Western Mediterranean [*Díaz et al.*, 2013; *Zhu and Tromp*, 2013].

The vertical component of mantle flow shows maximum velocities in the back-arc and the inter-plate regions being more active while trenches approach (Figures 5.8 and S2-S5). This mantle upwelling from the deeper parts of the upper mantle can produce widespread melting by adiabatic decompression with variable composition depending on the water content and the depletion degree of the mantle source, which changes spatially with the retreating of slabs as proposed from recent 3D numerical modeling [e.g., *Magni*, 2019] and observed in Western Mediterranean [e.g., *Carminati et al.*, 2012; *Lustrino and Wilson*, 2007; *Lustrino et al.*, 2011; *Melchiorre et al.*, 2017].

A characteristic feature of some of the regions where double polarity subduction is observed, is the strong trench asymmetry with a tight curvature in one of the ends of the trench (e.g., Western Alps, Western Betics-Rif, southwest Ryuku trench, etc.). Analog and numerical results presented here (Chapters 4 and 5) show that the stress propagation associated with the interaction between plates produces a noticeable trench asymmetry. Moreover, the Alps-Apennines system has been analyzed by [*Király et al.*, 2016] proposing that the stress propagation and mantle flow associated with the interaction between the near retreating Tethyan plate segments likely contributed to the late stages of curvature of the Western Alps and to the slab breakoff. Likewise, the opposite dipping Ryukyu-Manila trenches in the Western Pacific would also be affected by the stress interaction

causing the strong curvature of the SW-Ryukyu trench [*Király et al.*, 2016]. A complex mantle flow resulting from the interaction of subducting plates with different polarities is derived from numerical modeling [*Lin and Kuo*, 2016], which is compatible with the tectonic and seismic anisotropy observations in this region.

Opposite subduction polarities are also present in New Zealand between the Tonga-Kermadec trench dipping to the west beneath the North Island, and the Puysegur trench dipping to the east beneath the South Island. The Hikurangi Trough, corresponding to the subduction of the Pacific Plate beneath the North Island, shows a strong curvature and coincides with a fast clockwise rotation of the North Island [*Wallace et al.*, 2004]. However, the effect of the interaction between both slabs is more elusive since they are separated at a critical distance of 500-600 km by the right-lateral transpressive Alpine Fault. Furthermore, the subduction in the Northern Island has initiated 25 Ma, whereas in South Island it has started 10-12 Ma [*King*, 2000]. Indeed, *Wallace et al.* [2009] suggest that the Hikurangi Trough curvature is produced by the collision of the Chatham Rise microplate on the Pacific Plate with the northern South Island.

CHAPTER 8

Conclusions

Chapter 8

Conclusions

In this thesis, the dynamics of subduction systems with opposite polarity in adjacent segments has been studied through two methodologies: analog and numerical modeling. The basics of the interaction between the two subducting plates observed by both methodologies provides relevant clues to better understand the tectonic evolution of natural scenarios. Reproducing numerically previous laboratory experiments of subduction systems allows comparing both methods and improving the techniques used. In addition, the application of a double polarity subduction system in the tectonic scenario of the Westernmost Mediterranean region supports the geodynamic model proposed by *Vergés and Fernàndez* [2012] to explain the formation and evolution of this region. In this chapter, I summarize the main conclusions deduced from this thesis according to the different chapters: i) Analog experiments of subduction systems with opposite polarity in adjacent segments (Chapter 4), ii) Reproducing analog experiments of subduction systems with numerical modeling (Chapter 5) and iii) The Alboran and Algerian basins (Westernmost Mediterranean), a case study of double subduction with opposite polarity in adjacent segments (Chapter 6). Finally, possible future works related to this thesis are proposed.

Analog experiments of subduction systems with opposite polarity in adjacent segments

In the first part of this thesis (Chapter 4), a number of laboratory experiments have been designed to better understand the dynamics of the plate/mantle interactions in a double subduction system with opposite polarity in adjacent segments. In particular, I

have tested the influence of the plate width and the initial separation between plates focusing the analysis on plate deformation described in terms of the evolution of trench retreat velocity and trench curvature, as well as on the variations in the lateral distance between the two plates and the induced mantle flow. From the laboratory experiments presented here I conclude that:

- The mantle flow induced by both plates shows an asymmetrical pattern around both trenches preventing a steady state phase of the subduction process to occur. Variations of observed rollback velocities and plate separation strongly correlate with the evolution of the toroidal cells around the inner edges of the trenches.

- The critical initial plate separation beyond which the interaction between the two slabs vanishes is about 10 cm in the experiments, or ~600 km in nature, thus confirming previous numerical results.

- For initial plate separations smaller than the critical distance, trench retreat velocities increase while trenches approach and decrease while trenches diverge, reaching a maximum velocity when trenches align to each other. The velocity variation is proportional to the width of the plates.

- The trench curvature increases linearly with time in all models. This trend line, which depends on the viscosity ratio and the return mantle flow balance, is independent of the width of the plates and of the initial plate separation.

Reproducing analog experiments of subduction systems with numerical modeling

In the second part of this thesis (Chapter 5), 3D numerical models, properly benchmarked with previous analog experiments, have been conducted with the aim of quantifying the physical processes characterizing the evolution of a subduction system with opposite polarity in adjacent plate segments. Numerical tests have been carried out to better understand the effects of boundary conditions, rheology and plate thickness. From these models I conclude:

- Numerical results show that varying the box size does not affect noticeably the evolution of the systems. This implies that the applied box domain of numerical models and/or analog experiments, using the same plate dimensions as described in this work,

may be reduced up to 80 x 80 cm^2 to increase the numerical model resolution or simplify the laboratory setup. Smaller box sizes (40 x 30 cm^2) can be sensitive to the lateral boundary conditions.

- Experimental uncertainties in the analog model setup (thinning of the plate or a non-perfectly Newtonian behavior of materials) may cause a more pronounced trench curvature, especially in wide plates, which is not well reproduced in numerical models.

- Numerical models of double polarity subduction show that the mantle flow induced by both plates produces that plates move closer to each other. Slabs and trenches deform asymmetrically as a consequence of the interaction between plates and mantle flow slowing down the subduction process relative to a single plate model.

- The interaction between the induced mantle flows in the inter-plate region generates a stress coupling in the mantle that increases during the relative approach of trenches and decreases when they diverge, producing additional deformation along the plate edges.

The Alboran and Algerian basins (Westernmost Mediterranean). A case study of double subduction with opposite polarity in adjacent segments

Finally, in Chapter 6 a 3D dynamic numerical model of double subduction with opposite polarity in adjacent plate segments has been developed simulating the tectonic setting of the Westernmost Mediterranean with the aim of reproducing the evolution of the Alboran-Tethys slab and studying the influence of an adjacent plate subducting in opposite direction. From the results presented in Chapter 6 the following conclusions have been achieved:

- The retreating of the Alboran-Tethys segment shows slower velocities (v_{rmax}= 35 mm/yr) than the Algerian-Tethys segment (v_{rmax}= 68 mm/yr) due to the combined effect of retreat consumption and asymmetry of the boundary conditions.

- The Alboran-Tethys segment shows a first phase spanning from 35 - 22 Ma in which the retreating velocities do not exceed the Africa-Iberia convergence velocity (7.7 mm/yr). This fact dates the initiation of the back-arc extension of the Alboran Basin 22 Ma, as estimated from geological data.

- The arcuate shape of the Alboran-Tethys slab is produced by a faster retreat of the eastern side of the plate segment being more relevant at 12-8 Ma. This asymmetry is governed by the continuity of the Alboran-Tethys segment with the Atlantic ocean to the west and the segmentation of the African margin.

- The presence of the adjacent Algerian-Tethys segment is needed to relate the numerical results with geological data. The interaction between the two retreating plate segments generates an asymmetrical mantle flow pattern around both trenches slowing down the retreating of the Alboran-Tethys segment and producing a less pronounced curvature.

Future work

The results presented in this thesis show that the basics of the interaction between two subducting plates with opposite polarity in adjacent segments provide relevant clues to better understand the tectonic evolution of natural scenarios as the Westernmost Mediterranean. Moreover, it highlights the importance of studying a certain geodynamic process using analog and numerical methods.

Analog and numerical experiments of subduction systems show a good similarity but the differences observed suggest that more detailed studies about the material properties and ambient conditions of the laboratory are needed. A direct numerical and analog benchmark of double polarity subduction, i.e. performing both experiments simultaneously, could help us to understand and quantify these differences.

Moreover, further improvements can be added to the numerical model of the Westernmost Mediterranean in order to obtain a more detailed study of the double polarity subduction process in this region. For example:

i) The use of more realistic geometries.

ii) The incorporation of overriding and side plates.

iii) The implementation of the thermal energy balance.

iv) The simulation of the convergence between Africa and Iberia.

These factors are nowadays feasible to be introduced although their implementations are not straightforward and will require a much greater computing capacity.

Appendix

Summary in Spanish

Resumen

El objetivo de esta tesis consiste en estudiar la dinámica de sistemas de doble subducción con polaridad opuesta en segmentos adyacentes. La ausencia de estudios previos sobre el análisis de la evolución geodinámica de estos sistemas ha definido la estrategia de investigación del presente trabajo. En consecuencia, esta tesis consta de tres partes diferenciadas que combinan tanto experimentos análogos como modelos numéricos de sistemas de doble subducción y su posterior aplicación a la región del Mediterráneo occidental, donde se ha propuesto un sistema de doble subducción con polaridad opuesta en segmentos adyacentes para explicar su formación y evolución.

Parte 1. Experimentos análogos de sistemas de subducción con polaridad opuesta en segmentos adyacentes

La primera parte de esta tesis consiste en analizar la dinámica de los sistemas de doble subducción con polaridad opuesta en segmentos litosféricos adyacentes mediante experimentos análogos. Estos experimentos se han llevado a cabo en el Laboratorio de Tectónica Experimental en la Universidad de Roma Tre durante una estancia de dos meses en Roma (Italia) bajo la supervisión de la Prof. Dr. Francesca Funiciello y el Prof. Dr. Claudio Faccenna. Se han diseñado un total de dieciocho experimentos, incluyendo cuatro modelos de referencia de subducción simple (una placa). Estos experimentos consisten en una o dos placas elaboradas con silicona representando la litosfera y un tanque lleno de jarabe de glucosa representando el manto. Las placas se fijan en su borde posterior para imponer un comportamiento de retroceso de las fosas de subducción (*trench rollback*) y la subducción se inicia hundiendo manualmente el borde delantero de la placa. Se han diseñado diferentes configuraciones para probar la influencia en la evolución del sistema de la anchura de las placas y la separación inicial entre ellas. Los resultados muestran que el flujo del manto inducido por ambas placas es asimétrico con respecto al eje de cada placa. Esto provoca una fusión progresiva de las celdas toroidales impidiendo una fase de estabilización del proceso de subducción y generando una fuerza de arrastre neta que tiende a separar las placas. Las velocidades de retroceso de las fosas (velocidad de subducción) dependen de la posición relativa de éstas, aumentando cuando

las fosas se acercan entre sí y disminuyendo cuando éstas se separan después de su alineación.

Parte 2. Reproducción de experimentos análogos de sistemas de subducción mediante modelos numéricos

En segundo lugar, se han realizado una serie de modelos numéricos, basados en los experimentos análogos realizados en la primera parte con el objetivo de comparar y complementar los resultados anteriores así como cuantificar los parámetros físicos más relevantes que caracterizan a un sistema de doble subducción con polaridad opuesta. En total, se han realizado alrededor de treinta y cinco modelos numéricos, además de las pruebas preliminares, aunque en esta tesis sólo se presentan quince de ellos mostrando los resultados más relevantes. Los modelos numéricos se han calculado principalmente en los supercomputadores *MARENOSTRUM 4* (Centro de Supercomputación de Barcelona, España) y *BRUTUS* (Instituto Federal Suizo de Tecnología, Suiza), con un tiempo de cálculo promedio de 3 semanas por modelo. La configuración numérica 3D se elige con parámetros de geometría, dimensiones y materiales similares a los modelos análogos de subducción realizados anteriormente. Éstos consisten en una o dos placas viscosas que subducen en el manto superior en direcciones opuestas. Las placas están fijadas en su borde posterior imponiendo un comportamiento de retroceso de la fosa durante la subducción. La subducción se produce debido a la diferencia de densidades entre la placa y el manto a partir de una pequeña subducción impuesta inicialmente. En primer lugar, se estudian el tamaño del dominio computacional, las condiciones de contorno, la reología y el grosor de las placas para encontrar el modelo numérico que mejor representa el experimento análogo. En segundo lugar, se estudian los parámetros más relevantes que controlan el proceso de doble subducción con polaridad opuesta mediante técnicas numéricas. Los resultados muestran que las condiciones de contorno del modelo numérico más adecuadas para reproducir los experimentos análogos son el deslizamiento libre en las paredes laterales del dominio computacional y el deslizamiento nulo en la pared inferior. Las condiciones de contorno laterales sólo afectan a la evolución del sistema a distancias muy pequeñas, lo que permite una reducción del tamaño del dominio computacional en relación con el modelo análogo aumentando la resolución numérica y disminuyendo el tiempo de cálculo. De manera complementaria a los resultados observados en los experimentos análogos, los resultados numéricos muestran que el flujo inducido del manto genera un acoplamiento en la tensión entre las placas adyacentes, ralentizando el proceso de subducción. Así mismo, se produce un movimiento lateral

entre las placas en superficie y una deformación asimétrica de las porciones subducidas (*slabs*) y de las fosas.

Parte 3. Las cuencas de Alborán y Argelia (Mediterráneo occidental). Un caso de estudio de doble subducción con polaridad opuesta en segmentos adyacentes

Finalmente, se ha realizado un modelo numérico 3D de doble subducción con polaridad opuesta en segmentos litosféricos adyacentes simulando la configuración tectónica del Mediterráneo occidental. El modelo numérico reproduce la evolución del segmento de placa de Alborán-Tethys estudiando la influencia del segmento de placa adyacente de Argelia-Tethys. Se han realizado alrededor de cuarenta modelos numéricos variando parámetros físicos y geométricos, incluyendo los modelos numéricos preliminares. En esta tesis sólo se presentan el modelo final de doble subducción con polaridad opuesta y de subducción simple. Los modelos numéricos se han calculado en el supercomputador *MARENOSTRUM 4* (Centro de Supercomputación de Barcelona, España) con un tiempo de cálculo promedio de 4 semanas por modelo. El modelo consta de dos segmentos de placa oceánica con una reología viscoplástica que subducen en direcciones opuestas en el manto superior viscoso. El modelo se inicia hace 35 millones de años. En la región actual de la cuenca del Alborán, el segmento de placa de Alborán-Tethys subduce hacia el sureste con el borde posterior fijado al margen ibérico. Se incluye un segmento de placa continental africana en el lado oeste de esta placa. En la región actual de la cuenca argelina, el segmento de placa de Tell-Kabylies subduce hacia el noroeste y el borde posterior se fija al margen africano. El estado inicial del modelo considera la convergencia entre África e Iberia desde el temprano Cretácico hasta el tardío Eoceno imponiendo una subducción inicial de los segmentos de placa de 150 km. El posterior proceso de subducción es impulsado por la inestabilidad de Rayleigh-Taylor. Además, se ha realizado un modelo de referencia de placa simple que incluye sólo el segmento de Alborán-Tethys para estudiar la influencia del segmento adyacente subduciendo en dirección opuesta. Los resultados muestran que la curvatura progresiva de la placa de Alborán-Tethys se debe a la falta de una zona de transformación en su conexión con el océano Atlántico al oeste y la gran segmentación del margen africano. Esto produce unas velocidades de retroceso de la fosa mayores en el lado este de la placa de Alborán-Tethys que en el lado occidental, donde una zona de transformación la separa del segmento de Argelia-Tethys. El cálculo de las velocidades de retroceso de las fosas de ambos segmentos de placa concluyen que la apertura de la cuenca de Alborán se produjo aproximadamente hace 22 millones de años.

La influencia del segmento argelino adyacente genera un patrón de flujo asimétrico alrededor de ambas fosas que ralentiza el proceso de subducción general del segmento de la placa de Alborán-Tethys.

List of Figures and Tables

List of Figures and Tables

References

References

Andrieux, J., J. M. Fontbote, and M. Mattauer (1971), Sur un modele explicatif de l'arc de Gibraltar, Earth and Planetary Science Letters, 12(2), 191-198.

Baumgardner, J. R. (1985), Three-dimensional treatment of convective flow in the earth's mantle, Journal of Statistical Physics, 39(5-6), 501-511.

Becker, T. W., C. Faccenna, R. J. O'Connell, and D. Giardini (1999), The development of slabs in the upper mantle: Insights from numerical and laboratory experiments, Journal of Geophysical Research: Solid Earth, 104(B7), 15207-15226.

Bellahsen, N., C. Faccenna, and F. Funiciello (2005), Dynamics of subduction and plate motion in laboratory experiments: Insights into the "plate tectonics" behavior of the Earth, Journal of Geophysical Research B: Solid Earth, 110(1), 1-15.

Berástegui, X., C. J. Banks, C. Puig, C. Taberner, D. Waltham, and M. Fernàndez (1998), Lateral diapiric emplacement of Triassic evaporites at the southern margin of the Guadalquivir Basin, Spain, in Geological Society Special Publication, edited, pp. 49-68.

Bevis, M., et al. (1995), Geodetic observations of very rapid convergence and back-arc extension at the tonga arc, Nature, 374(6519), 249-251.

Billen, M. I. (2008), Modeling the dynamics of subducting slabs, in Annual Review of Earth and Planetary Sciences, edited, pp. 325-356.

Booth-Rea, G., C. R. Ranero, I. Grevemeyer, and J. M. Martínez-Martínez (2007), Crustal types and tertiary tectonic evolution of the Alborán sea, western Mediterranean, Geochemistry, Geophysics, Geosystems, 8(10).

Boutelier, D., and O. Oncken (2011), 3-D thermo-mechanical laboratory modeling of plate-tectonics: Modeling scheme, technique and first experiments, Solid Earth, 2(1), 35-51.

Boutelier, D., and A. Cruden (2013), Slab rollback rate and trench curvature controlled by arc deformation, Geology, 41(8), 911-914.

Boutelier, D., A. Chemenda, and J. P. Burg (2003), Subduction versus accretion of intra-oceanic volcanic arcs: Insight from thermo-mechanical analogue experiments, Earth and Planetary Science Letters, 212(1-2), 31-45.

Brace, W., and D. Kohlstedt (1980), Limits on lithospheric stress imposed by laboratory experiments, 6248-6252 pp.

Bunge, H. P., M. A. Richards, and J. R. Baumgardner (1997), A sensitivity study of three-dimensional spherical mantle convection at 108 Rayleigh number: Effects of depth-dependent viscosity, heating mode, and an endothermic phase change, Journal of Geophysical Research B: Solid Earth, 102(6), 11991-12007.

Burg, J. P., O. Jagoutz, H. Dawood, and S. Shahid Hussain (2006), Precollision tilt of crustal blocks in rifted island arcs: Structural evidence from the Kohistan Arc, Tectonics, 25(5).

Buttles, J., and P. Olson (1998), A laboratory model of subduction zone anisotropy, Earth and Planetary Science Letters, 164(1-2), 245-262.

Calvert, A., E. Sandvol, D. Seber, M. Barazangi, S. Roecker, T. Mourabit, F. Vidal, G. Alguacil, and N. Jabour (2000), Geodynamic evolution of the lithosphere and upper mantle beneath the Alboran region of the western Mediterranean: Constraints from travel time tomography, Journal of Geophysical Research: Solid Earth, 105(B5), 10871-10898.

Capitanio, F. A. (2014), The dynamics of extrusion tectonics: Insights from numerical modeling, Tectonics, 33(12), 2361-2381.

Capitanio, F. A., G. Morra, and S. Goes (2007), Dynamic models of downgoing plate-buoyancy driven subduction: Subduction motions and energy dissipation, Earth and Planetary Science Letters, 262(1-2), 284-297.

Capitanio, F. A., A. Replumaz, and N. Riel (2015), Reconciling subduction dynamics during Tethys closure with large-scale Asian tectonics: Insights from numerical modeling, Geochemistry, Geophysics, Geosystems, 16(3), 962-982.

Carlson, R. L., T. W. C. Hilde, and S. Uyeda (1983), The driving mechanism of plate tectonics: Relation to age of the lithosphere at trenches, Geophysical Research Letters, 10(4), 297-300.

Carminati, E., M. Lustrino, and C. Doglioni (2012), Geodynamic evolution of the central and western Mediterranean: Tectonics vs. igneous petrology constraints, Tectonophysics, 579, 173-192.

Carminati, E., M. J. R. Wortel, W. Spakman, and R. Sabadini (1998), The role of slab detachment processes in the opening of the western-central Mediterranean basins: Some

geological and geophysical evidence, Earth and Planetary Science Letters, 160(3-4), 651-665.

Casciello, E., M. Fernàndez, J. Vergés, M. Cesarano, and M. Torne (2015), The Alboran domain in the western Mediterranean evolution: The birth of a concept, Bulletin de la Societe Geologique de France, 186(4-5), 371-384.

Čížková, H., and C. R. Bina (2015), Geodynamics of trench advance: Insights from a Philippine-Sea-style geometry, Earth and Planetary Science Letters, 430, 408-415.

Cloos, M. (1993), Lithospheric buoyancy and collisional orogenesis: subduction of oceanic plateaus, continental margins, island arcs, spreading ridges, and seamounts, Geological Society of America Bulletin, 105(6), 715-737.

Comas, M. C., J. P. Platt, J. I. Soto, and A. B. Watts (1999), The origin and tectonic history of the Alboran Basin: Insights from Leg 161 results, Proceedings of the Ocean Drilling Program: Scientific Results, 161, 555-580.

Conrad, C. P., and B. H. Hager (1999), Effects of plate bending and fault strength at subduction zones on plate dynamics, Journal of Geophysical Research: Solid Earth, 104(B8), 17551-17571.

Cruciani, C., E. Carminati, and C. Doglioni (2005), Slab dip vs. lithosphere age: No direct function, Earth and Planetary Science Letters, 238(3-4), 298-310.

Chapple, W. M., and T. E. Tullis (1977), Evaluation of the forces that drive the plates, Journal of Geophysical Research (1896-1977), 82(14), 1967-1984.

Chemenda, A., S. Lallemand, and A. Bokun (2000), Strain partitioning and interplate friction in oblique subduction zones: Constraints provided by experimental modeling, Journal of Geophysical Research: Solid Earth, 105(B3), 5567-5581.

Chen, Z., W. P. Schellart, V. Strak, and J. C. Duarte (2016), Does subduction-induced mantle flow drive backarc extension?, Earth and Planetary Science Letters, 441, 200-210.

Chertova, M. V., W. Spakman, T. Geenen, A. P. Van Den Berg, and D. J. J. Van Hinsbergen (2014), Underpinning tectonic reconstructions of the western Mediterranean region with dynamic slab evolution from 3-D numerical modeling, Journal of Geophysical Research: Solid Earth, 119(7), 5876-5902.

Christensen, U. R. (1996), The influence of trench migration on slab penetration into the lower mantle, Earth and Planetary Science Letters, 140(1-4), 27-39.

Davies, G. F. (1995), Penetration of plates and plumes through the mantle transition zone, Earth and Planetary Science Letters, 133(3-4), 507-516.

Davies, G. F., and M. A. Richards (1992), Mantle convection, Journal of Geology, 100(2), 151-206.

Davy, P., and P. R. Cobbold (1991), Experiments on shortening of a 4-layer model of the continental lithosphere, Tectonophysics, 188(1-2), 1-25.

Di Leo, J. F., A. M. Walker, Z. H. Li, J. Wookey, N. M. Ribe, J. M. Kendall, and A. Tommasi (2014), Development of texture and seismic anisotropy during the onset of subduction, Geochemistry, Geophysics, Geosystems, 15(1), 192-212.

Di Leo, J. F., J. Wookey, J. O. S. Hammond, J. M. Kendall, S. Kaneshima, H. Inoue, T. Yamashina, and P. Harjadi (2012), Mantle flow in regions of complex tectonics: Insights from Indonesia, Geochemistry, Geophysics, Geosystems, 13(12).

Díaz, J., and J. Gallart (2014), Seismic anisotropy from the Variscan core of Iberia to the Western African Craton: New constrains on upper mantle flow at regional scales, Earth and Planetary Science Letters, 394, 48-57.

Díaz, J., A. Gil, and J. Gallart (2013), Uppermost mantle seismic velocity and anisotropy in the euro-mediterranean region from pn and sn tomography, Geophysical Journal International, 192(1), 310-325.

Díaz, J., J. Gallart, I. Morais, G. Silveira, D. Pedreira, J. A. Pulgar, N. A. Dias, M. Ruiz, and J. M. González-Cortina (2015), From the Bay of Biscay to the High Atlas: Completing the anisotropic characterization of the upper mantle beneath the westernmost Mediterranean region, Tectonophysics, 663.

Do Couto, D., C. Gorini, L. Jolivet, N. Lebret, R. Augier, C. Gumiaux, E. d'Acremont, A. Ammar, H. Jabour, and J. L. Auxietre (2016), Tectonic and stratigraphic evolution of the Western Alboran Sea Basin in the last 25 Myrs, Tectonophysics, 677-678, 280-311.

Doblas, M., J. López-Ruiz, and J. M. Cebriá (2007), Cenozoic evolution of the Alboran Domain: A review of the tectonomagmatic models, in Special Paper of the Geological Society of America, edited, pp. 303-320.

Donea, J., and Huerta, A., Finite Element Methods for Flow Problems, Wiley, Chichester, West Sussex PO198SQ, England (2002).

Druken, K. A., M. D. Long, and C. Kincaid (2011), Patterns in seismic anisotropy driven by rollback subduction beneath the High Lava Plains, Geophysical Research Letters, 38(13).

Druken, K. A., C. Kincaid, R. W. Griffiths, D. R. Stegman, and S. R. Hart (2014), Plume-slab interaction: The Samoa-Tonga system, Physics of the Earth and Planetary Interiors, 232, 1-14.

Duarte, J. C., W. P. Schellart, and A. R. Cruden (2013), Three-dimensional dynamic laboratory models of subduction with an overriding plate and variable interplate rheology, Geophysical Journal International, 195(1), 47-66.

Duggen, S., K. Hoernle, P. van den Bogaard, and C. Harris (2004), Magmatic evolution of the Alboran region: The role of subduction in forming the western Mediterranean and causing the Messinian Salinity Crisis, Earth and Planetary Science Letters, 218(1-2), 91-108.

Duggen, S., K. Hoernle, P. van den Bogaard, and D. Garbe-Schönberg (2005), Post-collisional transition from subduction-to intraplate-type magmatism in the westernmost Mediterranean: Evidence for continental-edge delamination of subcontinental lithosphere, Journal of Petrology, 46(6), 1155-1201.

Duggen, S., K. Hoernle, A. Klügel, J. Geldmacher, M. Thirlwall, F. Hauff, D. Lowry, and N. Oates (2008), Geochemical zonation of the Miocene Alborán Basin volcanism (westernmost Mediterranean): Geodynamic implications, Contributions to Mineralogy and Petrology, 156(5), 577-593.

Duretz, T., T. V. Gerya, B. J. P. Kaus, and T. B. Andersen (2012), Thermomechanical modeling of slab eduction, Journal of Geophysical Research: Solid Earth, 117(8).

Elsasser, W. M. (1971), Sea- floor spreading as thermal convection, J Geophys Res, 76(5), 1101-1112.

Faccenda, M., and F. A. Capitanio (2013), Seismic anisotropy around subduction zones: Insights from three-dimensional modeling of upper mantle deformation and SKS splitting calculations, Geochemistry, Geophysics, Geosystems, 14(1), 243-262.

References

Faccenna, C., and T. W. Becker (2010), Shaping mobile belts by small-scale convection, Nature, 465(7298), 602-605.

Faccenna, C., C. Piromallo, A. Crespo-Blanc, L. Jolivet, and F. Rossetti (2004), Lateral slab deformation and the origin of the western Mediterranean arcs, Tectonics, 23(1), TC1012 1011-1021.

Faccenna, C., T. W. Becker, M. S. Miller, E. Serpelloni, and S. D. Willett (2014a), Isostasy, dynamic topography, and the elevation of the Apennines of Italy, Earth and Planetary Science Letters, 407, 163-174.

Faccenna, C., T. W. Becker, S. Lallemand, Y. Lagabrielle, F. Funiciello, and C. Piromallo (2010), Subduction-triggered magmatic pulses: A new class of plumes?, Earth and Planetary Science Letters, 299(1-2), 54-68.

Faccenna, C., P. Davy, J. P. Brun, R. Funiciello, D. Giardini, M. Mattei, and T. Nalpas (1996), The dynamics of back-arc extension: An experimental approach to the opening of the Tyrrhenian Sea, Geophysical Journal International, 126(3), 781-795.

Faccenna, C., et al. (2014b), Mantle dynamics in the Mediterranean, Reviews of Geophysics, 52(3), 283-332.

Farrington, R. J., L. N. Moresi, and F. A. Capitanio (2014), The role of viscoelasticity in subducting plates, Geochemistry, Geophysics, Geosystems, 15(11), 4291-4304.

Fernàndez, M., M. Torne, J. Vergés, E. Casciello, and C. Macchiavelli (2019), Evidence of segmentation in the iberia–africa plate boundary: A jurassic heritage?, Geosciences (Switzerland), 9(8).

Fichtner, A., and A. Villaseñor (2015), Crust and upper mantle of the western Mediterranean - Constraints from full-waveform inversion, Earth and Planetary Science Letters, 428, 52-62.

Forsyth, D., and S. Uyedaf (1975), On the Relative Importance of the Driving Forces of Plate Motion, Geophysical Journal of the Royal Astronomical Society, 43(1), 163-200.

Frizon de Lamotte, D., C. Raulin, N. Mouchot, J.-C. Wrobel-Daveau, C. Blanpied, and J.-C. Ringenbach (2011), The southernmost margin of the Tethys realm during the Mesozoic and Cenozoic: Initial geometry and timing of the inversion processes, Tectonics, 30(3).

Funiciello, F., C. Faccenna, and D. Giardini (2004), Role of lateral mantle flow in the evolution of subduction systems: Insights from laboratory experiments, Geophysical Journal International, 157(3), 1393-1406.

Funiciello, F., C. Faccenna, D. Giardini, and K. Regenauer-Lieb (2003), Dynamics of retreating slabs: 2. Insights from three-dimensional laboratory experiments, Journal of Geophysical Research B: Solid Earth, 108(4), ETG 12-11 - 12-16.

Funiciello, F., M. Moroni, C. Piromallo, C. Faccenna, A. Cenedese, and H. A. Bui (2006), Mapping mantle flow during retreating subduction: Laboratory models analyzed by feature tracking, Journal of Geophysical Research: Solid Earth, 111(3).

Funiciello, F., C. Faccenna, A. Heuret, S. Lallemand, E. Di Giuseppe, and T. W. Becker (2008), Trench migration, net rotation and slab–mantle coupling, Earth and Planetary Science Letters, 271(1–4), 233-240.

García-Dueñas, V., J. C. Balanyá, and J. M. Martínez-Martínez (1992), Miocene extensional detachments in the outcropping basement of the northern Alboran Basin (Betics) and their tectonic implications, Geo-Marine Letters, 12(2-3), 88-95.

Garel, F., S. Goes, D. R. Davies, J. H. Davies, S. C. Kramer, and C. R. Wilson (2014), Interaction of subducted slabs with the mantle transition-zone: A regime diagram from 2-D thermo-mechanical models with a mobile trench and an overriding plate, Geochemistry, Geophysics, Geosystems, 15(5), 1739-1765.

Garfunkel, Z., C. A. Anderson, and G. Schubert (1986), Mantle circulation and the lateral migration of subducted slabs, Journal of Geophysical Research: Solid Earth, 91(B7), 7205-7223.

Gelabert, B., F. Sàbat, and A. Rodríguez-Perea (2002), A new proposal for the late Cenozoic geodynamic evolution of the western Mediterranean, Terra Nova, 14(2), 93-100.

Gerya (2009), Introduction to numerical geodynamic modelling, 1-345 pp.

Gerya, and Yuen (2007), Robust characteristics method for modelling multiphase visco-elasto-plastic thermo-mechanical problems, Physics of the Earth and Planetary Interiors, 163(1-4), 83-105.

Gómez de la Peña, L., C. R. Ranero, and E. Gràcia (2018), The Crustal Domains of the Alboran Basin (Western Mediterranean), Tectonics, 37(10), 3352-3377.

Gómez de la Peña, L., E. Gràcia, A. Muñoz, J. Acosta, M. Gómez-Ballesteros, C. Ranero, and E. Uchupi (2016), Geomorphology and Neogene tectonic evolution of the Palomares continental margin (Western Mediterranean), Tectonophysics, 689, 25-39.

Griffiths, R. W., R. I. Hackney, and R. D. van der Hilst (1995), A laboratory investigation of effects of trench migration on the descent of subducted slabs, Earth and Planetary Science Letters, 133(1-2), 1-17.

Grotenhuis, S. Piazolo, T. Pakula, C. W. Passchier, and P. D. Bons (2002), Are polymers suitable rock analogs?, Tectonophysics, 350(1), 35-47.

Gueguen, E., C. Doglioni, and M. Fernandez (1998), On the post-25 Ma geodynamic evolution of the western Mediterranean, Tectonophysics, 298(1-3), 259-269.

Guillaume, B., J. Martinod, and N. Espurt (2009), Variations of slab dip and overriding plate tectonics during subduction: Insights from analogue modelling, Tectonophysics, 463(1-4), 167-174.

Guillaume, B., L. Husson, F. Funiciello, and C. Faccenna (2013), The dynamics of laterally variable subductions: Laboratory models applied to the Hellenides, Solid Earth, 4(2), 179-200.

Guillaume, B., M. Moroni, F. Funiciello, J. Martinod, and C. Faccenna (2010), Mantle flow and dynamic topography associated with slab window opening: Insights from laboratory models, Tectonophysics, 496(1-4), 83-98.

Guillou-Frottier, L., J. Buttles, and P. Olson (1995), Laboratory experiments on the structure of subducted lithosphere, Earth and Planetary Science Letters, 133(1-2), 19-34.

Hall (1815), II. On the Vertical Position and Convolutions of certain Strata, and their relation with Granite, Transactions of the Royal Society of Edinburgh, 7(1), 79-108.

Hall, R. and Spakman, W. (2015), Mantle structure and tectonic history of SE Asia, Tectonophysics, 658, 14-45.

Handy, M. R., K. Ustaszewski, and E. Kissling (2014), Reconstructing the Alps–Carpathians–Dinarides as a key to understanding switches in subduction polarity, slab gaps and surface motion, International Journal of Earth Sciences, 104(1).

Handy, M. R., S. M. Schmid, R. Bousquet, E. Kissling, and D. Bernoulli (2010), Reconciling plate-tectonic reconstructions of Alpine Tethys with the geological-

geophysical record of spreading and subduction in the Alps, Earth-Science Reviews, 102(3-4), 121-158.

Harlow, F. H. (1955). A Machine Calculation Method for Hydrodynamic Problems, Los Alamos Scientific Laboratory, LAMS-1956, 94p, New Mexico.

Haskell, N. A. (1935), The motion of a viscous fluid under a surface load, Journal of Applied Physics, 6(8), 265-269.

Heuret, A., and S. Lallemand (2005), Plate motions, slab dynamics and back-arc deformation, Physics of the Earth and Planetary Interiors, 149(1-2 SPEC. ISS.), 31-51.

Holt, A. F., L. H. Royden, and T. W. Becker (2017), The dynamics of double slab subduction, Geophysical Journal International, 209(1), 250-265.

Hubbert, M. (1937), Theory of scale models as applied to the study of geologic structures, Bulletin of the Geological Society of America, 48(10), 1459-1520.

Hubbert, M. (1951), Mechanical basis for certain familiar geologic structures, Bulletin of the Geological Society of America, 62(4), 355-372.

Iribarren, L.; J. Vergés; F., Camurri; J. Fullea; M. Fernàndez. The structure of the Atlantic–Mediterranean transition zone from the Alboran Sea to the Horseshoe Abyssal Plain (Iberia–Africa plate boundary). Mar. Geol. 2007, 243, 97–119.

Jacoby, W. R. (1973), Model Experiment of Plate Movements, Nature Physical Science, 242(122), 130-134.

Jolivet, L., C. Faccenna, and C. Piromallo (2009), From mantle to crust: Stretching the Mediterranean, Earth and Planetary Science Letters, 285(1-2), 198-209.

Kincaid, C., and R. W. Griffiths (2003), Laboratory models of the thermal evolution of the mantle during rollback subduction, Nature, 425(6953), 58-62.

Kincaid, C., and R. W. Griffiths (2004), Variability in flow and temperatures within mantle subduction zones, Geochemistry, Geophysics, Geosystems, 5(6).

King, P. R. (2000), Tectonic reconstructions of New Zealand: 40 Ma to the Present, New Zealand Journal of Geology and Geophysics, 43(4), 611-638.

References

Király, Á., C. Faccenna, F. Funiciello, and A. Sembroni (2015), Coupling surface and mantle dynamics: A novel experimental approach, Geophysical Research Letters, 42(10), 3863-3869.

Király, Á., C. Faccenna, and F. Funiciello (2018a), Subduction Zones Interaction Around the Adria Microplate and the Origin of the Apenninic Arc, Tectonics, 37(10), 3941-3953.

Király, Á., F. A. Capitanio, F. Funiciello, and C. Faccenna (2016), Subduction zone interaction: Controls on arcuate belts, Geology, 44(9), 715-718.

Király, Á., F. A. Capitanio, F. Funiciello, and C. Faccenna (2017), Subduction induced mantle flow: Length-scales and orientation of the toroidal cell, Earth and Planetary Science Letters, 479, 284-297.

Király, Á., A. F. Holt, F. Funiciello, C. Faccenna, and F. A. Capitanio (2018b), Modeling Slab-Slab Interactions: Dynamics of Outward Dipping Double-Sided Subduction Systems, Geochemistry, Geophysics, Geosystems, 19(3), 693-714.

Kirdyashkin, A. A., and A. G. Kirdyashkin (2014), Forces acting on a subducting oceanic plate, Geotectonics, 48(1), 54-67.

Kufner, S. K., et al. (2016), Deep India meets deep Asia: Lithospheric indentation, delamination and break-off under Pamir and Hindu Kush (Central Asia), Earth and Planetary Science Letters, 435, 171-184.

Lallemand, and F. Funiciello (2009), Subduction Zone Geodynamics.

Lallemand, Y. Font, H. Bijwaard, and H. Kao (2001), New insights on 3-D plates interaction near Taiwan from tomography and tectonic implications, Tectonophysics, 335(3–4), 229-253.

Lallemand, A. Heuret, C. Faccenna, and F. Funiciello (2008), Subduction dynamics as revealed by trench migration, Tectonics, 27(3).

Lamb, S. (2011), Cenozoic tectonic evolution of the New Zealand plate-boundary zone: A paleomagnetic perspective, Tectonophysics, 509(3-4), 135-164.

Leprêtre, A., F. Klingelhoefer, D. Graindorge, P. Schnurle, M. O. Beslier, K. Yelles, J. Déverchère, and R. Bracene (2013), Multiphased tectonic evolution of the Central Algerian

margin from combined wide-angle and reflection seismic data off Tipaza, Algeria, Journal of Geophysical Research: Solid Earth, 118(8), 3899-3916.

Li, Z. H., and N. M. Ribe (2012), Dynamics of free subduction from 3-D boundary element modeling, Journal of Geophysical Research: Solid Earth, 117(6).

Liao, J., T. Gerya, M. Thielmann, A. A. G. Webb, S. K. Kufner, and A. Yin (2017), 3D geodynamic models for the development of opposing continental subduction zones: The Hindu Kush–Pamir example, Earth and Planetary Science Letters, 480, 133-146.

Lin, S. C., and B. Y. Kuo (2016), Dynamics of the opposite-verging subduction zones in the Taiwan region: Insights from numerical models, Journal of Geophysical Research: Solid Earth, 121(3), 2174-2192.

Loiselet, C., L. Husson, and J. Braun (2009), From longitudinal slab curvature to slab rheology, Geology, 37(8), 747-750.

Lonergan, L., and N. White (1997), Origin of the Betic-Rif mountain belt, Tectonics, 16(3), 504-522.

Long, M. D. (2016), The Cascadia Paradox: Mantle flow and slab fragmentation in the Cascadia subduction system, Journal of Geodynamics, 102, 151-170.

Long, M. D., and P. G. Silver (2008), The subduction zone flow field from seismic anisotropy: A global view, Science, 319(5861), 315-318.

Lustrino, M., and M. Wilson (2007), The circum-Mediterranean anorogenic Cenozoic igneous province, Earth-Science Reviews, 81(1-2), 1-65.

Lustrino, M., S. Duggen, and C. L. Rosenberg (2011), The Central-Western Mediterranean: Anomalous igneous activity in an anomalous collisional tectonic setting, Earth-Science Reviews, 104(1-3), 1-40.

Macchiavelli, C., J. Vergés, A. Schettino, M. Fernàndez, E. Turco, E. Casciello, M. Torne, P. P. Pierantoni, and L. Tunini (2017), A New Southern North Atlantic Isochron Map: Insights Into the Drift of the Iberian Plate Since the Late Cretaceous, Journal of Geophysical Research: Solid Earth, 122(12), 9603-9626.

MacDougall, J. G., C. Kincaid, S. Szwaja, and K. M. Fischer (2014), The impact of slab dip variations, gaps and rollback on mantle wedge flow: Insights from fluids experiments, Geophysical Journal International, 197(2), 705-730.

Machetel, P., M. Rabinowicz, and P. Bernardet (1986), Threedimensional convection in spherical shells, Geophysical & Astrophysical Fluid Dynamics, 37(1-2), 57-84.

Magni, V. (2019), The effects of back-arc spreading on arc magmatism, Earth and Planetary Science Letters, 519, 141-151.

Maldonado, A., A. C. Campillo, A. Mauffret, B. Alonso, J. Woodside, and J. Campos (1992), Alboran Sea late cenozoic tectonic and stratigraphic evolution, Geo-Marine Letters, 12(2-3), 179-186.

Martínez, F., P. Fryer, and N. Becker (2000), Geophysical characteristics of the southern Mariana Trough, 11°50′N-13°40′N, Journal of Geophysical Research: Solid Earth, 105(B7), 16591-16607.

Mason, W. G., L. Moresi, P. G. Betts, and M. S. Miller (2010), Three-dimensional numerical models of the influence of a buoyant oceanic plateau on subduction zones, Tectonophysics, 483(1-2), 71-79.

Mauffret, A., A. Ammar, C. Gorini, and H. Jabour (2007), The Alboran Sea (Western Mediterranean) revisited with a view from the Moroccan Margin, Terra Nova, 19(3), 195-203.

Mauffret, A., D. Frizon de Lamotte, S. Lallemant, C. Gorini, and A. Maillard (2004), E-W opening of the Algerian Basin (Western Mediterranean), Terra Nova, 16(5), 257-264.

McKenzie, D. (1977), Surface deformation, gravity anomalies and convection, Geophysical Journal of the Royal Astronomical Society, 48(2), 211-238.

Medaouri, M., J. Déverchère, D. Graindorge, R. Bracene, R. Badji, A. Ouabadi, K. Yelles-Chaouche, and F. Bendiab (2014), The transition from Alboran to Algerian basins (Western Mediterranean Sea): Chronostratigraphy, deep crustal structure and tectonic evolution at the rear of a narrow slab rollback system, Journal of Geodynamics, 77, 186-205.

Melchiorre, M., J. Vergés, M. Fernàndez, M. Coltorti, M. Torne, and E. Casciello (2017), Evidence for mantle heterogeneities in the westernmost Mediterranean from a statistical approach to volcanic petrology, Lithos, 276, 62-74.

Mériaux, C. A., D. A. May, J. Mansour, Z. Chen, and O. Kaluza (2018), Benchmark of three-dimensional numerical models of subduction against a laboratory experiment, Physics of the Earth and Planetary Interiors, 283, 110-121.

Meyer, C., and W. P. Schellart (2013), Three-dimensional dynamic models of subducting plate-overriding plate-upper mantle interaction, Journal of Geophysical Research: Solid Earth, 118(2), 775-790.

Minear, J. W., and M. N. Toksöz (1970), Thermal regime of a downgoing slab, Tectonophysics, 10(1-3), 367-390.

Mishin, Y. A., T. V. Gerya, J. P. Burg, and J. A. D. Connolly (2008), Dynamics of double subduction: Numerical modeling, Physics of the Earth and Planetary Interiors, 171(1-4), 280-295.

Moresi, L., F. Dufour, and H. B. Mühlhaus (2003), A Lagrangian integration point finite element method for large deformation modeling of viscoelastic geomaterials, Journal of Computational Physics, 184(2), 476-497.

Morra, G., K. Regenauer-Lieb, and D. Giardini (2006), Curvature of oceanic arcs, Geology, 34(10), 877-880.

Mullen, E. K., and D. Weis (2015), Evidence for trench-parallel mantle flow in the northern Cascade Arc from basalt geochemistry, Earth and Planetary Science Letters, 414, 100-107.

Oden, J. (1991), Finite elements: An introduction, in Handbook of Numerical Analysis, edited, pp. 3-15.

OzBench, M., et al. (2008), A model comparison study of large-scale mantle-lithosphere dynamics driven by subduction, Physics of the Earth and Planetary Interiors, 171(1-4), 224-234.

Palano, M., C. Piromallo, and C. Chiarabba (2017), Surface imprint of toroidal flow at retreating slab edges: The first geodetic evidence in the Calabrian subduction system, Geophysical Research Letters, 44(2), 845-853.

Panien, M., S. J. H. Buiter, G. Schreurs, and O. Pfiffner (2006), Inversion of a symmetric basin: Insights from a comparison between analogue and numerical experiments, 253-270 pp.

Patankar, S. V. (1980), Numerical heat transfer and fluid flow.

Peral, M., Á. Király, S. Zlotnik, F. Funiciello, M. Fernàndez, C. Faccenna, and J. Vergés (2018), Opposite Subduction Polarity in Adjacent Plate Segments, Tectonics, 37(9), 3285-3302.

Piromallo, C., T. W. Becker, F. Funiciello, and C. Faccenna (2006), Three-dimensional instantaneous mantle flow induced by subduction, Geophysical Research Letters, 33(8).

Platt, J. P., and R. L. M. Vissers (1989), Extensional collapse of thickened continental lithosphere: a working hypothesis for the Alboran Sea and Gibraltar arc, Geology, 17(6), 540-543.

Platt, J. P., W. M. Behr, K. Johanesen, and J. R. Williams (2013), The Betic-Rif arc and its orogenic hinterland: A review, in Annual Review of Earth and Planetary Sciences, edited, pp. 313-357.

Ramberg, H. (1967), Model Experimentation of the Effect of Gravity on Tectonic Processes, Geophysical Journal of the Royal Astronomical Society, 14(1-4), 307-329.

Ramberg, H. (1981), Gravity, deformation and the earth's crust. In theory, experiments and geological application, second edition, Gravity, deformation and the earth's crust. In theory, experiments and geological application, second edition.

Ranalli, G., and D. C. Murphy (1987), Rheological stratification of the lithosphere, Tectonophysics, 132(4), 281-295.

Ribe, N. M. (2010), Bending mechanics and mode selection in free subduction: A thin-sheet analysis, Geophysical Journal International, 180(2), 559-576.

Ribe, N. M., and A. Davaille (2013), Dynamical similarity and density (non-) proportionality in experimental tectonics, Tectonophysics, 608, 1371-1379.

Richard, P. (1991), Experiments on faulting in a two-layer cover sequence overlying a reactivated basement fault with oblique-slip, Journal of Structural Geology, 13(4), 459-469.

Rosenbaum, G., and G. S. Lister (2004), Formation of arcuate orogenic belts in the western Mediterranean region, in Special Paper of the Geological Society of America, edited, pp. 41-56.

Rosenbaum, G., G. S. Lister, and C. Duboz (2002), Reconstruction of the tectonic evolution of the western Mediterranean since the Oligocene, Journal of the Virtual Explorer, 8.

Royden, and Faccenna (2018), Subduction Orogeny and the Late Cenozoic Evolution of the Mediterranean Arcs, in Annual Review of Earth and Planetary Sciences, edited, pp. 261-289.

Royden, L. H. (1993), Evolution of retreating subduction boundaries formed during continental collision, Tectonics, 12(3), 629-638.

Ruh, J. B., L. Le Pourhiet, P. Agard, E. Burov, and T. Gerya (2015), Tectonic slicing of subducting oceanic crust along plate interfaces: Numerical modeling, Geochemistry, Geophysics, Geosystems, 16(10), 3505-3531.

Sàbat, F., Roca, E., Muñoz, J., Vergés, J., Santanach, P., Masana, E., et al. (1997). Role of extension and compression in the evolution of the eastern margin of Iberia: the ESCI-Valencia trough seismic profile. Rev. Soc. Geol. España (8), 431-448.

Schellart, W.P. (2004a), Kinematics of subduction and subduction-induced flow in the upper mantle, Journal of Geophysical Research B: Solid Earth, 109(7), B07401 07401-07419.

Schellart, W.P. (2004b), Quantifying the net slab pull force as a driving mechanism for plate tectonics, Geophysical Research Letters, 31(7), L07611 07611-07615.

Schellart, W.P. (2008), Kinematics and flow patterns in deep mantle and upper mantle subduction models: Influence of the mantle depth and slab to mantle viscosity ratio, Geochemistry, Geophysics, Geosystems, 9(3).

Schellart, W.P. (2010a), Evolution of subduction zone curvature and its dependence on the trench velocity and the slab to upper mantle viscosity ratio, Journal of Geophysical Research: Solid Earth, 115(11).

Schellart, W.P. (2010b), Mount Etna-Iblean volcanism caused by rollback-induced upper mantle upwelling around the Ionian slab edge: An alternative to the plume model, Geology, 38(8), 691-694.

Schellart, W.P. and L. Moresi (2013), A new driving mechanism for backarc extension and backarc shortening through slab sinking induced toroidal and poloidal mantle flow:

Results from dynamic subduction models with an overriding plate, Journal of Geophysical Research: Solid Earth, 118(6), 3221-3248.

Schellart, W.P., and V.A. Strak (2016), A review of analogue modelling of geodynamic processes: Approaches, scaling, materials and quantification, with an application to subduction experiments, Journal of Geodynamics, 100, 7-32.

Schellart, W.P., J. Freeman, D. Stegman, L. Moresi, and D. A. May (2007), Evolution and diversity of subduction zones controlled by slab width, 308-311 pp.

Schettino, A., and E. Turco (2011), Tectonic history of the Western Tethys since the Late Triassic, Bulletin of the Geological Society of America, 123(1-2), 89-105.

Schmeling, H., et al. (2008), A benchmark comparison of spontaneous subduction models-Towards a free surface, Physics of the Earth and Planetary Interiors, 171(1-4), 198-223.

Spakman, W., and M. Wortel (2004), A Tomographic View on Western Mediterranean Geodynamics, TRANSMED Atlas Mediterr. Reg. Crust Mantle.

Stegman, D.R., R. Farrington, F. A. Capitanio, and W. P. Schellart (2010), A regime diagram for subduction styles from 3-D numerical models of free subduction, Tectonophysics, 483(1-2), 29-45.

Stegman, D.R., J. Freeman, W. P. Schellart, L. Moresi, and D. May (2006), Influence of trench width on subduction hinge retreat rates in 3-D models of slab rollback, Geochemistry, Geophysics, Geosystems, 7(3).

Stephenson, R. A., and S. A. P. L. Cloetingh (1991), Some examples and mechanical aspects of continental lithospheric folding, Tectonophysics, 188(1-2), 27-37.

Stern, R. J. (2002), Subduction zones, Reviews of Geophysics, 40(4), 3-1 - 3-38.

Sternai, P., L. Jolivet, A. Menant, and T. Gerya (2014), Driving the upper plate surface deformation by slab rollback and mantle flow, Earth and Planetary Science Letters, 405, 110-118.

Strak, V., and W. P. Schellart (2014), Evolution of 3-D subduction-induced mantle flow around lateral slab edges in analogue models of free subduction analysed by stereoscopic particle image velocimetry technique, Earth and Planetary Science Letters, 403, 368-379.

Tackley, P. J. (2008), Modelling compressible mantle convection with large viscosity contrasts in a three-dimensional spherical shell using the yin-yang grid, Physics of the Earth and Planetary Interiors, 171(1-4), 7-18.

Tetzlaff, M., and H. Schmeling (2000), The influence of olivine metastability on deep subduction of oceanic lithosphere, Physics of the Earth and Planetary Interiors, 120(1), 29-38.

Thielicke, W., and E. Stamhuis (2014), PIVlab – Towards User-friendly, Affordable and Accurate Digital Particle Image Velocimetry in MATLAB, Journal of Open Research Software, 2.

Torne, M., M. Fernàndez, M. C. Comas, and J. I. Soto (2000), Lithospheric structure beneath the Alboran Basin: Results from 3D gravity modeling and tectonic relevance, Journal of Geophysical Research: Solid Earth, 105(B2), 3209-3228.

Turcotte, D. L. (1982), Geodynamics : applications of continuum physics to geological problems, J. Wiley, New York.

Van Hinsbergen, D. J. J., R. L. M. Vissers, and W. Spakman (2014), Origin and consequences of western Mediterranean subduction, rollback, and slab segmentation, Tectonics, 33(4), 393-419.

Vergés, J., and F. Sàbat (1999), Constraints on the Neogene Mediterranean kinematic evolution along a 1000 km transect from Iberia to Africa, Geological Society, London, Special Publications, 156(1), 63.

Vergés, J., and M. Fernàndez (2012), Tethys-Atlantic interaction along the Iberia-Africa plate boundary: The Betic-Rif orogenic system, Tectonophysics, 579, 144-172.

Vidal, N., J. Gallart, and J. J. Dañobeitia (1998), A deep seismic crustal transect from the NE Iberian Peninsula to the western Mediterranean, Journal of Geophysical Research: Solid Earth, 103(6), 12381-12396.

Vignaroli, G., C. Faccenna, L. Jolivet, C. Piromallo, and F. Rossetti (2008), Subduction polarity reversal at the junction between the Western Alps and the Northern Apennines, Italy, Tectonophysics, 450(1-4), 34-50.

Villaseñor, A., S. Chevrot, M. Harnafi, J. Gallart, A. Pazos, I. Serrano, D. Córdoba, J. A. Pulgar, and P. Ibarra (2015), Subduction and volcanism in the Iberia-North Africa collision zone from tomographic images of the upper mantle, Tectonophysics, 663, 238-249.

Wallace, L. M., S. Ellis, and P. Mann (2009), Collisional model for rapid fore-arc block rotations, arc curvature, and episodic back-arc rifting in subduction settings, Geochemistry, Geophysics, Geosystems, 10(5).

Wallace, L. M., C. Stevens, E. Silver, R. McCaffrey, W. Loratung, S. Hasiata, R. Stanaway, R. Curley, R. Rosa, and J. Taugaloidi (2004), GPS and seismological constraints on active tectonics and arc-continent collision in Papua New Guinea: Implications for mechanics of microplate rotations in a plate boundary zone, Journal of Geophysical Research: Solid Earth, 109(5), B05404 05401-05416.

Weijermars, R. (1986), Flow behaviour and physical chemistry of bouncing putties and related polymers in view of tectonic laboratory applications, Tectonophysics, 124(3-4), 325-358.

Weijermars, R., and H. Schmeling (1986), Scaling of Newtonian and non-Newtonian fluid dynamics without inertia for quantitative modelling of rock flow due to gravity (including the concept of rheological similarity), Physics of the Earth and Planetary Interiors, 43(4), 316-330.

Wortel, R. (1982), Seismicity and rheology of subducted slabs, Nature, 296(5857), 553-556.

Wright, I. C. (1993), Pre-spread rifting and heterogeneous volcanism in the southern Havre Trough back-arc basin, Marine Geology, 113(3-4), 179-200.

Yamato, P., L. Husson, J. Braun, C. Loiselet, and C. Thieulot (2009), Influence of surrounding plates on 3D subduction dynamics, Geophysical Research Letters, 36(7).

Zhu, H., and J. Tromp (2013), Mapping tectonic deformation in the crust and upper mantle beneath Europe and the North Atlantic Ocean, Science, 341(6148), 871-875.

Zlotnik, S., P. Díez, M. Fernández, and J. Vergés (2007), Numerical modelling of tectonic plates subduction using X-FEM, Computer Methods in Applied Mechanics and Engineering, 196(41-44), 4283-4293.